Studies of Dielectric Multipactor Discharges and Gas Breakdown Initiated by High Power Millimeter Waves

by

Samuel Clay Schaub

B.S. Physics, Valparaiso University (2011)
B.S. Chemistry, Valparaiso University (2011)

Submitted to the Department of Physics
in partial fulfillment of the requirements for the degree of

Doctor of Philosophy

at the

MASSACHUSETTS INSTITUTE OF TECHNOLOGY

June 2019

Author ..... Signature redacted
Department of Physics
March 28, 2019

Certified by ..... Signature redacted
Richard J. Temkin
Senior Research Scientist, Department of Physics
Thesis Supervisor

Accepted by ..... Signature redacted
Nergis Mavalvala
Associate Department Head

Studies of Dielectric Multipactor Discharges and Gas Breakdown Initiated by High Power Millimeter Waves

by

Samuel Clay Schaub

Submitted to the Department of Physics
on March 28, 2019, in partial fulfillment of the
requirements for the degree of
Doctor of Philosophy

Abstract

This thesis reports the theoretical and experimental investigation of discharge phenomena induced at dielectric surfaces and in gases by a 1.5 MW, 110 GHz gyrotron operating in 3 μs pulses.

The experimental study of multipactor discharges on dielectric surfaces in vacuum was performed at 110 GHz, a frequency that is an order of magnitude higher than in previous experimental studies. Two separate test assemblies were constructed: one with the 110 GHz electric field tangential to the dielectric surface and the second with a perpendicular field. Threshold electric fields for multipactor onset were measured in both field orientations for samples of sapphire, alumina, fused quartz, crystal quartz and silicon. The present results at 110 GHz, when combined with previously published data at lower frequencies, show that the threshold electric field for initiation of a dielectric multipactor discharge scales linearly with frequency. This linear scaling, which is favorable for operation at high frequency, is in good agreement with theoretical predictions. The absorbed RF power due to multipactor was also measured as a function of RF intensity. At low intensities, absorbed RF power was found to agree quantitatively with theoretical predictions, though experimental results diverged from theory at higher RF intensities.

Calculations of dielectric multipactor were carried out to help analyze the experimental results. A new equation for predicting threshold RF electric fields was derived that agrees with a wide variety of existing experimental data, spanning orders of magnitude in frequency and a variety of geometries and materials. The theory work also suggests strategies for mitigation of multipactor, dependent upon experimental geometry.

Gas breakdowns were experimentally characterized at both 110 and 124.5 GHz by focusing the gyrotron beam in air at pressures from 25 to 760 Torr. Prior studies of this system had revealed that the plasma spontaneously forms a reproducible two-dimensional array of filaments. Optical emission spectroscopy was used to measure peak electron density in this plasma, through Stark broadening of the H_α line. Heating dynamics of the background neutral gas were spatially and temporally resolved

using two-dimensional laser interferometry. These results help test the theory of gas breakdown at 110 GHz.

Thesis Supervisor: Richard J. Temkin
Title: Senior Research Scientist, Department of Physics

Acknowledgments

The accomplishments of this thesis were only possible because of the great support, aid, and contributions I received from many others.

I must begin by thanking my research advisor and thesis supervisor, Dr. Richard Temkin. He guided my research at MIT, and had invaluable advice or motivation for nearly every difficulty encountered. He has taught me what it is to be an excellent scientist. His example, his vast knowledge, and his diverse expertise will be an aspirational role model for the rest of my career. I am grateful as well to Dr. Michael Shapiro for entertaining my many questions and requests. Much of my work at MIT was aided by his mathematical skills, knowledge, and bountiful patience. I will greatly miss working with him.

Every member of Dr. Temkin's group at MIT had a positive influence on my education or my work here. Ivan Mastovsky rescued me from numerous equipment failures and technical disasters with great speed and proficiency. David Tax dedicated significant time to teaching me the use of our megawatt gyrotron lab, and Jason Hummelt was a steady source of support as I assembled my first plasma physics experiment. Dr. Sudheer Jawla's extensive proficiency and assistance with a variety of microwave diagnostics eased innumerable tasks and measurements. A short conversation with Dr. Guy Rosenzweig on the day we met, even before he joined our group, is the reason the two-dimensional interferometer presented in this thesis ever worked. Jacob Stephens brought a new expertise of low temperature plasmas to our group, and has shared his knowledge and advice freely. Xueying Lu aided me in experimental data collection tasks as a new graduate student, and went on to perform creative, successful work of her own that has been fascinating to follow.

JieXi Zhang, my officemate of four years, provided me with advice on electromagnetic simulations, and a delightful, peaceful workspace. Alexander Soane spent years as the designated social butterfly of our group, helping all of us to get to know one another better. My fellow graduate student, Haoran Xu, has an open door policy for impromptu chats of multipactor and accelerators. Our conversions and his

regular presentations were of great value to my own research efforts. At the end of my research, Julian Picard took over my duties in the gyrotron lab with astounding eagerness. His zeal for experimental work allowed me to focus on my thesis writing and finish my time here.

I wish also to thank my undergraduate research mentors, Dr. Todd Hillwig and Dr. Bruce Hrivnak. The opportunity to research and publish as an undergraduate was an invaluable part of my graduate school applications. I fondly remember my many nights working in an astronomical observatory, and look eagerly forward to having the time to take up astronomy once again, though this time as an amateur.

Outside of MIT, I must thank my parents, whose continuous support has made everything I have in life possible. My best friend, and my best man, Hong Sio, is perhaps my best discovery from MIT. He, along with our friends Anton and Colin have made my time in Boston far richer. I am thankful for the many hiking trips, shared meals, and conversations that enriched my time away from the lab. My wife, Rebecca, has shown great patience as I wrap up my work at MIT. She added an entirely new dimension to my life, and I look forward to the life we will build together from here.

Contents

List of Figures

List of Tables

Chapter 1

Introduction

1.1 Millimeter Waves

The millimeter wave band of the electromagnetic spectrum runs from 30 to 300 GHz, lying at the high frequency end of the microwave regime, just below the far infrared, or terahertz regime (see Fig. 1-1). Also known as the extremely high frequency band (EHF), low power millimeter waves have found extensive use in radio astronomy, telecommunications, and imaging applications (for security screening and quality control). Commercial applications, primarily existing at frequencies below 100 GHz, have only arisen in the last couple of decades as microwave sources at these frequencies have developed and matured.

Existing in a regime between traditional radio frequencies and infrared light, millimeter waves bring unique technical challenges. Millimeter waves experience high attenuation in the coaxial cables and metallic waveguides often used to contain and transport radio frequency and traditional microwave signals. Though single-moded metallic waveguides are used to transport millimeter waves over short distances, up to a few hundred wavelengths, both metal and dielectric materials show losses that increase with frequency and become less useful in the millimeter wave regime. Millimeter and terahertz waves are often propagated in quasioptical systems [23, 24]. Away from frequencies of strong atmospheric absorption, quasioptical systems make use of the low loss nature of propagating electromagnetic waves in free space. In

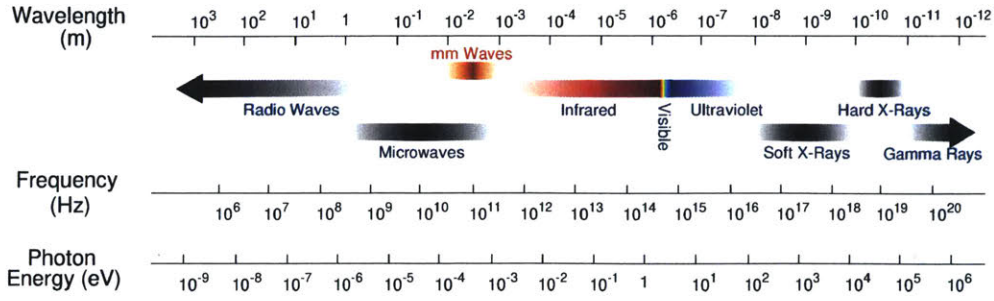

Figure 1-1: The electromagnetic spectrum. The region designated as millimeter waves (30 - 300 GHz) is labeled in orange.

contrast to geometric optics techniques that are useful at higher frequencies, electromagnetic beams of millimeter waves, and the optics that manipulate them, are not much greater in size than the wavelength of the radiation. Apertures and optics that satisfy the approximation of geometric optics that the lateral dimensions, D, must be much much greater than the wavelength, $D \gg \lambda$, would be impractically large. The field of quasioptics makes use of traditional optical techniques, but designs of quasioptical components must use a less approximate theory of electromagnetic radiation to account for the strong influence of diffraction that is ignored in geometric optics. In contrast to longer wavelength radio frequency (RF) waves, the wavelength of millimeter waves is just short enough that they do tend to propagate optically, and applications require a line-of-sight between sources and receivers. Millimeter waves are neither reflected by the ionosphere, nor do they travel along the ground as RF waves do. Additionally, even in the atmospheric windows that avoid molecular absorption peaks, millimeter waves are more strongly absorbed in the atmosphere than lower frequency electromagnetic waves, and applications are limited to ranges of a few kilometers or less.

1.2 Organization of this Thesis

The needs of the nuclear fusion research community for high power sources at frequencies from 100 to 200 GHz have led to the development of high power (0.5 - 2 MW) gyrotrons, a form of vacuum tube microwave source, over the last few decades. Orig-

inally developed for the heating of electrons in magnetically confined fusion devices, high power gyrotrons have opened up a new parameter space for potential study and applications. A pulsed gyrotron, capable of delivering 3 microsecond pulses of up to 1.5 MW of power at 110 or 124.5 GHz has been developed at MIT. This gyrotron was at the core of all of the experiments presented in this thesis. Chapter 2 provides a general overview of gyrotrons, and specific details of the MIT high power gyrotron. Section 2.6 details an internal mode converter that was installed and tested in the course of this thesis.

This thesis presents studies of two distinct forms of electrical discharges initiated and sustained by high power millimeter waves. Presented first is a study of multipactor on dielectric surfaces in vacuum. Multipactor is a process by which an oscillating electric field creates an electron avalanche on a surface in vacuum, leading to the formation of a cloud of electrons. Generally a phenomenon to be avoided or mitigated in modern applications, multipactor has not been studied at frequencies above 30 GHz, due to a historical lack of microwave sources at millimeter wavelengths. The development of high power sources, including gyrotrons, at millimeter wave frequencies is opening up new applications. It is desirable to understand if scaling laws and theories that have been developed to explain RF and low frequency microwave multipactor continue to usefully apply in this higher frequency regime. The phenomenon of multipactor is introduced in chapter 3. The theory of multipactor on dielectric surfaces is derived in chapter 4. Section 4.1 details existing, published theory. Sections 4.2.1 - 4.5 describe new work that was performed as part of this thesis. The design and results of an experiment to test theoretical predictions and historic scaling laws for dielectric multipactor are presented in chapters 5 - 6.

The second form of discharge presented in this thesis is millimeter wave discharges in a gas (air). Focused to a spot size of a few wavelengths, the millimeter wave output of the MIT MW gyrotron is capable of producing a plasma in air at pressures up to 1 atmosphere (760 Torr). Unexpectedly, such a plasma was found to spontaneously form into a regular, two-dimensional array of plasma filaments. This spontaneously complex plasma forming from a simple experimental arrangement proved to be an

excellent test case for theoretical models of microwave-plasma interactions in weakly ionized plasmas. Chapter 7 provides a full description of this plasma, an overview of prior work done at MIT, as well as theoretical work that has been carried out by research groups outside of MIT. This is followed by chapter 8 that describes experiments carried out for this thesis. Two new plasma diagnostics were implemented: spectroscopy and two-dimensional laser interferometry. The two-dimensional laser interferometry, in particular, provided measurements of plasma parameters as a function of both time and space. The plasma parameters measured by these diagnostics are compared to the predictions of prior theoretical work.

The final chapter of this thesis, chapter 9, summarizes the conclusions and accomplishments of this thesis work. Additionally, a description of ongoing and future work, to be carried on by the same research group, is provided.

Chapter 2

110 GHz, 1.5 MW Gyrotron Microwave Source

2.1 Gyrotrons

The research of this thesis was possible because of the development, over the past few decades, of high power gyrotrons at millimeter wave frequencies. The development of these high power sources was largely driven by the needs of the nuclear fusion research community. In several fusion experiments and designs for potential future fusion reactors, multiple MW's of power are required at frequencies of 100-200 GHz to heat electrons and drive currents through electron cyclotron heating (ECH) and electron cyclotron current drive (ECCD) systems. The development of these new sources has opened up a new parameter space for research with high power microwaves. Because high power gyrotrons were so central to this thesis, sections 2.1 - 2.4 provides an overview of gyrotrons in general, to provide the reader with a basic understanding of these devices. Section 2.5 provides specific details on the 1.5 MW MIT gyrotron as it was configured for the study of millimeter wave discharges in gas. During the progress of this thesis work, a new output section was installed and tested on the MIT gyrotron that coupled the output directly into a waveguide. This proved to be of great benefit for the studies of multipactor discharge, facilitating precise alignment between the test structures and the high power microwave output. Though it was

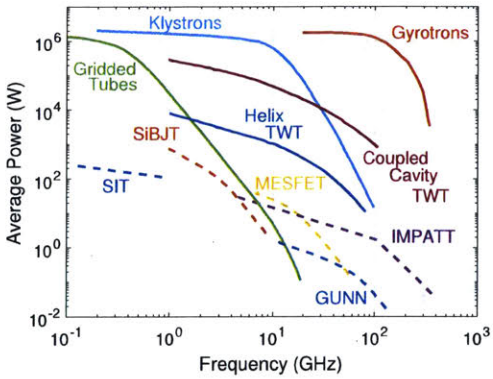

(a) Comparison of average power versus frequency for vacuum electron devices (solid line), and solid-state devices (dashed). Modified from [25].

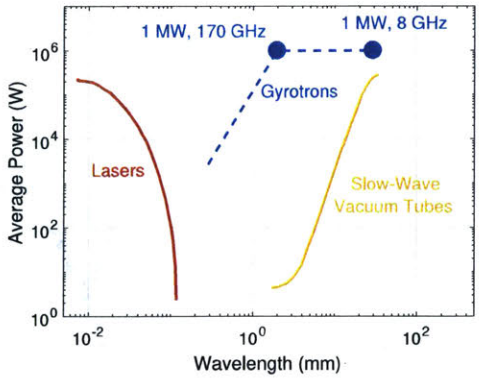

(b) High power sources in different wavelength regimes. Modified from [26].

Figure 2-1: Plots comparing the power and spectral output of gyrotrons compared to other sources. Gyrotrons provide high power in a frequency range not well served by conventional sources.

not a central point of study of this thesis, the testing of this gyrotron output section is presented in section 2.6.

Gyrotrons are vacuum tube microwave sources based on the electron cyclotron maser interaction. Fig. 2-1 shows where gyrotrons fit among other electromagnetic wave sources. There exists a gap in technology in the regions between infrared light (served by lasers) and conventional microwave and RF frequencies (served by a variety of vacuum tube and solid-state sources). High power gyrotrons have encroached on this gap from the low frequency side, and have opened a new regime of high frequency microwaves (millimeter waves) to experimental studies and applications.

To understand how a gyrotron operates, first consult the schematic of a gyrotron shown in Fig. 2-2. Conceptually, the gyrotron can be broken up into three processes: electron beam formation/propagation, wave-beam interaction, and microwave extraction/beam collection. In sections 2.2 - 2.4, these processes will be elaborated upon, along with the governing laws and equations that describe them.

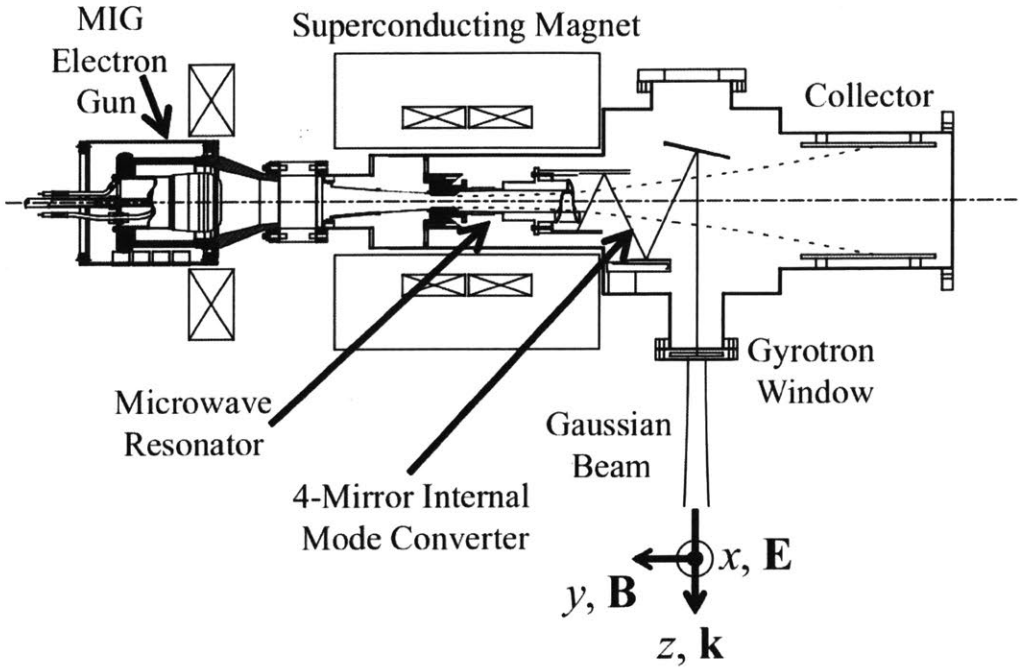

Figure 2-2: Schematic of a gyrotron oscillator. In the electron gun, the electron beam is drawn towards a grounded anode from the surface of a heated thermionic cathode held at a high negative potential. The electron beam is compressed by a powerful magnetic field, provided by the superconducting magnet, and interacts with the electromagnetic mode of a cavity located at the center of the solenoidal magnet. The cavity is label "Microwave Resonator". The wave power is extracted through a quartz window by means of a mode converter and a set of copper mirrors. The electron beam terminates on a grounded copper collector. Modified from [1].

2.2 Electron Beam Formation and Propagation

The principal component of electron beam formation is an electron gun, specifically a magnetron injection gun (MIG) in gyrotrons. A diode configuration, as shown in Fig. 2-2, is used in the MIT MW gyrotron, meaning that the gun is comprised simply of a cathode and a single anode. Many different types of cathodes exist, like the M-type cathode consisting of a porous tungsten pellet impregnated by a mixture of BaO, CaO, and Al_2O_3 and coated with osmium. While the materials science behind cathodes is quite complex, the overall goal is a surface with a low work function, which is the minimum amount of energy needed to break the atomic bonds and draw an electron to the surface of the metal.

In a MIG, the annular cathode ring is placed on a solid stock with a heating filament. Electrons are drawn to the surface of the cathode by means of thermionic emission as the cathode is heated to temperatures of ~1000 °C. The electrons are accelerated towards the anode when a large negative voltage is applied at the cathode while the anode is maintained at ground potential. Two regions of operation exist for such a gun: a space-charge-limited regime and a temperature-limited regime. In the space-charge limited regime, the electron population at the cathode surface saturates and prevents further electrons from being drawn to the surface without increasing the applied voltage, accelerating more electrons away from the cathode surface. In the temperature-limited regime, the population of electrons at the surface is wholly accelerated towards the anode, and the emitted current can only be increased by raising the cathode temperature and thus the amount of electrons being drawn to the surface. There is also an additional element in the temperature-limited regime from the Schottky effect, in which the electric field at the cathode surface causes an effective lowering of the metal's work function and enhances emission. The emitted current density for the space-charge-limited regime is given by the Child-Langmuir law:

$$J_{SCL} = \frac{4\varepsilon_0\sqrt{2e/m_e}}{9d^2}V^{3/2} \tag{2.1}$$

where e is the charge of an electron, m_e is its mass, ε_0 is the permittivity of free space,

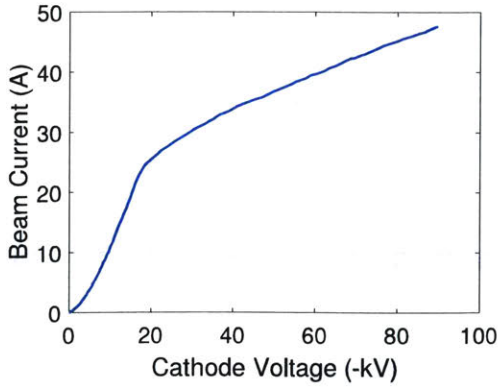

Figure 2-3: Sample I-V (current-voltage) curve for the electron gun used in the MIT 1.5 MW, 110 GHz gyrotron experiment. At higher voltages the gun operates in the temperature-limited regime. Below 15-20 kV, it operates in the space-charge-limited regime. Modified from [2].

d is the spacing between the cathode and anode, and $-V$ is the cathode voltage. The combination of the terms that relate the scaling of current to the voltage to the 3/2 power is known as the gun's perveance, K. The Child-Langmuir law applies only up to some threshold voltage at which point the current emission will be described by the Richardson-Dushman equation for the temperature-limited regime:

$$J_{TL} = \lambda_R A_0 T^2 \exp\left[\frac{-e}{kT}\left(\varphi - \sqrt{\frac{eE}{4\pi\varepsilon_0}}\right)\right] \tag{2.2}$$

where $A_0 = 120$ A/cm^{2}K^2 is a constant, λ_R is a material-specific correction factor [27], T is the cathode temperature, k is the Boltzmann constant, φ is the cathode work function, and E is the electric field at the cathode surface [28]. A sample I-V curve is shown in Fig. 2-3, where the transition between the two operational regions of the electron gun is easily observed around 15-20 kV. The exact transition point is ill-defined due to a finite spread in the value of the work function throughout the cathode [29].

Electron guns for megawatt class gyrotrons require high beam power and operate at high voltages (50-100 kV). They must therefore operate in the temperature-limited regime. This is convenient for gyrotron operation due to the fact that the beam current depends only weakly on any perturbation to the voltage, and stable beam

current is essential for high efficiency operation.

2.3 Electron Cyclotron Maser Interaction

The generation of electromagnetic wave energy from electron kinetic energy occurs in the cavity of the gyrotron, labeled "Microwave Resonator" in Fig. 2-2. The cavity is a cylindrical section of waveguide, approximately centered in the center of the DC magnetic field provided by a superconducting solenoid magnet. Toward the electron gun, the waveguide tapers to a smaller diameter, below the cutoff frequency of the operational electromagnetic mode of the gyrotron cavity, closing off one end of the cavity to microwave propagation. Toward the output and the "Collector", the end of the cavity tapers to slightly larger radius. This creates a small mismatch in the waveguide impedance for the microwaves, reflecting some of the power back into the microwave cavity. This taper acts as a semi-transparent microwave mirror. Within the cavity, the parameters of the electron beam and cavity electromagnetic mode are designed to spontaneously transfer energy to the cavity mode via the electron cyclotron maser (ECM) interaction.

2.3.1 Phase Bunching

The ECM interaction is the basis for a variety of vacuum tube RF sources, of which gyrotrons are an important example. The basics of the ECM interaction can be understood by considering figures 2-4 and 2-5. Fig. 2-4 shows an electron moving under the influence of a uniform longitudinal magnetic field in the presence of a uniform transverse RF electric field of angular frequency ω. The electron gyrates in a circular orbit with an angular velocity equal to the relativistic cyclotron frequency,

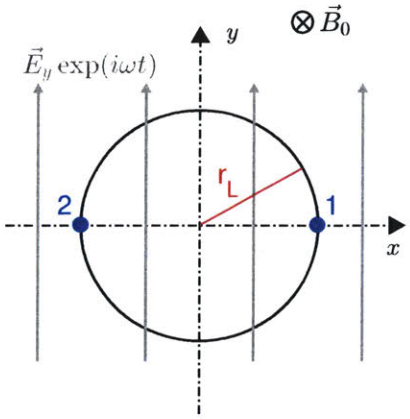

Figure 2-4: Geometry of a basic electron cyclotron interaction. The electron is gyrating about a DC magnetic field that is into the page. The electron is accelerated or decelerating by the oscillating electric field, $\vec{E}_y$, depending upon its position and the phase of the RF field. Modified from [3].

Eq. 2.3.

$$\omega_c = \frac{eB_z}{m_e\gamma} \tag{2.3}$$

$$\gamma = \left(1 - \frac{u^2}{c^2}\right)^{-1/2} \tag{2.4}$$

$$u^2 = u_\theta^2 + u_z^2 \tag{2.5}$$

In these equations, e and m_e are the charge and mass of an electron, B_z is the magnetic field (down the axis of the gyrotron), u is the electron velocity and c is the speed of light. The tangential and axial components of the electron velocity are u_θ and u_z, and it is assumed that the radial component of the electron velocity is negligible. It can be seen that, because of the relativistic factor, γ, the cyclotron frequency decreases as the electron velocity increases.

If the axial motion of the electrons, u_z, were to be ignored, the motion of an electron is in synchronism with the RF field when $\omega = \omega_c$. A synchronous electron at position 1 in Fig. 2-4 experiences a retarding field. When it reaches position 2, the direction of the RF electric field has reversed, and the motion of the electron is further retarded. Similarly, an electron starting at position 2 is accelerated and then accelerated again when it reaches position 1. The accelerated electrons fall back

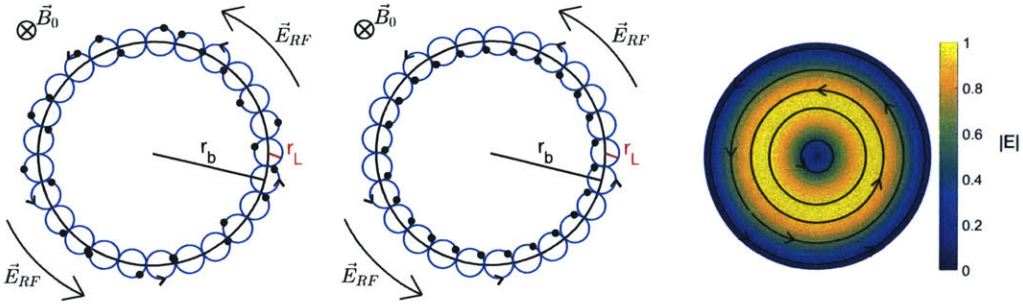

(a) Initial random phasing (b) Bunched in phase (c) TE_{01} mode of circular waveguide

Figure 2-5: Illustration of gyro-phase bunching in an annular electron beam in the RF field of a TE_{01} mode in circular waveguide. A DC magnetic field is into the page. Modified from [4].

in phase relative to the RF field, because of the change in cyclotron frequency with velocity. Similarly, retarded electrons move forward in phase so that electron bunches (in RF and gyro phase) are formed. If these bunches fall in the retarding phase of the RF field, then there is a net transfer of energy from the electrons to the wave, as required of an RF source. Note that, when relativistic effects are ignored, the cyclotron frequency is constant and no bunching occurs. A necessary condition for the ECM interaction is that the electron velocity should be high enough for relativistic effects to be important.

Fig. 2-5 illustrates phase bunching of electrons in an annular electron beam in the RF electric field of a TE_{01} mode of a circular waveguide. This is a mode with a purely azimuthal electric field. The radius of the orbit of each electron is the Larmor radius, $r_L = u_\theta/\omega_c$, which increases as the electron velocity increases. In the MIT megawatt gyrotron, the Larmor orbit is less than 1/10th of an RF wavelength, so the RF electric field is approximately uniform across an individual orbit.

2.3.2 Synchronicity Condition

The electron beam of a gyrotron is normally generated by a magnetron injection gun (MIG). This generates an annular (hollow tube-like) electron beam. The energy of

the electrons can be written as Eq. 2.6 [3].

$$u_\theta^2 + u_z^2 = c^2 \left(1 - \frac{1}{[1 + (eV_a/m_e c^2)]^2}\right) \tag{2.6}$$

The anode to cathode potential of the electron gun is denoted as V_a. The ratio of the transverse (to the magnetic field) velocity to the axial velocity is denoted by the pitch factor $\alpha = u_\theta/u_z$. This parameter is typically greater than unity. Because only the transverse energy can be converted into RF power. The efficiency of energy extraction from the electron beam cannot exceed

$$\eta_e = \frac{(u_\theta^2 + u_z^2) - u_z^2}{u_\theta^2 + u_z^2} = \frac{\alpha^2}{1 + \alpha}. \tag{2.7}$$

In practical reality, it is not possible to reduce tangential electron energies to zero and realized efficiencies are smaller than that given by Eq. 2.7.

When the axial velocity of the electrons is taken into account, the synchronous condition is altered from the simplistic $\omega = \omega_c$. The time taken for an electron to make one gyro orbit is

$$t_{gyro} = \frac{2\pi}{\omega_c}. \tag{2.8}$$

In that time, the electron moves through an axial distance

$$z_{gyro} = u_z t = \frac{2\pi u_z}{\omega_c}. \tag{2.9}$$

For synchronism, the phase of the electromagnetic wave as seen by the electron must be

$$\omega t - k_z z = 2s\pi, \tag{2.10}$$

where the wave propagates as $exp(i(\omega t - k_z z))$ with k_z propagation constant, and s is a positive integer. Substituting t and z for t_{gyro} and z_{gyro}, the synchronism condition is found to be

$$\omega = k_z u_z \pm s\omega_c, \tag{2.11}$$

where the first term on the right hand side represents the Doppler shifting of the

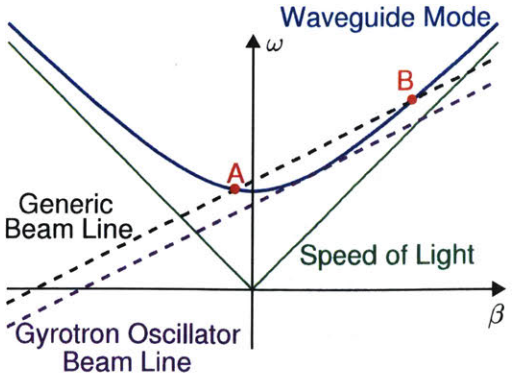

Figure 2-6: Example dispersion diagram for a gyrotron. The "Generic Beam Line", Eq. 2.14, represents cyclotron waves on an electron beam. The "Waveguide Mode", Eq. 2.13, represents the dispersion of a mode in a uniform section of waveguide. Gyrotron oscillators are tailored to have a tangent interaction between the beam line and the waveguide mode.

frequency caused by the motion of the electrons along the magnetic field.

The dispersion curve of any mode in a uniform waveguide can be written as

$$k_z = \frac{1}{c}\sqrt{\omega^2 - \omega_{mn}^2}, \tag{2.12}$$

where ω_{mn} is the cut-off angular frequency of the mode with the mode numbers (m, n). A uniform waveguide, here, is defined as a section of waveguide with a constant cross section as a function of axial position. This dispersion curve for waves in a waveguide can be written in normalized form as

$$\frac{\omega}{\omega_{mn}} = \sqrt{1 + \frac{k_z^2}{k_{mn}^2}}, \tag{2.13}$$

where $k_{mn} = \omega_{mn}/c$. This is an uncoupled dispersion diagram, ignoring the effects of coupling between waveguide modes and the electron beam. Using the same normalizations, the dispersion equation for waves on the electron beam, Eq. 2.11, can be written as

$$\frac{\omega}{\omega_{mn}} = \frac{k_z u_z}{k_{mn} c} \pm \frac{s\omega_c}{\omega_{mn}}. \tag{2.14}$$

Fig. 2-6 shows a typical uncoupled dispersion diagram plotted using equations 2.13 and 2.14. It can be seen that there are typically two points of intersection between a particular waveguide mode (solid blue line), and the electron cyclotron wave (black dashed line). The two points of intersection are labeled A and B. The locations of these points can be tailored in a device by altering the electron beam voltage and pitch factor, and adjusting the DC magnetic field. Different types of ECM devices correspond to choices of points A and B. A gyrotron oscillator, in particular, operates in a condition where points A and B coincide (the beam line is adjusted to be tangent to the waveguide mode line), at small positive values of k_z (the purple dashed line in Fig. 2-6). The most efficient operating point is when this tangent intersection is very close to $k_z \approx 0$, just above the cutoff frequency of the waveguide mode. A grazing, tangent synchronicity condition is chosen to minimize the effect of velocity spread in the electron beam (a finite width distribution of electron velocity) [26].

2.3.3 Transference of Electron Energy to RF Energy

At the same time as phase bunching is spontaneously occurring, a slight detuning between the RF frequency of the waveguide mode and the cyclotron frequency of the electrons causes a slowly increasing phase shift, which brings the bunched electrons into a phase where energy extraction to the RF wave occurs. If there were no frequency detuning (Eq. 2.13 = Eq. 2.14), the same number of electrons would be accelerated and decelerated, and no net energy would be exchanged between the electrons and the field. However, energy is transferred if the wave frequency is somewhat larger than the initial value of the cyclotron frequency:

$$\omega - \omega_{c0} > 0 \tag{2.15}$$

where $\omega_{c0} = eB/m_e\gamma_0$ is the cyclotron frequency with the initial electron launch energy. In this case, more electrons are decelerated over an RF period than are accelerated by the RF electric field and net energy is transferred to the RF wave. The wave amplitude increases and wave energy grows exponentially in time for each

RF period.

2.4 Microwave Power Extraction and Electron Beam Collection

The output taper of the cavity is, essential, a weakly tapered cylindrical waveguide that allows the TE mode of the interaction cavity to propagate further down the axis. In the same region, the electron beam, after losing a significant portion of its energy, continues to travel towards a collector located at the far end of the vacuum tube.

The simplest method of power extraction is to continue propagating the electromagnetic waves axially to a window located at the end of the tube. Early gyrotrons used this approach, and it is still employed occasionally as an experimental configuration. It is not particularly practical, however, in a real gyrotron system where the output power is to be used. The spatial intensity pattern of such an output is quite complex.

Instead, gyrotrons implement internal mode converters which aim to convert the TE mode of the cavity into a more practical output for transmission, like a Gaussian beam. An internal mode converter can be seen in Figure 2-1 and consists of a quasi-optical "launcher", i.e. a section of waveguide following the cavity, and a set of copper mirrors. The launcher can be best understood by considering the propagating waveguide mode as a set of rays bouncing around the inside of the waveguide at an angle. By implementing a step-cut at the end of this waveguide, these rays are "launched" out of the waveguide and may be collected on the surface of a copper mirror which directs the power towards a window [30]. In the case of a mode that rotates with the electron beam, such a cut should be helical. By adding perturbations to the surface of the launcher, these rays may become grouped and a Gaussian intensity profile is generated on the surface of the waveguide [31]. Proper design of this launcher allows for this Gaussian profile to be launched from a cut onto the surface of the first mirror. As codes to design these launchers have become more sophisticated, the efficiency of

these converters has increased. Output beams with as high as 98 or 99 % Gaussian beam content are now achievable.

Dealing with the spent electron beam is simultaneously a remarkably simple process and a challenging one. In the case of a pulsed gyrotron, even for high beam power, like the ~4 MW of a 96 kV and 40 A beam, at microsecond pulse lengths, this only yields a maximum of a few joules of energy deposited on the collector. Therefore, in such an experiment, the collector may simply be a grounded copper cylinder without any cooling required. In a CW (continuous wave) tube, the energy deposition is significant. Not only do these tubes require massive water cooling systems, but they also often implement a sweeping coil, which is a small variable magnetic field that ensures the beam does not constantly impact the same location on the collector.

An additional element that can be introduced is a "depressed collector." The depressed collector allows for improvement of the gyrotron's overall efficiency by holding the collector at an intermediate potential while maintaining the same potential difference between the cathode and the anode, which is part of the tube's "body". This can be accomplished by either adding a resistive load between the collector and body or using two separate power supplies. Implementation of a depressed collector was part of previous doctoral work on the MIT MW gyrotron [4].

The final component to consider is the window. First and foremost, it must be strong enough to maintain high vacuum in the tube. An additional concern in CW gyrotrons is the heat loading. Diamond windows (with very high thermal conductivity) are a necessity in a CW megawatt gyrotron, while a simple fused quartz window will suffice for pulsed operation or for lower power gyrotrons. For a single frequency gyrotron, a single disc window whose thickness is designed for full transmission at that frequency is employed. In instances where frequency transmission over a wider frequency band is desired, alternatives like a double disc window or a Brewster angle window must be considered.

2.5 The MIT Gyrotron

The MIT MW gyrotron has been developed over the course of several PhD's [2,4,26]. The original design produced 1.43 MW of power at a single frequency, 110 GHz, in 3 microsecond long pulses [32]. The frequency of this gyrotron matches the electron cyclotron heating system of the DIII-D fusion experiment at General Atomics in San Diego, so that knowledge gained from its development could directly benefit the fusion research community.

When configured for a single mode of operation, the MIT MW gyrotron produced a maximum of 1.67 MW of microwave power from a 97 kV, 41 A electron beam, operating at an impressive 42% efficiency [33]. At 110 GHz, the gyrotron was designed to work with the very high order $TE_{22,6}$ cavity mode. The electric field of this mode is shown in Fig. 2-7a. In the gyrotron community, TE_{mn} modes with $m \gg n$ are referred to as whispering gallery modes. For generation of very high average powers, these high order modes allow the use of cavities very large compared to the generated microwave wavelength. This allows a large, high current, high power electron beam to pass through the cavity. Additionally, these modes have weak electromagnetic fields along the cavity wall, losing little energy to ohmic losses in the copper surface of the cavity. The advantages offered by these modes are essentially for constructing sources that can continuously generate megawatts of microwaves, maximizing available electron beam power and minimizing thermal loads on the microwave tube components.

2.5.1 Two-Frequency Gyrotron

The MIT MW gyrotron was modified by PhD student David Tax to produce output at two frequencies [2, 34]. The cavity and mode launcher section were optimized for functionality at either 110 or 124.5 GHz. In addition to the $TE_{22,6}$ mode at 110 GHz, the gyrotron cavity was redesigned to allow interaction with the $TE_{24,7}$ mode at 124.5 GHz (See Fig. 2-7b). In the experiment, the gyrotron could produce either 1.25 MW power at 110 GHz or 1 MW power at 124.5 GHz. As in previous designs, the gyrotron was operated in 3 microsecond long pulses. This modification of the gyrotron

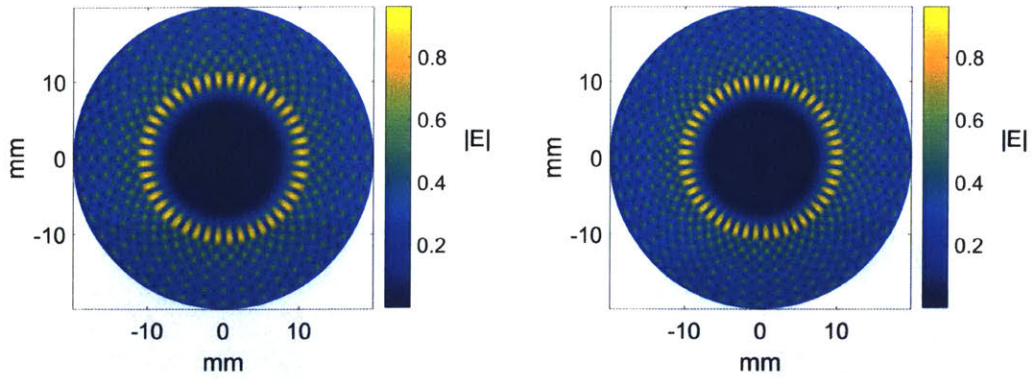

(a) $TE_{22,6}$ Mode at 110 GHz (b) $TE_{24,7}$ Mode at 124.5 GHz

Figure 2-7: Electric field (normalized magnitude) of the high order TE cavity modes of the MIT megawatt gyrotron configured to operate at either 110 or 124.5 GHz. These modes are calculated in a 1.98 cm radius section of circular waveguide.

continued to use a four-mirror mode converter, as displayed in Fig. 2-2. The ouptut of the gyrotron was a Gaussian beam of microwaves in free space. Operation at the two frequencies was performed at different values of the main magnetic field. Only one operational mode was excited at a time.

It was in this configuration that the MIT MW gyrotron was used for studies of millimeter wave discharges in gas, with data collected at both available frequencies. A notable feature of this configuration was the very high quality output microwave beams from the gyrotron. The pattern of the output is shown in Fig. 2-8. The output patterns are located at the window of the gyrotron. The intensity is very well represented by a Gaussian profile. Note that the intensity plots, subfigures (a) and (c), are shown in units of decibels, a logarithmic scale. The phase of the microwave output is mapped in subfigures (b) and (d). In the central region of the microwave beams, the phase is very nearly constant, indicating a flat phase front. This demonstrates that the waist (focal point) of the Gaussian microwave beam is accurately placed at the gyrotron window. The output of the gyrotron was measured to be 99% Gaussian at 110 GHz, and 97% at 124.5 GHz. This high quality output allowed for precise knowledge of the shape and intensity of the microwave beam used in the millimeter wave gas discharge experiments.

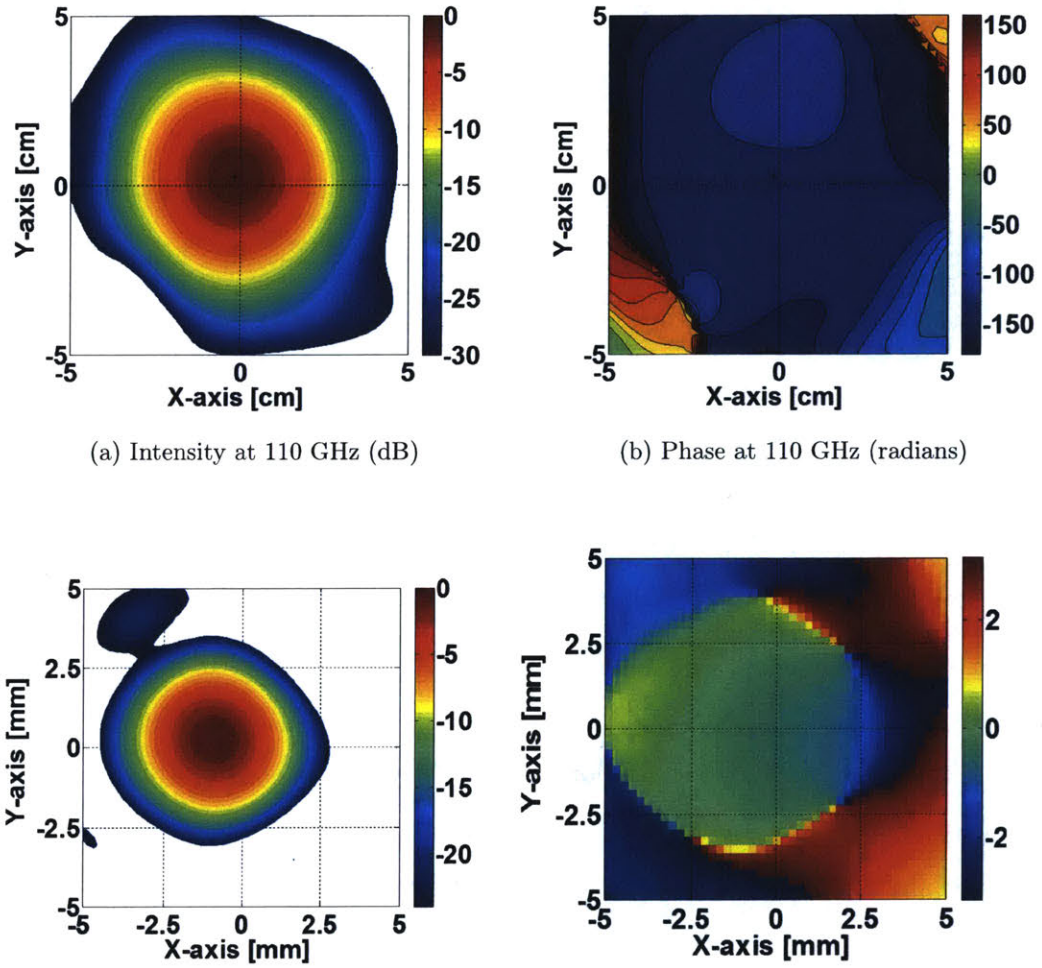

(a) Intensity at 110 GHz (dB)

(b) Phase at 110 GHz (radians)

(c) Intensity at 124.5 GHz (dB)

(d) Phase at 124.5 GHz (radians)

Figure 2-8: Measured output beam from the two-frequency configuration of the MIT 1.5 MW gyrotron. This was calculated from data taken at 3 distances from the gyrotron window. The phase retrieval method of [5] was used to calculate the intensity and phase at the window.

2.6 Testing and Installation of a $TE_{22,6}$ to HE_{11} Internal Mode Coupler

During the course of the presented thesis work, a new output section was installed and tested in the MIT gyrotron. This output section was designed to directly couple the output of the $TE_{22,6}$ mode of the gyrotron cavity at 110 GHz to the HE_{11} mode of an oversized corrugated waveguide. The HE_{11} mode is the lowest order mode of a corrugated waveguide [35], and it matches 98% to a free-space Gaussian beam [36]. The waveguide is about 11 wavelengths in diameter, making the mode far from cut-off. Thus, there is little impedance mismatch at the end of the waveguide, and it can be used to directly launch a Gaussian beam into free space with little reflection. Essentially, a corrugated waveguide is a low-loss method of transporting a microwave Gaussian beam without allowing it to diffract. Such waveguide is extensively used to transport millimeter wave power from gyrotrons to plasma devices in electron cyclotron heating schemes on nuclear fusion experiments.

2.6.1 CCR Internal Mode Coupler

The new output section was designed externally by the company Calabazas Creek Research (CCR), with the intention to test it on the MIT MW gyrotron. Like the original output sections of the gyrotron, the mode of the cavity is launched from a helical cut on a circular waveguide. In a typically quasioptical launcher, the launched Gaussian-like beam is highly elliptical and rapidly diverging. The profiles of the mirrors in the four-mirror launchers are contoured to modify the microwave output into a nearly circular beam. In contrast, to create a more compact system, the last surface from which microwaves are reflected from the helically cut waveguide in the CCR launcher was warped to produce a nearly circular beam directly. This parallelogram shaped region of the launcher was numerically optimized to produce a Gaussian beam that would maximally couple to an HE_{11} mode of a 31.75 mm diameter corrugated waveguide. A second mirror, interior to the copper block in Fig.

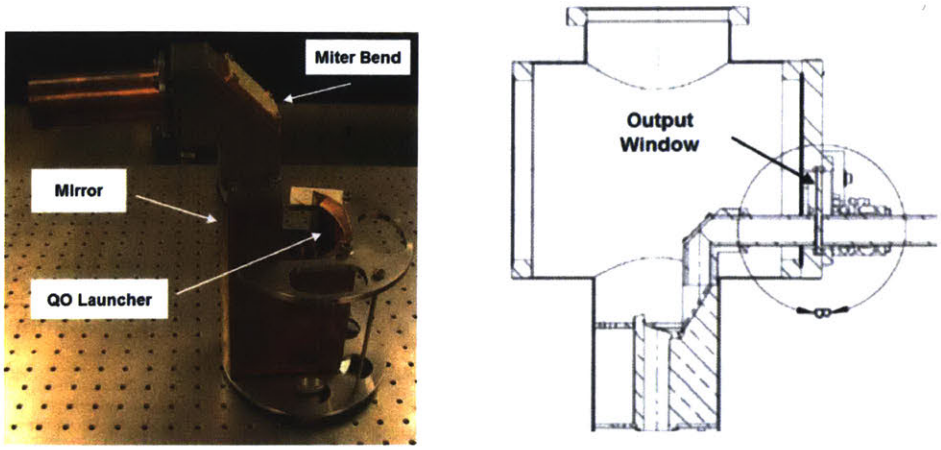

(a) Photograph CCR Internal Mode Coupler

(b) Schematic of Gyrotron Output

Figure 2-9: The internal mode coupler designed to couple the $TE_{22,6}$ operational mode of the gyrotron directly to the HE_{11} mode of a corrugated waveguide for output. The "QO Launcher" in (a) is short for quasioptical launcher.

2-9a, was simultaneously optimized. The two mirrors allowed the launcher to couple, in theory, 97.4% of the $TE_{22,6}$ power to the HE_{11} mode. About 1.3% of the power does not couple into the waveguide at all, and is scattered into the vacuum tube. The remainder of the power couples into other, undesirable modes of the corrugated waveguide.

It can be seen in Fig. 2-9a that the two optimized surfaces, the QO launcher and the mirror, were machined out of a single block of copper, along with the output taper of the gyrotron. This output system was designed to be coupled to the existing $TE_{22,6}$ cavity from Eunmi Choi's earlier PhD work [4]. A miter bend (a 90 degree bend in a waveguide) was used to direct the microwaves through the gyrotron window. As seen in Fig. 2-9b, on the outside of the window, further sections of corrugated waveguide were attached to the gyrotron to transport the microwaves to their intended destination.

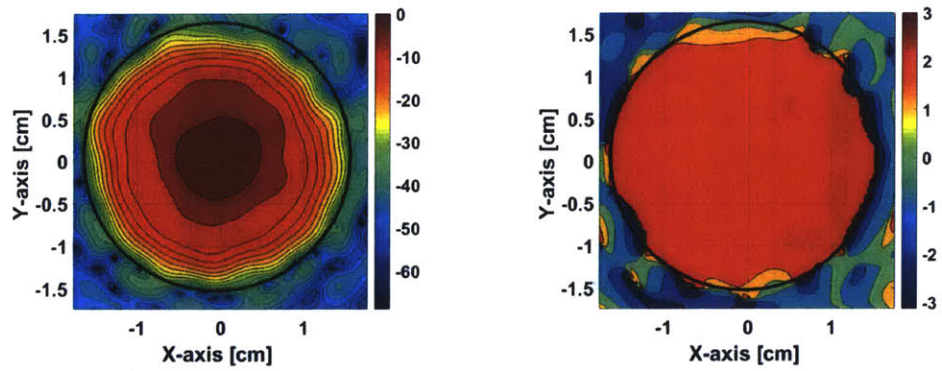

(a) Intensity (dB) (b) Phase (radians)

Figure 2-10: Measured output beam from the CCR internal mode converter on a low power test stand. The black circle indicates the boundary of the corrugated waveguide that forms the gyrotron output.

2.6.2 Low Power Testing

Prior to installing the output assembly in the gyrotron, the performance of the coupler was analyzed at low power at MIT using a vector network analyzer. $TE_{22,6}$ microwaves were fed into the mode launcher. The output intensity and phase were recorded with a two-dimensional scan. The HE_{11} mode content, and thus the performance of the mode launcher, was calculated using the method described in [37]. This measurement could be performed with greater precision at low power, and this eliminated effects due to any unwanted modes that could be excited in the gyrotron cavity during high power testing.

The output was measured to be 97.9%±0.3% in the HE_{11} mode, near the design value of 98.8%. The results of the output scan are shown in Fig. 2-10. In these images, the black circle indicates the location of the waveguide wall. The power shown outside the waveguide is down from the peak intensity by 40 dB, a factor of 10^{-4}. This is noise below the accuracy of the measurement.

2.6.3 High Power Testing

After low power testing, the CCR mode coupler was installed in the MIT MW gyrotron and tested at high power. This was benchmarked by comparison to the perfor-

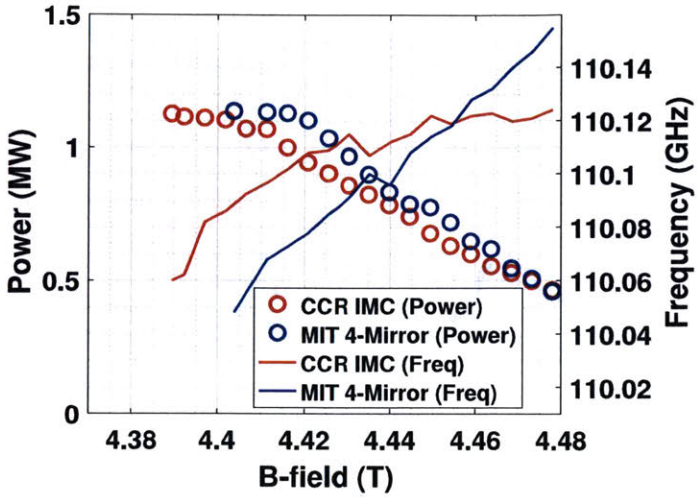

Figure 2-11: Comparison of the power and frequency output of the MIT MW gyrotron with either a four mirror quasioptical output section (blue) or the CCR internal mode coupler (red).

mance of the gyrotron with a four-mirror output connected to the same cavity. The performance of the mode coupler can be seen in Fig. 2-11.

The data in Fig. 2-11 was collected with a 96.7 kV, 43 A electron beam. With either the CCR mode coupler or a simple four-mirror system, the gyrotron achieved a peak power of 1.12 MW. There is, however, a measurable shift in the magnetic field at which the gyrotron is optimized. Installation of each output section required realignment of the gyrotron components, and the entire tube within the superconducting magnet to maximize performance and minimize electron beam interception. To avoid interception of the electron beam on the miter bend of the CCR mode coupler, the tube had to be placed in the magnetic field at a different angle from that which maximized the performance of the gyrotron with the four-mirror output section. This likely caused at least some of the discrepancy in performance versus magnetic field strength.

Another method of evaluating the performance of gyrotrons is a mode map, as seen in Fig. 2-12. The x-axis represents a sweeping of the field of the main superconducting magnet. A small supplementary solenoid is centered on the cathode of the MIG electron gun, allowing independent adjustment of the magnetic field at the cathode. This is varied to generate the y-axis of the mode map. As the main magnetic field is

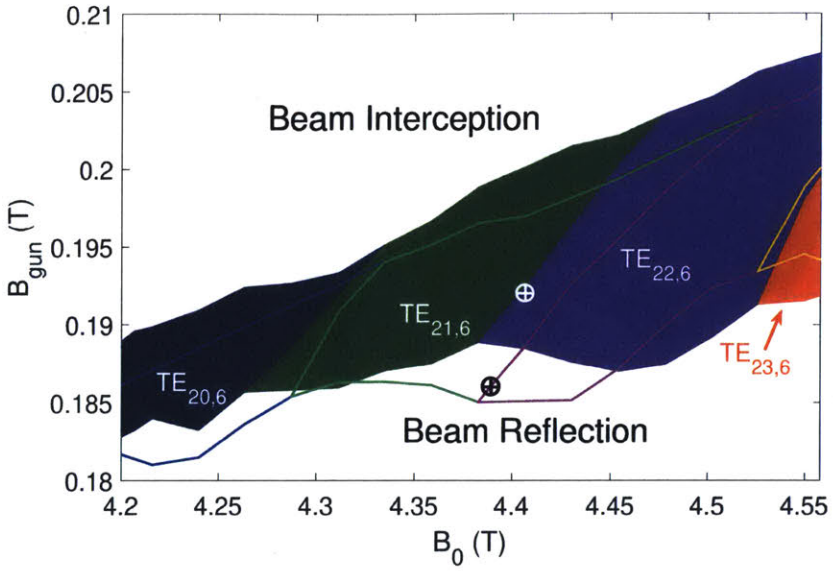

Figure 2-12: Mode map with four mirror launcher (filled areas) or CCR mode coupler (outlines). This map shows the mode excited in the gyrotron cavity by the electron beam as a function of magnetic field at the electron gun cathode (B_{gun}) and the field in the gyrotron cavity (B_0). The operational point of maximum output is indicated with a white plus (four mirrors) or a black plus (CCR mode coupler).

changed, the electron cyclotron frequency shifts, eq. 2.3, and the electron cyclotron wave is synchronous with different modes of the gyrotron cavity. As the ratio of the magnetic field at the cathode to the main magnetic field is adjusted, the radius of the electron beam in the gyrotron cavity, as well as the pitch factor, α, are adjusted. The greater the ratio of main magnetic field to the cathode magnetic field, the more the electron beam is compressed. If the beam is not compressed enough, it will strike (be intercepted) on a component of the gyrotron. This is the top region of the mode map. If the beam is compressed too much, the electrons in the beam with the greatest ratio of transverse to longitudinal kinetic energy will be reflected from the magnetic field, as all of their longitudinal energy is converted to transverse energy during beam compression. These reflected electrons strike the cathode of the MIG electron gun, disrupting its operation. This is the lower region of the mode map.

It can be seen in the mode map that, with either output section, the same modes are excited in the gyrotron cavity. It was a concern that the CCR mode coupler, designed to work in a narrow frequency range, could reflect significant microwaves

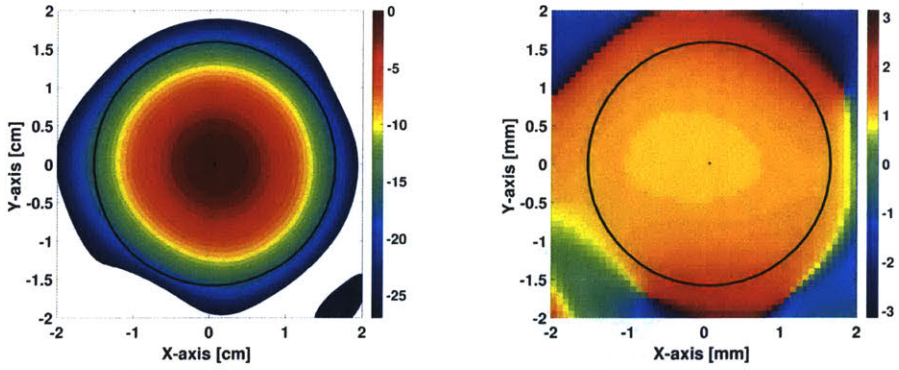

(a) Intensity (dB) (b) Phase (radians)

Figure 2-13: Measured output beam from the CCR internal mode coupler installed on the MIT 1.5 MW gyrotron. This was calculated from data taken at 3 distances from the gyrotron window. The phase retrieval method of [5] was used to calculate the intensity and phase at the window. The black circle indicates the boundary of the corrugated waveguide that forms the gyrotron output.

back into the gyrotron cavity, altering the response of the cavity for different modes. This turned out to not be a concern. With the CCR mode coupler installed, the "Beam Interception" region of the mode map is expanded, as the miter bend is near the expanding, spent electron beam. This is not a concern, because the highest efficiency parameters for operation are always found lower in the mode maps. In this mode map, the points of maximum power output are indicated with plus marks, white for the four mirror system, and black for the CCR mode coupler.

While installed on the gyrotron and operating at high power, the output pattern of the CCR mode coupler was again measured. The results are shown in Fig. 2-13. At high power, the output of the gyrotron was found to be 97.5%±1%, in agreement with the low power tests.

The CCR internal mode coupler performed as designed. It did not negatively affect the performance of the gyrotron, and it output a high purity HE_{11} mode into a corrugated waveguide. The installation of this output for the gyrotron proved to be beneficial to later experiments where the gyrotron was used for studies of dielectric multipactor. The experiment was necessarily located several meters from the gyrotron. Sections of waveguide were connected to the output of the gyrotron. This

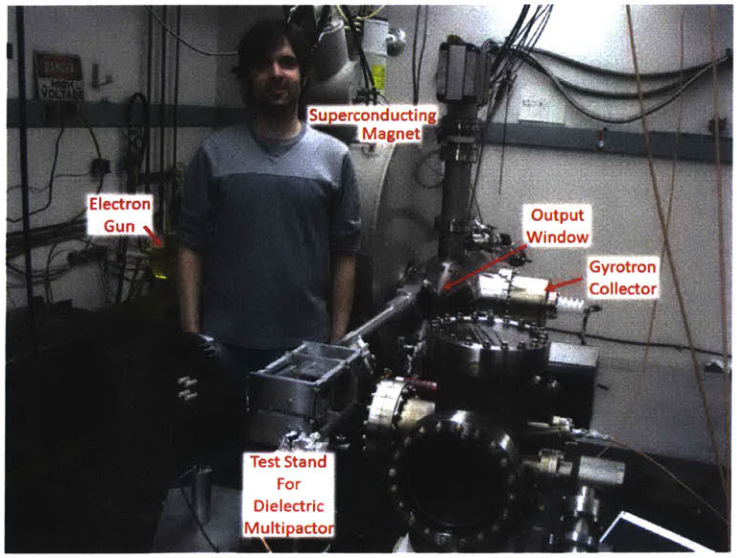

Figure 2-14: Photograph of the MIT 1.5 MW gyrotron with a 31.75 mm diameter corrugated waveguide connected to the output. In this setup, the waveguide carries the microwave power to an optical bench, where a test stand has been constructed for studying dielectric multipactor.

can be seen in the photograph of Fig. 2-14. This provided a surface to which optics could be aligned with far greater ease than alignment to a free space output several meters from the gyrotron.

Chapter 3

Introduction to Dielectric Multipactor

Multipactor is a vacuum discharge frequently observed in microwave systems, such as RF windows, particle accelerator structures, vacuum tube microwave sources, and RF systems on satellites. Multipactor is an electron avalanche event caused by secondary emission of electrons from a surface. Seed (primary) electrons that gain energy from an RF field may impact a surface and release a larger number of secondary electrons. The secondary electrons may subsequently be accelerated by the RF field and be made to impact again, yielding an even greater number of secondary electrons, et cetera. These discharges can take place on conducting surfaces, dielectric surfaces, on a single surface, or between two surfaces.

3.1 Vaughan's Model of Secondary Electron Yield

When an electron impacts a surface, it may be captured by the surface, reflect from the surface, or liberate additional, secondary electrons. The secondary electron yield (SEY) is the average number of free electrons that can be expected to result from the impact of a primary electron. Empirically, it has been found that a plot of SEY versus electron impact energy and impact angle has a somewhat universal shape, independent of material [38–40]. This has allowed the development of a simple model

to predict SEY from impacting electrons given a few, measurable parameters for the material. Most theoretical work published thus far on multipactor on dielectric surfaces has made use of Vaughan's model of secondary electron yield. This simple model is preferred, because, for dielectric materials in particular, secondary electron emission properties are not known to great accuracy, and experimental data is lacking to constrain more sophisticated models [41].

Vaughan's model, described in detail in 1989 [42] and revised in 1993 [7] is defined by Eq. 3.1 - Eq.3.4. In this definition, V_i is the electron impact energy, V_{max} is the impact energy at which SEY is maximized for normal impacts (0° impact angle), and δ_{max} is the peak SEY at normal incidence. Equation 3.1 defines how these values change as a function of impact angle, θ. The smoothness parameter, k_s can range from 0 for textured carbon to 1.5 or 2 for a highly polished, impeccably clean surface. In the absence of specific data, this parameter is assigned a value of $k_s = 1$, representing a typical dull surface. The threshold energy, V_0, is the impact energy below which no secondary electrons are produced. This is assumed to be 12.5 eV in the nominal model. However, experimental data at very low impact energies is lacking, especially for dielectric materials where charging of the surface would complicate the measurements. For simplicity, most publications on the theory of multipactor on a dielectric surface set this value to 0 eV. The effect of a nonzero V_0 is explored in chap. 4.

$$\begin{aligned} V_{max}(\theta) &= V_{max}\left(1 + \frac{k_s\theta^2}{2\pi}\right) \\ \delta_{max}(\theta) &= \delta_{max}\left(1 + \frac{k_s\theta^2}{2\pi}\right) \end{aligned} \tag{3.1}$$

$$\nu = \frac{V_i - V_0}{V_{max}(\theta) - V_0} \tag{3.2}$$

$$\frac{\delta(\theta)}{\delta_{max}(\theta)} = \left(\nu e^{1-\nu}\right)^k \tag{3.3}$$

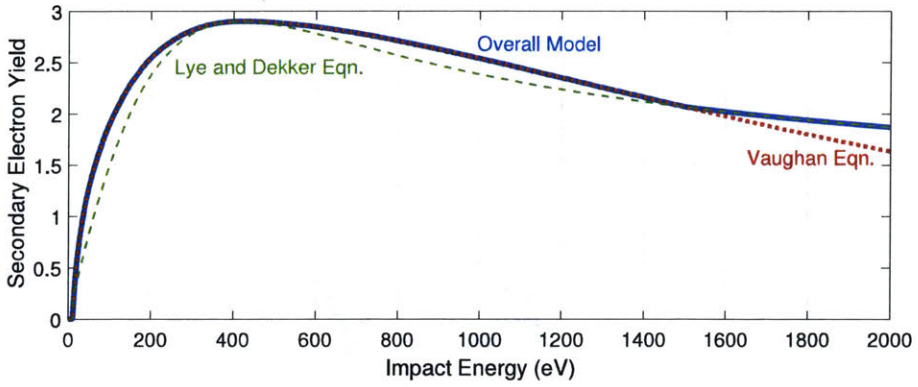

Figure 3-1: Vaughan's empirical model of secondary electron yield. Example shown for fused quartz with $\delta_{max} = 2.9$ and $V_{max} = 420$ eV.

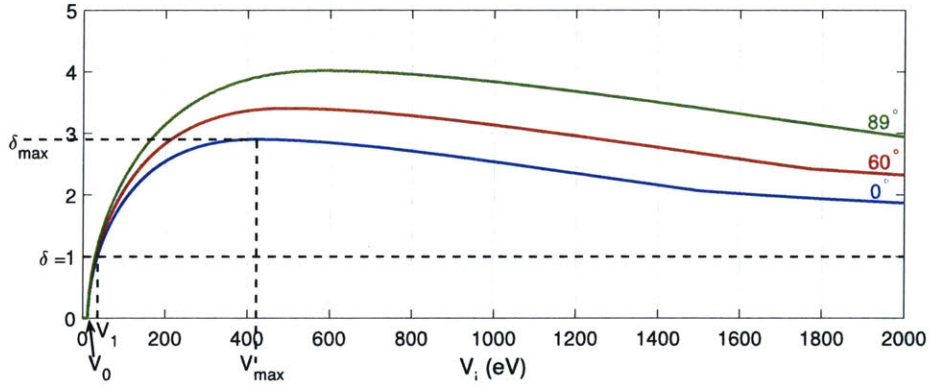

Figure 3-2: Definition of variables in Vaughan's empirical model of secondary electron yield.

$$k = k_1 = 0.56, \text{ for } \nu < 1$$
$$k = k_2 = 0.25, \text{ for } \nu > 1 \tag{3.4}$$

At very high electron energies, Eq. 3.3 falls off too rapidly, compared to experimental data. The empirical model is supplemented by an earlier empirical SEY model of Lye and Dekker [43], given in Eq. 3.5. The overall model used throughout studies of multipactor is shown in Fig. 3-1. It transitions between Eq. 3.3 and Eq. 3.5 where they intersect at high impact energy (near 1500 eV in Fig. 3-1).

$$\frac{\delta(\theta)}{\delta_{max}(\theta)} = 1.379 \frac{1 - \exp\left(-\left(1.844 V_i / V_{max}\right)^{1.35}\right)}{\left(1.844 V_i / V_{max}\right)^{0.35}} \tag{3.5}$$

Figure 3-1 shows theoretical SEY behavior for fused quartz. Figure 3-2 visually

Material	δ_{max}	V_{max} (eV)	Normal V_1 (eV)	Grazing V_1 (eV)	Source
Alumina	1.5 - 9	350 - 1300	87.9 - 21.9	64.8 - 19.8	[44]
Lucalox Alumina (Polished)	6.4	650	21.1	19.2	[45]
Sapphire	6.4	650	21.1	19.2	[45]
Fused Quartz	2.9	420	36.2	30.5	[44]
Crystal Quartz	2.4	400	45.0	36.8	[44]
Silicon	1.1	250	137	83.8	[44]

Table 3.1: Table of secondary electron yield parameters for materials tested. Properties of alumina vary dependent upon the material density, purity, and surface condition. Alumina used in this thesis was high purity, fine grained (99.8% - 99.9% sapphire density), and optically polished. The reported values for polished Lucalox alumina were assumed, giving identical theoretical behavior to sapphire.

defines the variables of Vaughan's model. In addition to the variables in the explicit definition, the first crossover energy, V_1 is defined as the lowest energy at which SEY= 1 for a particular material, at normal incidence. This value will prove to be important in the theory of how a multipactor discharge forms and reaches equilibrium. There also exists a second crossover energy, V_2 where the SEY falls below 1 at higher impact energy, off the right side of the plot. Also shown in Fig. 3-2 is the angular dependence of SEY, as defined by Eq. 3.1. An electron impacting a surface at a grazing angle can yield a significantly greater number of secondary electrons than a perpendicular impact. The secondary electron emission properties of some materials of interest for high power microwave and accelerator devices are shown in Table 3.1.

3.2 Multipactor

3.2.1 Two-Surface Multipactor

Multipactor phenomenon is broadly divided into two classes: two-surface multipactor and single-surface multipactor. Two-surface multipactor, the first historically to be documented and studied, is described here for completeness, though it was not a subject of study in this thesis. Two-surface multipactor is a resonance phenomenon

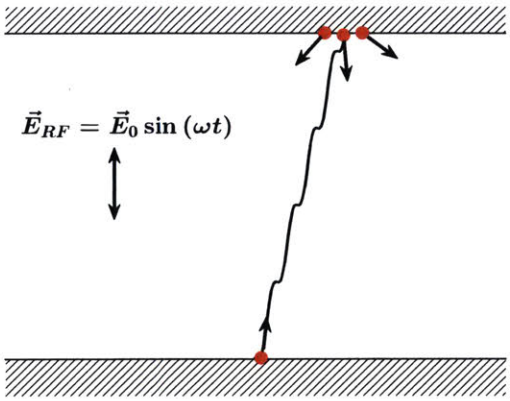

Figure 3-3: Geometry of a simple, two-surface multipactor.

consisting of a sheet-like cloud of electrons oscillating between two surfaces in the presence of an RF field. The electron cloud is driven by and synchronous with the RF field. The synchronous condition is that the transit time between the two surfaces is an odd number of half cycles of the RF, such that at each alternate impact, the electron cloud sees the same conditions in reverse. The basic geometry is shown in Fig. 3-3. Phase focusing of the electron cloud with the RF field counteracts the dispersive effects of varied secondary electron launch energy and space charge (electron-electron repulsion). This can lead to a steady-state electron cloud oscillating in the gap between two surfaces. Further background on the well-studied (with metallic surfaces) two-surface multipactor can be found in review papers [41, 46].

3.2.2 Single-Surface Multipactor

All studies of multipactor presented in this thesis are single-surface multipactor, where secondary electrons are directed back to the surface from which they are emitted by means of external electric and/or magnetic fields. In the oft-studied single surface multipactor with a metallic surface, an oscillatory electric field must be normal to the surface. Electrons launched within a proper phase of a strong enough RF field will gain sufficient energy to yield more than one secondary electron when returned to the surface. On a conducting surface, this, like two-surface multipactor, is a

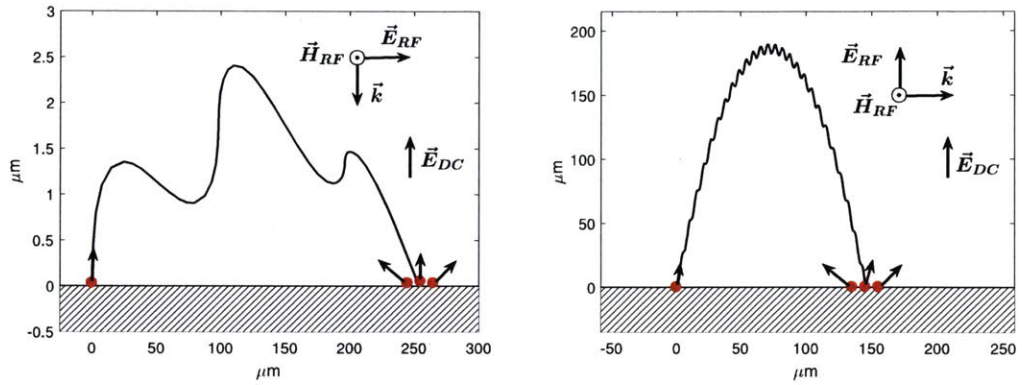

(a) Tangential E-Field

(b) Normal E-Field

Figure 3-4: Example trajectories of electrons launched from the surface of a dielectric in the presence of a traveling TEM wave with an electric field either tangential to (a) or normal to (b) the dielectric surface. This example was calculated with 150 kV/m DC electric fields and an RF electric field of 40 MV/m in (a) and 10 MV/m in (b). The time to impact is 23 ps and 237 ps, respectively.

resonant phenomenon. Electron trajectories must be synchronous with the RF field and return to the surface in an even number of half cycles, so that the secondary electrons see identical launch conditions, leading to the exponential growth of the electron population. Essentially, this is the same physics as two-surface multipactor, with electron trajectories folded back on themselves.

3.2.3 Dielectric Multipactor

In the following chapters of this thesis, specifically presented is a study of single-surface multipactor on dielectric (nonconducting) surfaces. The dielectric surface complicates the case of single-surface multipactor. A nonconducting surface allows for the presence of tangential surface electric fields in addition to the normal fields. Furthermore, as secondary electrons are stripped from a dielectric surface, the surface will develop a positive charge. Multipactor on a dielectric will tend to self-develop a DC electric field to confine the cloud of electrons near the surface and draw them back to impact. In the case of a purely tangential RF electric field (as in an RF window), the time of flight of secondary electrons depends only upon their launch velocity and

the strength of the DC field. This timing independence from the RF electric field removes any resonance condition, and greatly widens the parameter space in which dielectric multipactor can occur [6, 46]. As we will see in chap. 4, in the case of a normal RF electric field, a resonance condition still exists for sustained multipactor. However, in this geometry, the dielectric will tend to charge to the precise value required to sustain an electron cloud with average trajectories lasting one RF cycle. Figure 3-4 shows example electron trajectories in the presence of a traveling RF wave propagating either through, (a), or along, (b), a dielectric surface. It can be seen in Fig. 3-4a that, with only a tangential RF E-field, electrons remain within a few microns of the surface. For illustrative purposes, the example trajectories are calculated with a DC electric field much weaker than the RF electric field, so that the electron takes multiple RF cycles to return to the dielectric surface. These trajectories represent a stage in a developing multipactor, where the dielectric has not yet charged enough to yield a steady-state electron cloud.

3.2.4 A Brief History of Multipactor

Though observed in 1924 [47], multipactor as a phenomenon of electron multiplication was first identified and described by P. T. Farnsworth in 1934 [48]. Farnsworth sought to exploit multipactor as a means of amplifying electronic signals, particularly to enhance the sensitivity of early television cameras [49]. An illustrative schematic tube making use of two-surface multipactor to amplify current is shown in Fig. 3-5. Plate-like cathodes are at the left and right boundaries of the tube. The space between is filled with a hollow cylindrical anode. The entire tube is placed in a horizontal solenoid, providing a DC magnetic field that partially inhibits radial motion of the electrons. The cathodes are driven with an RF potential (at 50 MHz in Farnsworth's devices) and multipactor occurred as electrons oscillated horizontally between the two cathodes. The anode carried a small positive charge to collect a portion of the cloud of electrons, generating a large current from a modest positive voltage. Farnsworth originally coined the term multipactor as the name of the vacuum tubes he developed as current amplifiers (from "AC Electron Multiplier"). By the 1950's,

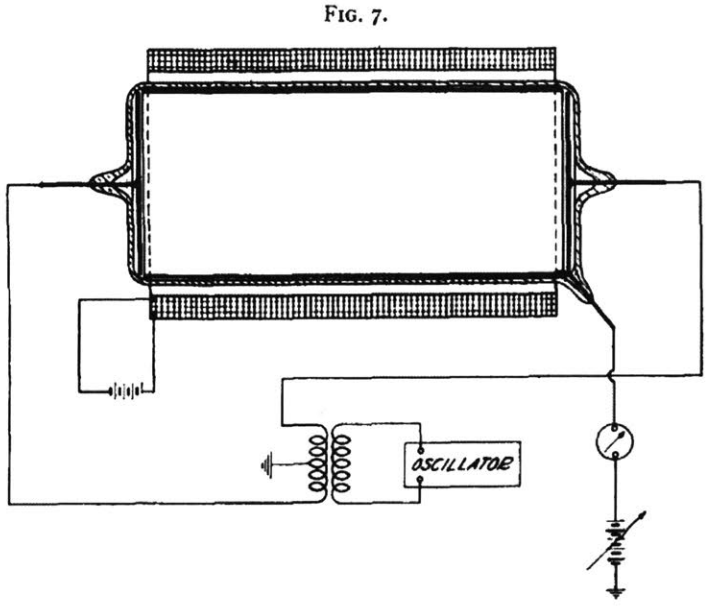

Figure 3-5: An illustrative schematic of a vacuum tube that uses multipactor to amplify current.

the term had transferred from the tubes themselves to the physical phenomenon upon which Farnsworth based his invention [50].

Multipactor as a useful phenomenon for current amplification has not had lasting applications. It has, however, been studied for use in the design of electron guns [51,52]. Multipactor has also been found useful as a protection mechanism for sensitive electronics [53–55], where multipactor is used to dissipate excess RF energy.

In the majority of modern applications where multipactor occurs, it is an undesirable and destructive phenomenon. Contemporary applications in which multipactor arises include in microwave sources and RF windows [56–59], accelerator cavities [60–64], and spacecraft antennas [65–68]. In these devices, multipactor manifests itself as localized heating at the site of the electron impacts. This heating can itself melt or destroy vacuum surfaces, or heat the surface enough to cause outgassing that leads to arcing in regions of high electric field [69]. The absorption of energy by the electron cloud reduces the quality factor of resonant cavities, decreasing efficiency of microwave sources and RF accelerators. The charging of dielectric or ceramic

windows enhances the heat deposition of the multipactor process, and can result in cracking or puncturing of RF windows [70–73]. Modern studies of multipactor focus on understanding the phenomenon, so that it can be effectively predicted and subsequently suppressed or avoided.

3.3 Prior Studies of Dielectric Multipactor at Frequencies up to 11 GHz

Currently, only a handful of experiments exist to provide clear data on the behavior of multipactor on dielectric materials. This is at least in part because the unique nature of multipactor on a dielectric surface was not well recognized before the development of a theory of multipactor that included dielectric charging in 1998 [6]. Ivanov et al. have experimentally measured the minimum surface RF electric field (5.8 MV/m) to initiate a multipactor on fused quartz in a window configuration, with a tangential RF electric field at 9.4 GHz [74]. Additionally, they placed the sample at different gradients of electric field in a standing wave cavity, to qualitatively document the effect of the ponderomotive force on the multipactor. It was demonstrated that the threshold value of RF electric field for initiating multipactor could be raised or lowered by imposing an external DC field on the sample, and that the ponderomotive force manifested itself in a similar manner. At a low frequency of 1.95 GHz, a data point of multipactor threshold (0.54 MV/m) and power absorption (~3%) on a fused quartz plate as a window in a TE_{01}-moded rectangular waveguide (with tangential RF electric field) was measured in 2012 [75].

A series of experiments aimed at developing a dielectric-loaded accelerating structure, consisting of a dielectric lined waveguide to provide phase velocities below the speed of light, have provided data on multipactor in a TM_{01} mode at 11.424 GHz [76]. In this geometry the RF surface field approaches a normal angle with the surface of the dielectric. Initial experiments documented the multipactor threshold field on an alumina surface, 1 MV/m, and recorded the power absorbed by the multipactor as a

function of incident surface field strength. This showed a nearly linearly increasing trend in the fraction of the power absorbed versus the surface electric field. Later experiments attempted to suppress the multipactor, using a coating of titanium nitride to lower the SEY of the material [77]. This coating raised the multipactor threshold to 1.6 MV/m and significantly reduced the fraction of power absorbed once multipactor onset had occurred.

No studies on any material or geometry have been performed above 11 GHz. New, high power microwave sources and applications are being developed at frequencies of 100's of GHz, and multipactor may be a concern. Prior to the work of this thesis, it was unknown precisely how the limited results at 2-11 GHz scale to much higher frequencies.

3.4 Overview of Existing Theory

Since the properties of dielectric multipactor were theoretically probed in [6], a multitude of theory has been published to predict behavior and extrapolate from the meager existing experimental data. The original paper [6] made predictions about how multipactor threshold fields scale with material properties and that the threshold scales linearly with RF frequency. A follow up paper [22] predicted that, in RF window geometry, the fraction of absorbed RF power is independent of the strength of the RF surface fields, and on the order of 1%. Predictions of absorbed RF power are beneficial for cases where multipactor cannot be completely avoided, to determine the heat load that must be borne by the device. A more involved analytical study was performed by Sakharov et al. suggesting that the absorbed power is logarithmically dependent upon the amplitude of the surface RF electric field [75]. A series of papers by Sazontov et al. has explored the role of the RF magnetic field in dielectric multipactor [78–81]. This turns out to predict several subtle and a few significant effects, and will be discussed in detail in chap. 4.

After the publication of experimental data on dielectric loaded accelerator experiments, several papers were published using Monte Carlo calculations [82, 83] to

reproduce the experimentally shown relationship between the fraction of absorbed power vs incident RF power. A later paper by Sakharov et al. [84], further used a PIC simulation to examine multipactor on a dielectric as a continuous function of angle between the dielectric surface and the RF E-field. In this paper, it is suggested that an intermediate angle of electric field (20° away from tangential E-fields for fused quartz) could be employed to minimize the amount of power deposited on the dielectric surface by the cloud of electrons.

What is lacking from this body of theoretical work is a means of accurately predicting threshold fields for the onset of dielectric multipactor, in any geometry. Thus far, studies have concentrated on understanding the steady-state equilibrium that a multipactor discharge reaches. The models used cannot be extrapolated down to the realistic initial conditions at the onset of multipactor, with few seed electrons and no prior charging of the dielectric surface. It has been suggested in [6] that the threshold field should scale linearly with frequency. If such behavior could be experimentally verified, it would at least allow extrapolation from previous experimental data as new technology and applications continue to push available microwave sources to ever higher frequencies and powers.

3.5 Goals of This Work

The experimental work presented in the following chapters seeks to bolster the available experimental data on dielectric multipactor, and to evaluate theoretical predictions that remain untested since research began in this field in earnest with the 1998 paper by Kishek and Lau. The experiment sought to measure multipactor thresholds for multiple materials of interest with MIT's high power, 110 GHz microwave source. These tests, an order of magnitude higher in frequency than existing data, allow testing of predicted frequency scalings. Separate experiments were designed to independently study multipactor with either normal or tangential RF electric fields, as the two regimes theoretically produce very different steady state behavior. Additionally, the experiments were designed so that they could be operated over a wide

range of incident microwave powers, allowing evaluation of theoretical scaling and testing if the behavior seen in 11 GHz accelerating structures extends into the millimeter wave regime ($f \gtrsim 100$ GHz). Finally, all tests were performed on multiple materials, allowing study of how dielectric multipactor depends upon the properties of materials commonly used in microwave devices.

Chapter 4

Dielectric Multipactor Theory

4.1 Monte Carlo Model Based on the Theory of R. A. Kishek and Y. Y. Lau

The first modern publications on the theory of dielectric multipactor were published in 1998 by the group of Y. Y. Lau at the University of Michigan [6, 22]. These publications use a Monte Carlo simulation to study dielectric multipactor with a tangential electric field. The majority of dielectric multipactor theory papers that have been published in subsequent years have built upon this work, adding additional physics or complicating the geometry. This model is described here, and used as a base from which the dynamics of dielectric multipactor is explored.

4.1.1 Monte Carlo Model

Figure 4-1 shows the geometry of a multipactor simulation with a tangential electric field. The initial launch velocity is v_0. The angle between the initial velocity and the surface is ϕ. Rotation of the launch vector about the x-axis is α. The angle of impact with the surface is θ. For this initial model, the system is reduced to two dimensions by setting α to zero and ignoring the magnetic field.

This model, and the majority that came after it, use a simplified version of Vaughan's original 1989 model of secondary electron yield [42], neglecting his later

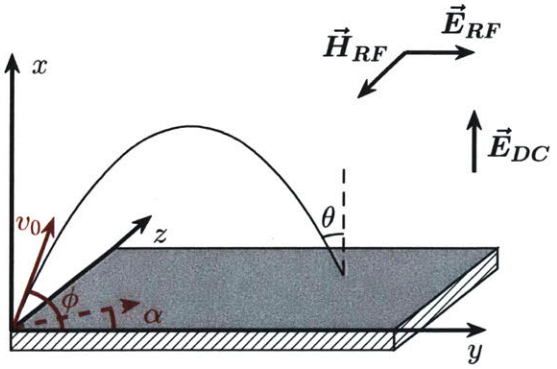

Figure 4-1: Geometry used in Monte Carlo simulations.

revision that was laid out in section 3.1. In the simplification, the threshold impact energy, V_0 is set to zero. The transition to the model of Lye and Dekker, Eq. 3.5, is neglected. The dependence upon impact angle, θ, of the simplified model is given in Eq. 4.1. The dependence of secondary electron yield, δ, upon impact energy, V_i, is given in Eq. 4.2 - Eq. 4.4.

$$\begin{aligned} V_{max}(\theta) &= V_{max}(0)\left(1+\frac{\theta^2}{\pi}\right) \\ \delta_{max}(\theta) &= \delta_{max}(0)\left(1+\frac{\theta^2}{2\pi}\right) \end{aligned} \tag{4.1}$$

$$\nu = \frac{V_i}{V_{max}(\theta)} \tag{4.2}$$

$$\frac{\delta(\theta)}{\delta_{max}(\theta)} = \left(\nu e^{1-\nu}\right)^k \tag{4.3}$$

$$\begin{aligned} k &= k_1 = 0.62, \text{ for } \nu < 1 \\ k &= k_2 = 0.25, \text{ for } \nu > 1 \end{aligned} \tag{4.4}$$

The growth rate of a multipactor discharge is estimated by following macroparticles over a large number of impacts in a Monte Carlo simulation. Each time a macroparticle is launched from the dielectric surface, it is assigned a random kinetic energy, $V_0 = \frac{1}{2}mv_0^2$, and angle, ϕ, according to the distributions in Eq. 4.5 and Eq.

4.6.

$$f(V_0) = \frac{V_0}{V_{0m}^2} e^{-V_0/V_{0m}} \tag{4.5}$$

$$g(\phi) = \frac{1}{2} \sin\phi \tag{4.6}$$

This is a Rayleigh probability distribution in velocity, expressed in terms of energy. V_{0m} is the peak of the distribution of emission energies. The expected value of V_0 is $2V_{0m}$. Secondary electrons are emitted with energies on the order of the work function of the material [44]. For all simulations presented in this chapter, the energy distribution peak is set to $V_{0m} = 0.005V_{max}$ (e.g. 2 eV for $V_{max} = 400$ eV). See Table 3.1 for values of V_{max}. The angle distribution function, Eq. 4.6, ranges from 0 to π.

An electron launched at time $t = 0$ from the dielectric surface at $x = 0$ and $y = 0$ with a velocity v_0 and angle with y-axis ϕ experiences a force due to the the RF electric field, $m\ddot{y} = -eE_{RF}\sin(\omega t + \varphi)$. If the dielectric is charged, the electron is affected by a restoring force, $m\ddot{x} = -eE_{DC}$. From these simple equations of motion, you can determine the transit time for the electron to return to the dielectric surface, Eq. 4.7. Note that with a parallel RF electric field, the transit time is independent of any influence of the RF field.

$$\tau = \frac{2mv_0 \sin\phi}{eE_{DC}} \tag{4.7}$$

The energy of the electron upon impacting the surface is:

$$\begin{aligned} V_{ix} &= \frac{1}{2} m v_0^2 \sin^2\phi \\ V_{iy} &= \frac{1}{2}\left(\frac{eE_{RF}}{\omega}\right)^2 \left[\cos\left(\frac{2mv_0\sin\phi}{e\,(E_{DC}/\omega)} + \varphi\right) - \cos\varphi + \frac{mv_0\cos\phi}{e\,(E_{DC}/\omega)}\right]^2, \end{aligned} \tag{4.8}$$

where V_{ix} and V_{iy} are the x and y components of the impact energy. The impact angle is given by Eq. 4.9.

$$\theta = \arctan\left(\sqrt{\frac{V_{iy}}{V_{ix}}}\right) \tag{4.9}$$

The equations presented up to this point are identical to the equations derived in the Kishek and Lau paper [6]. We now present our Monte Carlo code and the results obtained with it. This will benchmark our code against the results obtained previously in [6], prior to extending our theory to new regimes.

4.1.2 Multipactor Susceptibility Diagram

For the Monte Carlo simulation, many macroparticles are launched, distributed evenly in initial RF phase, φ. After the first impact, the impact energy and angle yields a value of secondary electron yield, δ. The RF phase is updated, and the macroparticle is once again launched from the surface, with a new random velocity and launch angle. The average value of secondary electron yield is computed with a geometric mean, as it is a multiplicative growth rate. The average impact energy is computed with an arithmetic mean. If a macroparticle is allowed to bounce n times, the average secondary electron yield for that macroparticle is $\delta_m = (\delta_1 \cdot \delta_2 \ldots \delta_n)^{1/n}$ and the average impact energy is $V_{im} = (V_1 + V_2 + \ldots V_n)/n$. To generate a multipactor susceptibility diagram, for each value of E_{RF} and E_{DC}, the value of secondary electron yield is averaged over all macroparticles launched, again using a geometric mean. By plotting this mean secondary electron yield, $\bar{\delta}$, as a function of E_{RF} and E_{DC}, regions of parameter space susceptible to multipactor can be identified, where $\bar{\delta} > 1$. Figure 4-2 shows a contour plot of $\bar{\delta}$ for an example material with $\delta_{max} = 2.0$.

A multipactor susceptibility diagram is shown in Fig. 4-3. In this diagram are plotted contours where $\bar{\delta} = 1$ for a variety of values of δ_{max}. Solid lines are reproduced directly from [6], and dotted lines are an attempt to recreate the calculation using the equations described in this section. For each value of δ_{max}, there is an upper and lower boundary. Between these boundaries, $\bar{\delta} > 1$, and multipactor should occur. The agreement between our Monte Carlo code and the results of [6], as shown in Fig. 4-3, is very good.

The shape of the boundaries on the multipactor susceptibility plot can be understood as follows. For any given value of E_{RF} and E_{DC}, the growth rate is determined by the mean secondary electron yield, averaged over random emission energy and

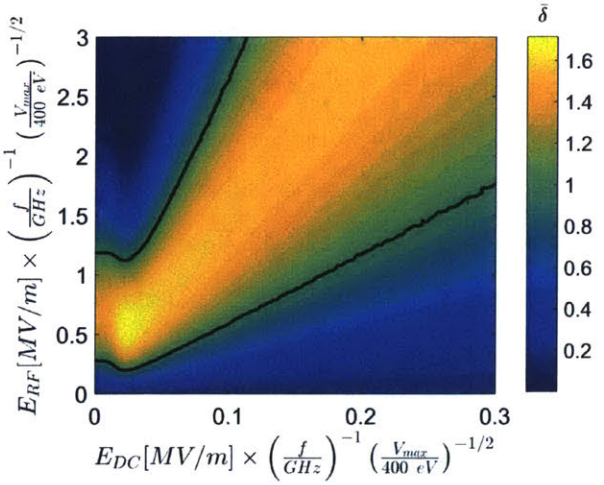

Figure 4-2: Contour plot of the mean secondary electron yield for an example material with $\delta_{max} = 2.0$. The $\bar{\delta} = 1$ contour is marked in black.

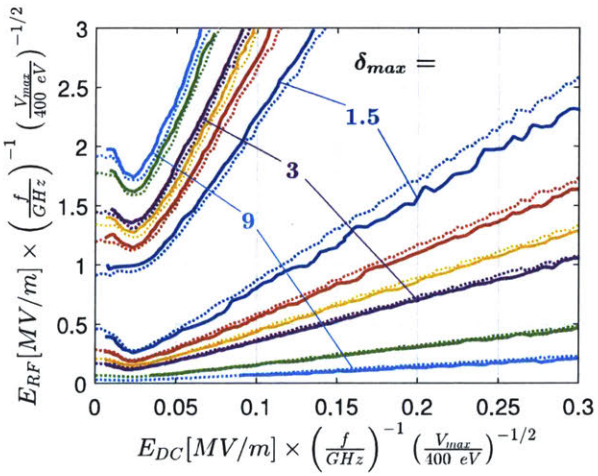

Figure 4-3: Multipactor susceptibility region boundaries for $\delta_{max} = 1.5, 2.0, 2.5, 3.0, 6.0, 9.0$. Solid lines are reproduced from [6]. Dotted lines are generated using the Monte Carlo technique outlined in section 4.1.

the launch angle distributions. The lower bound is where the mean electron impact energy is approximately equal to V_1, the first crossover energy defined in Fig. 3-2. At very high impact energy, the secondary electron yield will again fall below 1 at V_2, the second crossover energy. This is off the right of the plot in Fig. 3-2. The upper bound is where the mean electron impact energy is close to V_2. An increase in the magnitude of the RF electric field will increase the average amount of energy an electron gains before impacting. An increase in the magnitude of the DC electric field will decrease the transit time of an electron, eq. 4.7. If the average electron transit time is short compared to the RF period, as is the case at x-axis values greater than 0.04 in Fig. 4-3, this will decrease the mean electron impact energy.

In [22], the model of [6] was used to predict power absorption on a dielectric RF window with tangential surface electric fields. Discussion of this aspect of the theory will be put off until section 4.4, so that it can be examined at the same time as power absorption with normal surface electric fields.

Note that this model will break down at very low electric fields. Especially as the DC electric field tends toward zero, electron transit times grow to seconds and the trajectories span meters from the dielectric surface. In any real device, such electrons are lost from the multipactor region. In the original publication, no attempt was made to extend this model toward zero DC fields, as can be seen in the extent of the solid lines in Fig. 4-3. The zero DC field case will be further discussed in section 4.5.

4.1.3 Scaling Laws from the Kishek and Lau Model

A notable feature of this theory is the predicted linearity of the phenomenon with frequency. This comes directly from the equations of motion of this particularly simple geometry. Other than material parameters, Vaughan's model of SEY depends only upon the impact energy, V_i, and impact angle, θ, of an incident electron. It can be seen in Eq. 4.8 that, in the expression for impact energy, the strength of the RF field appears only in the form E_{RF}/ω. Likewise, because the transit time depends inversely on the DC electric field, the strength of the DC electric field only appears in the expression for impact energy in the form E_{DC}/ω. Other than this, the impact

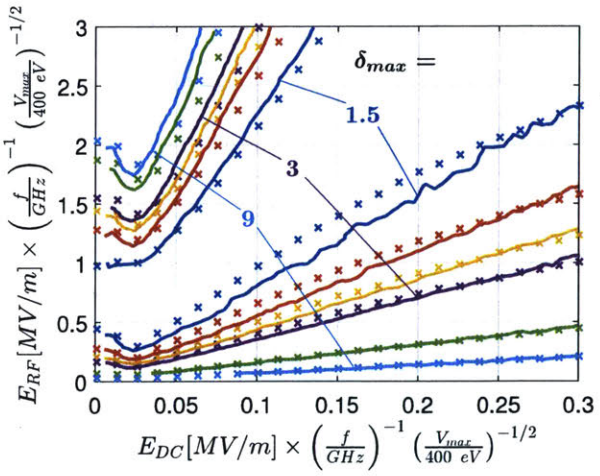

Figure 4-4: Multipactor susceptibility region boundaries. Solid lines are reproduced from [6]. "x" marks are generated using the approach outlined in section 4.2.1.

energy is independent of the RF oscillation frequency. This frequency scaling can also be shown to hold, approximately, in the same tangential electric field geometry with the inclusion of an RF magnetic field [80], though this model neglects the effects of RF phase focusing that arise from successive impacts of secondary electrons.

For example, in going from X-Band (8-12 GHz) to W-Band (75-110 GHz), the electric field required for the onset of a multipactor discharge, which is predicted to increase linearly with frequency, increases by nearly a factor of ten. This predicted scaling is a topic of major interest in this research, which is the first effort to measure these effects in W-Band.

The simplified version of Vaughan's model of SEY, Eq. 4.2 - Eq. 4.3, also leads to a scaling of electric field with the material property V_{max}. Assuming $V_0 = 0$, the secondary electron yield of an electron is only dependent upon initial velocity v_0, launch angle ϕ, launch RF phase φ, and the terms $E_{RF}/\left(\omega V_{max}^{1/2}\right)$ and $E_{DC}/\left(\omega V_{max}^{1/2}\right)$.

4.2 Extending the Kishek and Lau Model

4.2.1 Alterations to Monte Carlo Underpinning

The first alteration to the base model of Kishek and Lau was to tweak the math to allow for some electrons to be lost. Loss of electrons may be due to either electrons drifting too far from the system or impacting with energy below a nonzero V_0. The first step in the Monte Carlo simulation is the same as above. For the first bounce, m macroparticles are launched from the dielectric surface with random values of initial velocity, launch angle, and evenly distributed in RF phase, φ. Macroparticle trajectories were tracked to 100 RF cycles, after which macroparticles that had not impacted were assigned an SEY of $\delta = 0$. Macroparticles that impacted with less than V_0, nominally 12.5 eV in Vaughan's model, were also assigned $\delta = 0$. Macroparticles that impacted to yield nonzero δ had their charge adjusted and the RF phase of their impact recorded. A probability distribution of final charge versus final RF phase was fit to a histogram of the macroparticles. For the subsequent bounce, m macroparticles were launched with random energy, launch angle, and random RF phase distributed according to the probability distribution of the results of the previous bounce. In this manner, the total number of macroparticles in the calculation was maintained, but the RF phase distribution was allowed to evolve.

Mean secondary electron yield, $\bar{\delta}$ was calculated as a geometric mean in the Kishek and Lau model. A single value of 0 in a data set renders the geometric mean equal to 0. To allow for some loss of electrons, but still generate values that were directly comparable to the Kishek and Lau model, Eq. 4.10 was used. This is a geometric mean over all nonzero δ, multiplied by the fraction of δ that are nonzero. This hybrid between a geometric and arithmetic mean was chosen so that, as electron losses go

to zero, the results of the Kishek and Lau model are recovered.

$$\text{total macroparticles} = m$$

$$\text{fraction of macroparticles with nonzero } \delta = \chi$$

$$\bar{\delta} = \chi \left(\Pi_{i=1}^{\chi m} \delta_i\right)^{1/(\chi m)} \text{ (over nonzero } \delta_i) \tag{4.10}$$

To allow for the inclusion of a magnetic field, the simulation was expanded to three dimensions, using all the parameters shown in Fig. 4-1. For every launch of a macroparticle, the new angle α, rotation about the x axis, was randomly generated from a uniform distribution. The geometry of a tangential RF electric field, a normal DC electric field, and no magnetic fields is the only geometry for which an exact analytical solution for electron impact time and energy exists. To use the same code for a variety of geometries, including normal or tangential electric fields and magnetic fields, equations of motion were not analytically evaluated as in the Kishek and Lau model. Particle motion was tracked by numerically integrating the equations of motion with the Dormand-Prince Runge-Kutta method [85].

The code for this altered Monte Carlo simulation was benchmarked against the original results of the Kishek and Lau model. Figure 4-4 shows the original results as solid lines. The boundaries of the multipactor susceptibility regions calculated with the altered model are denoted with "x" marks. These benchmarking calculations used the simplified, unrefined Vaughan model of secondary electron yield (Eq. 4.1 - 4.4). At each point on the plot, 100 thousand macroparticles were tracked. The time limit for impact was 100 RF cycles. Tracking the macroparticles through 25 bounces was sufficient for results to converge.

4.2.2 Effects of Using the Full, Refined Vaughan's SEY model

The majority of publications on theory of dielectric multipactor have used the simplified version of Vaughan's original 1989 model of SEY, Eq.4.1 - Eq. 4.4. Figure 4-5 shows how the simplified model differs from Vaughan's 1993 revision, Eq. 3.1 - 3.4. This difference is shown at grazing incidence ($\theta = 90°$), appropriate to ge-

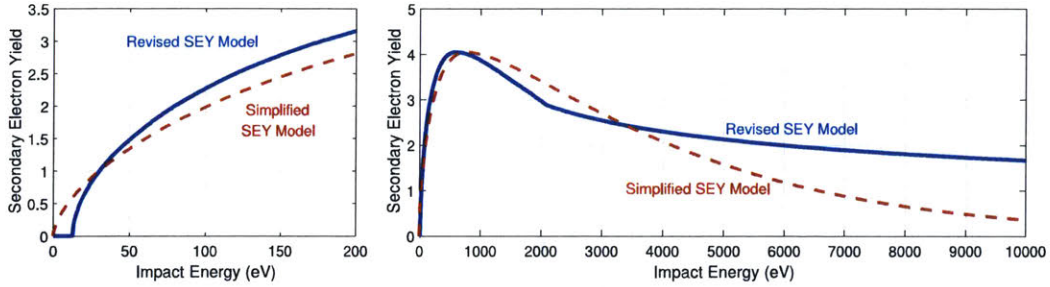

(a) Low Impact Energy (b) High Impact Energy

Figure 4-5: Example of how Vaughan's model of SEY [7] differs from the simplified model, Eq. 4.1 - Eq. 4.4. This example is calculated for fused quartz ($\delta_{max} = 2.9, V_{max} = 420$ eV), for impacts at grazing incidence, $\theta \approx 90°$.

ometries with tangential surface electric fields. The difference at low energies is less pronounced at normal incidence, though the large discrepancy in δ for high energy electrons remains.

Figure 4-6 shows the differences in a multipactor susceptibility plot calculated for fused quartz with a 110 GHz RF electric field tangential to the dielectric surface. These results still scale linearly with frequency, but they are displayed in terms of electric field strength to allow for easy comparison to the results in the following sections. Because the full Vaughan model significantly increases the calculated δ at high energies, the upper boundary of the multipactor susceptibility region is pushed to very high field values. The inclusion of a nonzero V_0 is a more subtle effect, as secondary electron production is dominated by impacts several times the nominal value of $V_0 = 12.5$ eV.

Figure 4-7 directly compares the boundaries of the multipactor susceptibility regions. The upper boundary of the region is pushed to very high electric fields, as the second crossover energy, V_2 is pushed to tens of thousands of eV. It is notable, however, that the effect on the lower boundary of the use of the full Vaughan model of SEY is only a slight perturbation to that derived using the simplified model of Kishek and Lau. This is important, because the lower boundary is the greater concern to the vast majority of applications in which dielectric multipactor may occur.

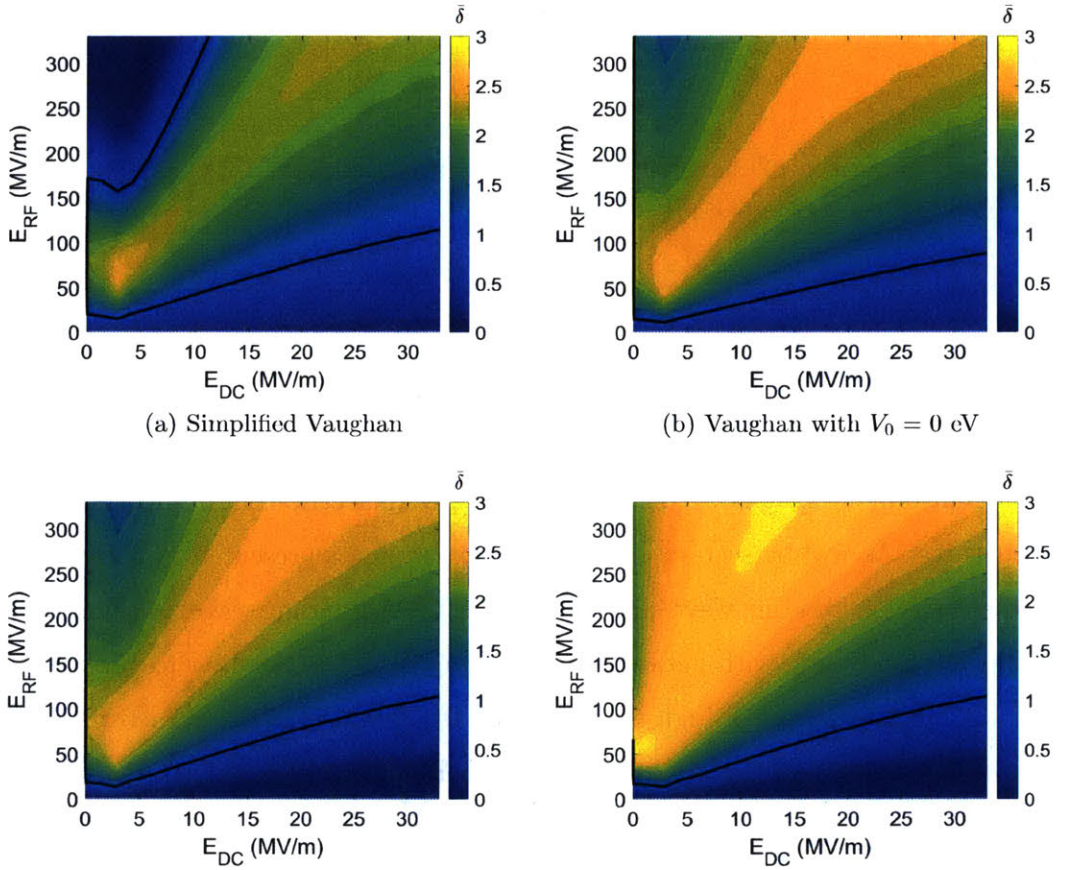

(a) Simplified Vaughan

(b) Vaughan with $V_0 = 0$ eV

(c) Vaughan with $V_0 = 12.5$ eV

(d) Vaughan with $V_0 = 12.5$ eV and RF Magnetic Field

Figure 4-6: Comparison of a multipactor susceptibility plot with the simplified Vaughan model of Kishek and Lau, and the revised model from section 3.1. The results in a)-c) scale linearly with frequency. This is only approximately true for d). d) is included here for a comparison of the effect of an RF magnetic field (see section 4.2.3). This example is calculated for fused quartz ($\delta_{max} = 2.9, V_{max} = 420$ eV) at 110 GHz.

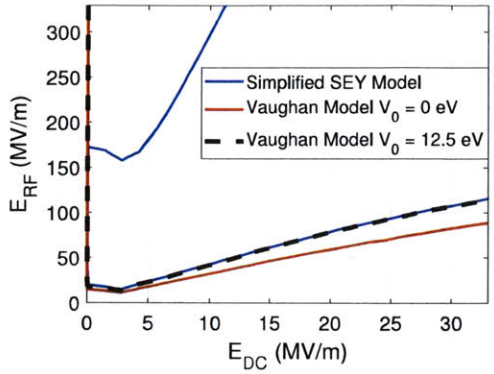

Figure 4-7: Comparison of the effects of using the non-simplified SEY model, and a nonzero value for V_0. This example is calculated for fused quartz ($\delta_{max} = 2.9, V_{max} = 420$ eV) at 110 GHz.

4.2.3 Effects of RF Magnetic Field

This section looks at the effects of the inclusion of an RF magnetic field on multipactor susceptibility. This is a consideration in any dielectric-containing traveling wave structures. As will be seen in chap. 5, the experiments presented in this thesis consisted entirely of standing wave structures. In a TEM standing wave, antinodes of the RF electric field align with nodes of the RF magnetic field, leading to very little RF magnetic field at points of high electric field. It is important to characterize the effect of an RF magnetic field, to know if the experiments performed on a standing wave structure have any applicability to a traveling wave structure.

The impact of an RF magnetic field on an RF window-like geometry, as in Fig. 4-1 was investigated in [79–81]. The orientation of the RF electric and magnetic fields was of an RF wave propagating into a dielectric surface ($\vec{k}$ pointing in the $-x$ direction in Fig. 4-1). This is applicable to an RF wave leaving a vacuum chamber through a dielectric window, a very common experimental reality. In this geometry, an electron that gains energy from the RF electric field will experience a force from the RF magnetic field in the $-x$ direction, pushing the electron back toward the surface. In the absence of an RF magnetic field, with a tangential RF electric field, the transit time of an electron trajectory is determined purely by its initial velocity in the x direction and the strength of the DC electric field, Eq. 4.7. Throughout the

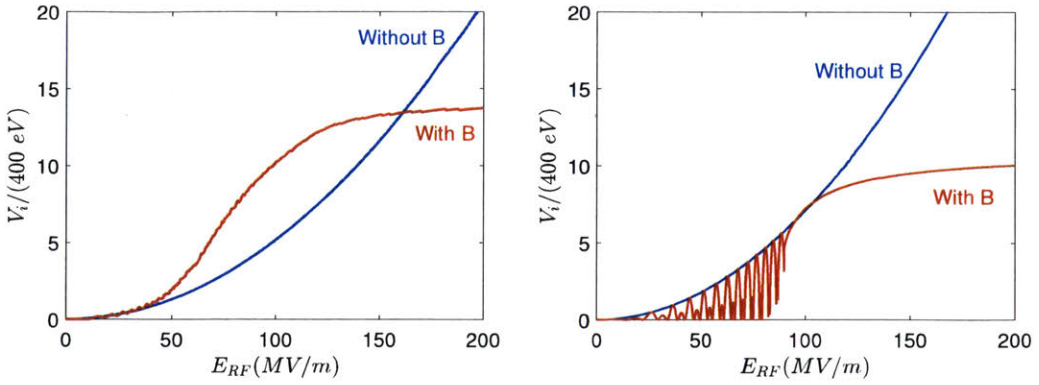

(a) Averaged over RF phase

(b) Example at RF phase: $\varphi = 75°$

Figure 4-8: Example of how an RF magnetic field limits the maximum impact energy of an electron. This is the impact energy of a 2 eV electron launched at a 75 degree angle with a DC field of 50 kV/m in the presence of a tangential RF electric field.

majority of the displayed multipactor susceptibility plots, the transit time is much shorter than an RF period. Thus, the further shortening of the transit time will, on average, lower the impact energy of electrons launched from the dielectric surface.

The effect of an RF magnetic field shortening the transit time of electron trajectories is displayed in Fig. 4-8. This shows example impact energy of a 2 eV electron launched from a dielectric surface at a 75° angle at various RF phases of a 110 GHz field. The most notable effect is that, at very high RF field strengths, the impact energy of the electrons saturates, rather than continuing to increase as E_{RF}^2. This, however, only begins to show a significant effect at electron energies that are high compared to the V_{max} of typical dielectric materials of interest for microwave sources and accelerators (400 - 1300 eV). It can be seen in Fig. 4-9a that, as far as the lower boundary of the multipactor susceptibility region, the magnetic RF field is only a slight perturbation.

The overall effect of the RF magnetic field on the multipactor susceptibility diagram for fused quartz is shown in Fig. 4-6d. At high energies, the RF magnetic field causes the contours of δ to spread, as the impact energy of electrons saturates. This effectively eliminates the upper bound of the multipactor susceptibility region for most values of DC electric field.

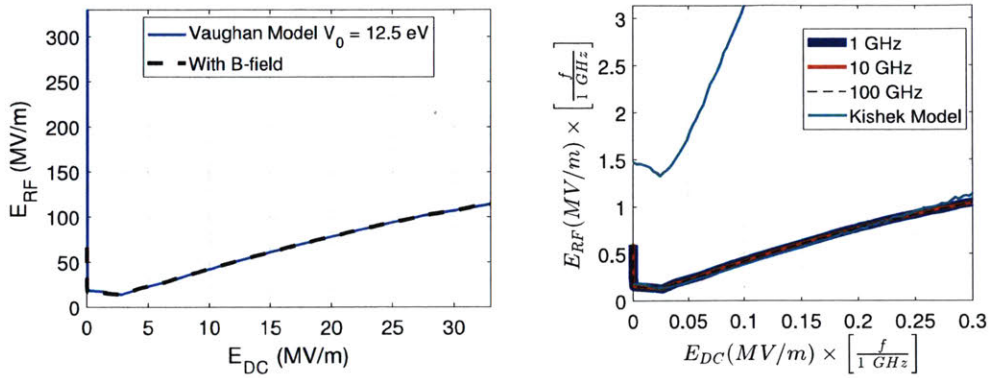

(a) Inclusion of RF B-field

(b) Frequency Independence

Figure 4-9: a) The effect of the inclusion of a tangential RF B-field causes a slight perturbation to the lower boundary of the susceptibility plot. It also eliminated the upper boundary, but, using the full Vaughan model of SEY, this was already at extremely high RF field values. b) The effect of the inclusion of a tangential RF B-field is linear with frequency. This example is calculated for fused quartz ($\delta_{max} = 2.9, V_{max} = 420$ eV) at 110 GHz.

Even with the inclusion of the RF magnetic field the boundaries of the multipactor susceptibility regions are linear with RF frequency. Though it is no longer easy to derive analytically, the multipactor susceptibility plots are found to still scale linearly with frequency. That is, the susceptibility plot in Fig. 4-6d, is reproduced at all frequencies, if the electric fields are divided by frequency. A comparison of the boundary of the multipactor susceptibility region for fused quartz is shown in Fig. 4-9b. The boundaries numerically calculated for 1, 10, and 100 GHz are indistinguishable. The "Kishek Model" line in this plot is produced using the simple Monte Carlo model from section 4.1. Possibly the most important prediction of the Kishek and Lau model, linear frequency scaling, is preserved.

It should be noted that, if the RF magnetic field were flipped so that it represented a wave leaving the dielectric surface, the RF magnetic field would have the opposite effect. At high electron energies, the RF magnetic field would provide a force away from the dielectric surface, raising electron impact energies, and vertically compressing the multipactor susceptibility region. This geometry would represent an RF wave entering a vacuum chamber through a window, perhaps a window separating two regions of vacuum. Still, this would only be a slight perturbation to the more

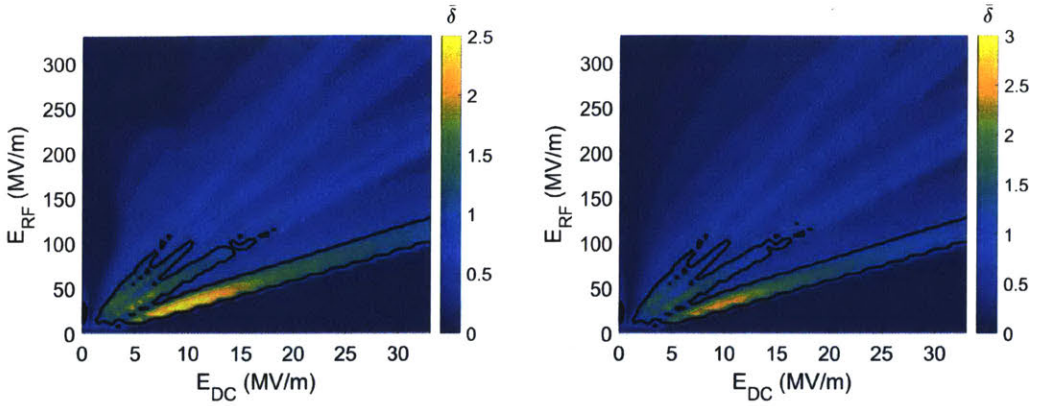

(a) No RF Magnetic Field

(b) Including RF Magnetic Field

Figure 4-10: Contour plot of the mean secondary electron yield for fused quartz with a normal surface RF electric field at 110 GHz.

important lower boundary of the multipactor susceptibility region.

4.3 Normal Electric Fields

The generalization of the Monte Carlo scheme in section 4.2.1 makes it easy to apply the same model to the case of normal RF electric fields. A multipactor susceptibility plot for fused quartz with a normal RF electric field ($\vec{E}_{RF} \parallel \vec{x}$) is shown in Fig. 4-10a.

Unlike in the case of a tangential electric field, the RF electric field now strongly impacts the electron transit time, as it acts in the x direction of Fig. 4-1. This allows for much longer transit times and more transfer of energy to the electron, vertically compressing the $\bar{\delta} = 1$ boundary of the multipactor susceptibility region. The finger-like structure to the susceptibility plot is the result of resonant electron trajectories. In the first "finger" that is enclosed by the multipactor susceptibility region, electrons are RF phase focused onto a trajectory with a transit time of 1 RF period. The next finger up consists of electrons phase focused onto a trajectory with a transit time of 2 RF periods, and so on.

With a normal electric field, the transit time of electrons is no longer dominated by a relatively weak (compared to the RF field) DC electric field. Additionally, the RF

magnetic field provides a force parallel to the dielectric surface, having little effect upon total energy or transit time. For these reasons, an RF magnetic field is less important than it is in the case of tangential RF electric fields. Figure 4-10b, shows a multipactor susceptibility plot with the inclusion of an RF magnetic field in the $-z$ direction, representing a wave traveling in the y direction. The RF magnetic field slightly alters the contours of the plot at very high RF field strength, but has little effect on the multipactor susceptibility region.

4.4 Steady State Multipactor and Power Absorption

From the multipactor susceptibility plots, we can predict the properties of a steady-state, or saturated, dielectric multipactor. If a dielectric surface is exposed to strong enough fields so that it falls within the multipactor susceptibility region, the average secondary electron yield of impacting electrons will be greater than one, $\bar{\delta} > 1$. In the presence of any seed electrons, a cloud of electrons will multiply above the surface. The removal of electrons from the dielectric surface will increase the strength of the DC electric field. To first order, the system will move to the right in the multipactor susceptibility plot, until it reaches a boundary of the susceptibility region. Due to absorption of power from the RF wave and deposition into the dielectric surface through impacts, the system will also progress down in the susceptibility region. As the strength of the RF electric field depends on the square root of the power of the RF wave, and the fraction of incident RF power absorbed is small, as will be shown, this is a much weaker effect [22].

The calculation of multipactor susceptibility regions allows for predictions of the fraction of incident RF power that is deposited onto the surface of the dielectric through collisions. The power deposited onto the dielectric surface is $P_{loss} = NV_i/\tau$. N is the number of electrons in the multipactor discharge, V_i is the impact energy, and τ is the transit time between impacts. Given the infinite planar geometry of the simulations, N can be estimated from E_{DC} as $N = 2\varepsilon_0 E_{DC} A/e$ where A is the area over which the discharge occurs. E_{DC} comes from the Monte Carlo simulations. For

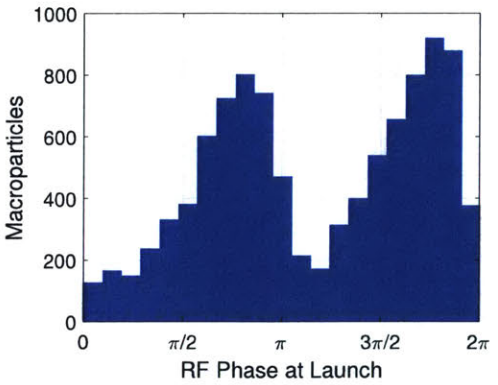

(a) Tangential E-field, RF phase of macroparticles

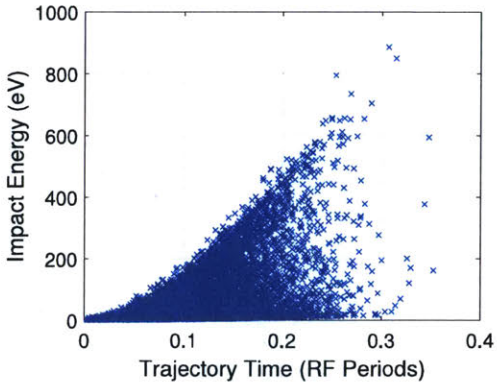

(b) Tangential E-field, transit time of macroparticles

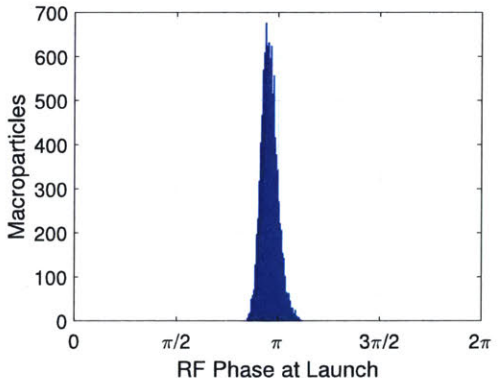

(c) Normal E-field, RF phase of macroparticles

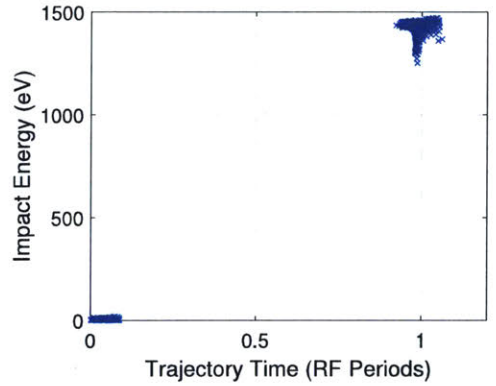

(d) Normal E-field, transit time of macroparticles

Figure 4-11: Comparison of the electron dynamics at saturation for a dielectric with tangential or normal surface electric fields. This example is calculated for fused quartz with a 42 MV/m RF electric field at 110 GHz. The DC electric field is 10 MV/m for a) and b), 15 MV/m for c) and d).

Material	RF E-field Orientation	C_1	E_{DC0} (MV/m)
Alumina (Lucalox)	tangential	0.544	-1.74
Sapphire	tangential	0.544	-1.74
Fused Quartz	tangential	0.281	-1.74
Crystal Quartz	tangential	0.244	-1.99
Alumina (Lucalox)	normal	0.332	1.87
Sapphire	normal	0.332	1.87
Fused Quartz	normal	0.3136	1.80
Crystal Quartz	normal	0.307	1.82

Table 4.1: Parameters for calculating E_{DC} at multipactor saturation from the input electric field, E_{RF}. These parameters were collected from Monte Carlo calculations. E_{DC} is calculated using equation 4.11.

every input value of E_{RF}, there is a corresponding value of E_{DC} at the right boundary of the multipactor susceptibility region. The right boundary of the multipactor susceptibility regions are, regardless of material or field orientation, very well described by a straight line. For a given value of E_{RF}, the value of DC electric field at the boundary edge can be found from Eq. 4.11, using the model parameters found in Table 4.1. C_1 is a unitless constant found from the numerical model.

$$E_{DC} = C_1 E_{RF} + E_{DC0} \tag{4.11}$$

The average impact energy and transit time at this boundary can also be had directly from the Monte Carlo simulations as a function of E_{RF}. Example trajectories of electrons at multipactor saturation are shown in Fig. 4-12. With tangential electric fields, the cloud of electrons will be confined near the dielectric surface to within about 1 ten thousandth of an RF wavelength. With normal RF electric fields, electron trajectories can range several hundredths of a wavelength away from the dielectric surface. These dimension will lead to difficulty resolving electron dynamics at saturation in a particle-in-cell (PIC) simulation of any realistic experimental geometry.

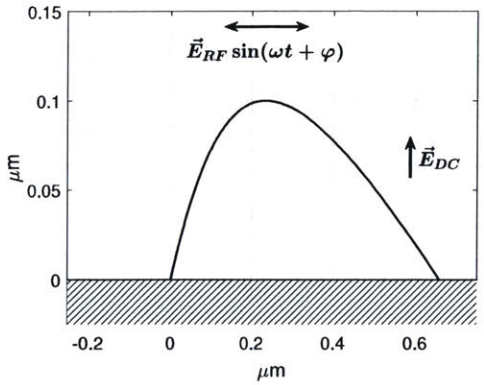

(a) 42 MV/m **tangential** RF field, 10 MV/m DC field

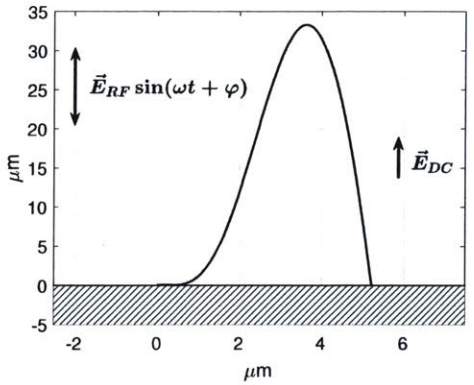

(b) 42 MV/m **normal** RF field, 15 MV/m DC field

Figure 4-12: Example trajectories of electrons launched at the boundary of a multipactor susceptibility region for fused quartz. Example electrons were launched with 2 eV and at an angle with the dielectric surface of $\phi = 45°$ at RF phase $\varphi = \pi$.

4.4.1 Tangential Electric Fields

An example of the electron dynamics at saturation with a tangential surface electric field is shown in Fig. 4-11a and b. With a tangential electric field, saturation occurs when the DC electric field has increased to the point that the average impact energy is approximately equal to the first crossover energy of the dielectric material, V_1. Impacts are spread throughout the RF phase. In the example simulation, at 42 MV/m RF electric field and 10 MV/m DC electric field, the average impact energy is 72.5 eV. The value of $V_1 = 30.5$ eV for fused quartz at a grazing angle. The actual average impact energy is a bit higher than V_1 to compensate for the shape of Vaughan's secondary electron model and the statistical spread in impact angles.

At the 10 MV/m DC electric field used in the example, the average impact time from the numerical simulation is 0.11 RF periods. As a comparison with analytical equations, the expected value of launch energy from Eq. 4.5 is $2V_{0m} \approx 0.01V_{max}$. This is 4.2 eV for fused quartz, giving an expected initial velocity of .004c, where c is the speed of light. Averaging over the launch angle distribution, Eq. 4.6, replaces the $\sin(\phi)$ in Eq. 4.7 with the value of pi/4. Plugging the boundary value of $E_{DC} = 10$ MV/m into Eq. 4.7 gives an expected value of transit time of 0.119 RF periods.

From the shape of the right boundary of the multipactor susceptibility region,

it can be see that, at saturation, E_{DC} is approximately $\propto E_{RF}$. This leads to the scalings with RF electric field shown in Eq. 4.12.

$$\begin{aligned} N &\propto E_{DC} \propto E_{RF} \\ V_i &\propto E_{RF}^0 \\ \tau &\propto E_{DC}^{-1} \propto E_{RF}^{-1} \\ P_{loss} &= \frac{NV_i}{\tau} \propto E_{RF}^2 \\ \frac{P_{loss}}{P_{RF}} &\propto E_{RF}^0 \end{aligned} \tag{4.12}$$

The expected fraction of the RF power absorbed by the multipactor is independent of the strength of the RF electric field, and subsequently also the RF power. This was first derived in [22], but never experimentally verified. The proportionality between E_{DC} and E_{RF} will depend upon the material used (Eq. 4.11 and Table 4.1). However, for a typical RF window of fused quartz, the loss of power will be on the order of 1%. This can result in a significant heat load, in the case of high power microwave devices.

4.4.2 Normal Electric Fields

With a normal surface electric field, the saturation mechanism is different than the relatively simple results with a tangential field. In the case of the normal field, after many impacts, electrons tend to be focused in RF phase about a single value. The dynamics of electron impacts at the right boundary of a multipactor susceptibility region on fused quartz is shown if Fig. 4-11c and d. In this example, at a 42 MV/m 110 GHz RF field and a 15 MV/m DC field, all electrons are launched about an RF phase slightly less than π. The electrons have a resonant transit of 1 RF cycle, as seen in Fig. 4-11d. Ignoring initial launch velocity, the impact energy of an electron launched precisely at RF phase π with a resonant trajectory is given by Eq. 4.13.

$$V_i = \frac{2}{m}\left(\frac{\pi e E_{DC}}{\omega}\right)^2 \tag{4.13}$$

For the example fields, this is 1635 eV, a value which yields a secondary electron yield of about 2 for fused quartz. This is compensated for by the random energy and angle spread of the launched electrons. About half of the electrons do not have enough energy to escape the pull of the DC electric field. They have very short trajectories, gain little energy, and have electron yields of zero. This leads to an average electron yield of one. At the right boundary of the multipactor susceptibility region, the fraction of electrons that gain nonnegligible energy from the RF fields can be estimated as 1 divided by the secondary electron yield at oblique incidence of electrons impacting with energy V_i, given by Eq. 4.13.

The shape of the right boundary of the multipactor susceptibility region with normal electric fields, as in the case with tangential fields, is a straight line. This approximately means, at saturation, $E_{DC} \propto E_{RF}$. This will again be used to determine the scaling of the power loss due to multipactor with surface electric field.

$$\begin{aligned} N &\propto E_{DC} \propto E_{RF} \\ V_i &\propto E_{DC}^2 \propto E_{RF}^2 \\ \tau &\propto E_{RF}^0 \\ P_{loss} &= \frac{NV_i}{\tau} \propto E_{RF}^3 \\ \frac{P_{loss}}{P_{RF}} &\propto E_{RF} \end{aligned} \tag{4.14}$$

With normal surface electric fields, it is predicted that the fraction of power lost to multipactor will increase approximately linearly with RF electric field. Two effects will complicate this simple scaling. As the fraction of power lost becomes large, the RF electric field at saturation will decrease from its initial value. As the impact energy of resonant orbits increases further and further beyond V_{max} for a particular dielectric, the fraction of launched electrons making the 1 RF period resonant trajectory will increase. These two effects work in opposite directions, and are fairly small for the range of existing experiments. With normal electric fields, the much higher average impact energy of electrons at saturation can lead to significant power absorption.

The linear scaling of power loss with RF electric field was initially proposed in [76] to explain results seen in an alumina loaded accelerating structure operating at 11.4 GHz. In this experiment, at the highest input powers, more than 50% of the incident power was absorbed by multipactor.

4.5 Multipactor Discharge Thresholds

The Monte Carlo simulations presented thus far do not yield accurate predictions of threshold RF electric fields for the initiation of multipactor. It can be seen from the solid lines in Fig. 4.1 that the predictions of these models are not typically extended down to 0 DC electric field. At this limit, in the model of Kishek and Lau, electron trajectories tend toward infinite size and time, due to the lack of any restoring force returning electrons to the surface. Naively extending the lower boundary of multipactor susceptibility regions to zero DC electric field will yield a prediction for the threshold electric field that is within about a factor of 5 of experimentally found values. The following simple calculation will yield a closer prediction.

For dielectric multipactor to occur, the dielectric must become charged in the presence of an RF field. This can be done by impacts from stray electrons with trajectories that take them through a region of strong field before impacting the dielectric. Neglecting the small initial velocity seed electrons may have, an electron in an RF electric field will have the kinetic energy given by Eq. 4.15.

$$V = \frac{1}{2m}\left[\frac{eE_{RF}}{\omega}\cos(\omega t + \varphi)\right]^2 \tag{4.15}$$

$$E_{RF} \approx \frac{\omega}{e}\sqrt{4mV_1} \tag{4.16}$$

To lowest order, this kinetic energy can be simply averaged over RF phase and set equal to V_1 of a particular dielectric material from Table 3.1, yielding Eq. 4.16. This represents the average impacting energy of stray electrons that strike the surface. Until the surface is sufficiently charged, the electrons liberated by this impact will escape the system, but leave a slight positive charge on the dielectric. If the

Material	Tangential E Threshold $\left[\frac{kV}{m}\left(\frac{f}{1GHz}\right)^{-1}\right]$	Tangential E at 110 GHz $\left[\frac{MV}{m}\right]$	Normal E Threshold $\left[\frac{kV}{m}\left(\frac{f}{1GHz}\right)^{-1}\right]$	Normal E at 110 GHz $\left[\frac{MV}{m}\right]$
Alumina (Lucalox)	141	15.5	154	16.9
Sapphire	141	15.5	154	16.9
Fused Quartz	196	21.6	220	24.2
Crystal Quartz	220	24.2	252	27.7
Silicon	400	44.0		

Table 4.2: Table of predicted threshold RF electric fields for the onset of multipactor discharge.

average impact energy is greater than V_1, the dielectric will continue to charge until multipactor is initiated.

For greater accuracy, the average secondary electron yield can be calculated as a function of RF phase, by feeding Eq. 4.15 into Vaughan's model of SEY. These values are then averaged over RF phase. Values were averaged using a modified geometric mean, as in Eq. 4.10. The resulting predicted multipactor threshold values are displayed in Table 4.2. The values for tangential electric fields are calculated assuming a grazing impact ($\theta = \pi/2$), and the values for normal electric fields are calculated assuming an oblique impact ($\theta = 0$). For secondary electron yield parameters of these materials, see Table 3.1. The values in Table 4.2 were calculated using Vaughan's model with a value of $V_0 = 12.5$ eV. These values are about 20% higher than the values calculated using Eq. 4.16.

It should be noted that Eq. 4.16 is similar to a relationship suggested in [75]. In |75|, it is stated that, for multipactor to occur, the electron oscillation energy in the external microwave field, $\varepsilon_{osc} = (eE_{RF}/\omega)^2/2m_e$ is greater than or equal to the first crossover energy, V_1. This predicts threshold a factor of $\sqrt{2}$ lower than Eq. 4.16, because it does not average the oscillation energy over RF phase. Additionally, accounting for the shape of the SEY curve for a particular material will further raise the multipactor threshold RF electric field by about 20%, generating the values in Table 4.2.

The simple method for calculated a multipactor threshold RF electric field presented in this section, assuming infinite, homogeneous RF electric fields will tend to under predict breakdown thresholds, especially if the fields decay rapidly with distance from the dielectric surface. This formula yields a safe lower bound below which multipactor should not occur in the vast majority of experimental geometries. A more detailed calculation including the spatial profile of fields would have to be carried out for a specific experiment or device if a more precise multipactor threshold must be predicted. An effort for greater accuracy, however, will be hampered by the limited experimental data on the secondary electron yield properties of dielectric materials. Much of the original data in Table 3.1 and [44] dates to the 1930's, before high vacuum technology had matured.

4.6 Conclusions of Theoretical Modeling of Dielectric Multipactor

From this look at the theory of multipactor discharge, we draw the following useful predictions. The strength of the electric fields necessary for the initiation of multipactor scale linearly with frequency. This allows one to extrapolate from existing experimental data, as new higher frequency, higher power microwave sources and devices are developed. In lieu of extrapolation from lower frequency experiments, Eq. 4.16 can provide a lower bound to the breakdown threshold for any frequency and material.

Monte Carlo simulations provide quantitative predictions of power deposition on a dielectric due to multipactor. For a given material and input RF electric field, a DC electric field at saturation can be calculated from Eq. 4.11 or pulled from the lower boundary of a multipactor susceptibility plot such as Fig. 4-3. Combined with the area of a high-field region and the specific scaling of RF power and RF electric field for a particular experiment, this yields a prediction of power deposition. When designing a device in which multipactor cannot be avoided, this gives the heat loads

that will have to be accounted for in the design.

The Monte Carlo simulations also give an indication of the possibility of "burn through." This is a strategy where the electric field in a device is rapidly ramped through the multipactor susceptibility region, to high enough RF electric fields that multipactor does not occur. This possibility depends on the specific geometry of the device being designed. For a microwave beam exiting a vacuum chamber through a window (a tangential RF electric field), the RF magnetic field can completely eliminate this possibility, especially for materials with higher secondary electron yield than fused quartz. Conversely, the multipactor susceptibility region is fairly small for geometries with normal RF electric fields, such as some dielectric lined waveguides, and burn through may be a productive strategy.

Finally, the discussion in section 4.5, and specifically Eq. 4.16, provides a means to quickly estimate a multipactor discharge threshold. The method is very simplistic, and will tend to under predict the threshold RF electric field. It will be shown in chapter 6, however, that this calculation fits existing and new experimental data to within a factor of 2, regardless of specific experiment geometry.

Chapter 5

Design of Experiments for the Study of Dielectric Multipactor at 110 GHz

5.1 Test Stand

MIT's 1.5 MW gyrotron, described in chapter 2, was configured to operate as a 110 GHz high power microwave source for the study of dielectric multipactor. For these studies, to aid in accurate alignment and control of the input microwaves, the gyrotron was used with an internal mode converter, described in section 2.6, that allowed the output to be coupled directly into a 31.75 mm diameter corrugated waveguide. A length of corrugated waveguide transported the high power microwaves to an optical table where a test stand was constructed. The output of the corrugated waveguide provided an excellent alignment surface where the location, size, and phase front of the Gaussian beam of high power microwaves was well known.

The test stand assembled for this study is shown in Fig. 5-1. At the output of a corrugated waveguide sat a zeroth order sapphire half-wave plate. This is a 3.997 mm thick disk of sapphire cut such that its optical axis is parallel to flat surfaces of the disk (an A-Plane cut). Using the refractive indices in Table 5.1, this sapphire disk was 4.5 wavelengths thick for microwaves polarized along the slow optical axis (extraordinary polarization) and 4.0 wavelengths along the fast axis (ordinary polarization). This choice of thickness simultaneously provided half-wavelength retardation along the

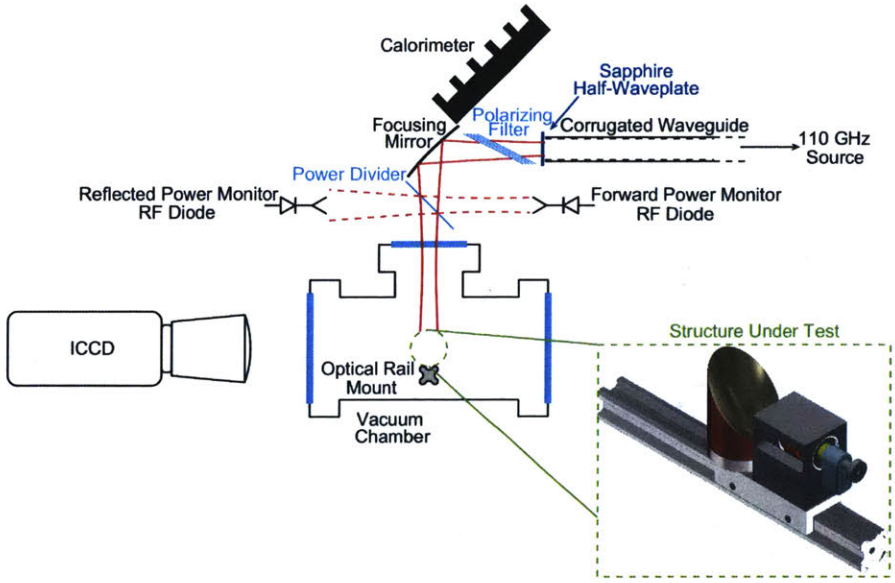

Figure 5-1: Schematic of the test stand used in the study of dielectric multipactor at 110 GHz. Microwaves are brought from the gyrotron source (off right of figure) to the test stand in a corrugated waveguide. A half-waveplate rotates the polarization of the linearly polarized microwaves, and a polarizing filter attenuates vertically polarized microwave power. This setup serves as a variable attenuator, varied by rotation of the half-waveplate. A focusing mirror brings the free-space microwave beam into a vacuum chamber in which the test structure is mounted.

slow axis, forming a half-waveplate, and was a multiple of half-wavelength thickness on both axes, forming a reflectionless window.

Directly from the gyrotron source, microwaves were polarized vertically (out of the page in the figure). The half-wave plate was used to rotate the polarization to an arbitrary angle. Following the polarization rotation, the beam passed through five fused quartz plates tilted at Brewster's angle with respect to the propagation axis of the beam. Combined with the sapphire half-wave plate, this setup formed a continuously variable attenuator with sufficient power handling capability for the pulsed megawatt microwave beam. Horizontally polarized microwaves passed through the five quartz plates to the experiment, while vertically polarized microwaves were scattered toward a calorimeter. This calorimeter was used to continuously monitor the output power of the gyrotron.

After the polarizing filter, an off axis parabolic mirror refocused the microwave

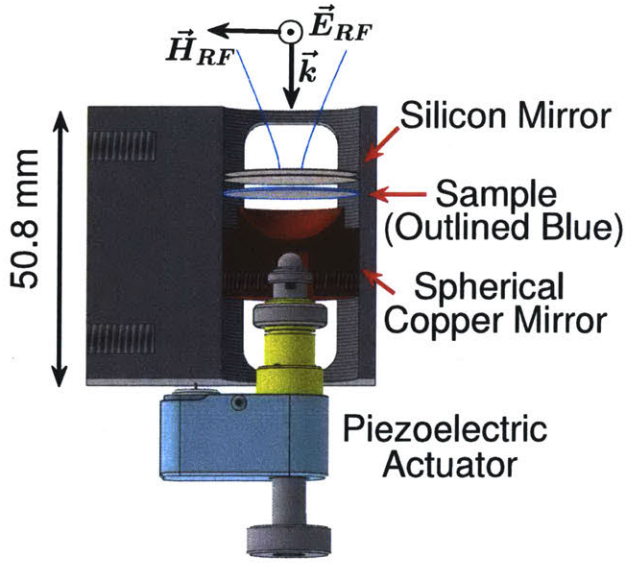

Figure 5-2: Fabry-Perot cavity constructed to study dielectric multipactor with tangential electric fields. Spacers and retaining rings are omitted for clarity.

beam and directed it toward the window of a vacuum chamber. Between the parabolic mirror and the vacuum chamber, a quartz plate at a 45 degree angle picked off about 1% of the beam. This picked off signal was monitored with RF diodes to measure forward power into the experiment and power reflected from the experiment. Inside the vacuum chamber were mounting points for an optical rail. Test structures, such as the one shown in the inset of Fig. 5-1, were assembled on an optical rail prior to insertion into the vacuum chamber. The vacuum chamber itself was mounted on a 2-axis translation stage and a lab jack, allowing for 3-axis alignment of the test structure with the microwave beam. Vacuum in the chamber was achieved with a 60 L/s ion pump, yielding a base pressure of less than 1×10^{-8} Torr. The vacuum chamber hosted five 8 inch vacuum ports, as well as two 2.75 inch and two 1.33 inch vacuum ports, allowing a multitude of feedthroughs that were used for diagnostics and motor control. Windows on the 8 inch vacuum ports allowed for the use of non-perturbing visible light diagnostics.

5.2 Design of Test Structures

Two separate test structures were designed to independently study dielectric multipactor with either tangential or normal surface electric fields. The structures were designed to generate surface electric fields on the samples in excess of 100 MV/m using 1 MW of input power. Structures were designed to be largely open, to allow the use of visual diagnostics as well as to allow the vacuum environment to quickly recover after a breakdown, where gas could be released near the surface under test.

Care was taken to design structures with fields below 1 kV/m at any triple points. A triple point is an interface where vacuum, dielectric material, and a conducting material all meet. Such points have very low breakdown thresholds, as the discontinuity in materials can cause great enhancement of the local electric field.

Pains were taken to generate designs that were insensitive to dimensional variations up to at least 25 micrometers. This is an easily achievable tolerance with the direct machining techniques that were relied upon to construct these experiments. This dimensional insensitivity was necessary so that the fields in the structures could be well known.

Fields in the test structures were calculated using Ansys Electronics Desktop [86], formerly Ansys High-Frequency Structure Simulator (HFSS). This is a finite element method solver for electromagnetic structures. Realistic refractive indices and loss tangents for dielectric materials were taken from [87–90]. The loss tangent is the ratio of the imaginary part of a material's permittivity to the real part. The values are in Table 5.1. The range of loss tangents for some materials in the table did not strongly affect the calculated field strengths. Dielectric loss in the test structures was very small compared to ohmic and diffractive (scattering) loss.

5.2.1 Fabry-Perot Test Structure for Tangential Electric Fields

For study of dielectric multipactor with tangential surface electric fields, an open optical cavity, or Fabry-Perot resonator was constructed. Shown, in Fig. 5-2, this is a one port optical cavity. The Gaussian beam of incident microwaves was focused to a

Material	Refractive Index	Loss Tangent ($\times 10^{-4}$)	Source
Alumina (Al_2O_3)	3.244	2.7	[87–89]
Sapphire (Ordinary)	3.066	2.1-2.5	[87, 88]
Sapphire (Extraordinary)	3.400	1.1-1.4	[87, 88]
Fused Quartz	1.953	5.5 - 7.1	[87–89]
Crystal Quartz (Ordinary)	2.108	0.9	[87–90]
Silicon	3.424	0.24	[87, 88]

Table 5.1: Table of refractive indices and loss tangents at 110 GHz of dielectric materials tested. The range of loss tangents come from measurements of multiple samples from multiple sources.

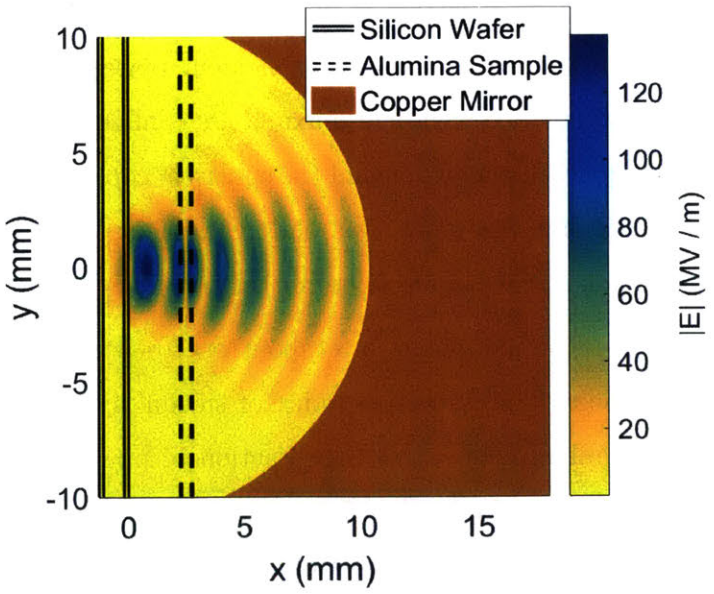

Figure 5-3: Electric fields excited in the Fabry-Perot cavity with an example alumina sample placed at the second field maximum.

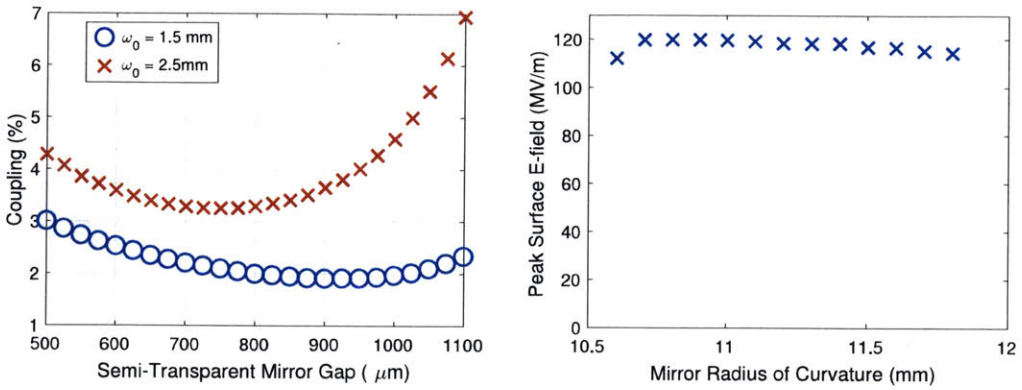

(a) (b)

Figure 5-4: Examining the tolerances required in construction of mirrors for the Fabry-Perot cavity. (a), the coupling into the cavity is insensitive to the changes in the spacing of the wafers of the silicon mirror of less than 50 micrometers. (b), the electric field on the sample is highly insensitive to the precise curvature of the spherical copper mirror.

beam waist on to a semi transparent mirror, consisting of two silicon wafers separated by a vacuum space. A spherical copper mirror, curved to match the phase front of the Gaussian beam, formed the other end of the cavity. The fields in the structure are shown in Fig. 5-3. In this figure, 1 MW of incident power is incident on the silicon wafer at the left edge plot. Seven field maxima are confined within the cavity, between the semi transparent silicon wafers and the spherical copper mirror. The test sample, in this example an alumina wafer, was placed on the second field maximum within the cavity, with peak surface fields of more than 120 MV/m.

The silicon wafers, at 185 micrometers, are about one quarter wavelength thick (λ = 2.72 mm in free space. The refractive index of silicon is 3.424 at 110 GHz). Between them was a 900 micrometer gap. The fraction of power coupled through this semitransparent mirror is shown in Fig. 5-4a, calculated for two different values of microwave beam waist. In the experiment, and in all of the calculations shown, a 2.5 mm beam waist was used, as this generated sufficiently strong fields to allow the development of multipactor.

This geometry of a planar mirror and a spherical mirror was chosen to eliminate sensitivity to tilts between the two components. As long as the spherical mirror is

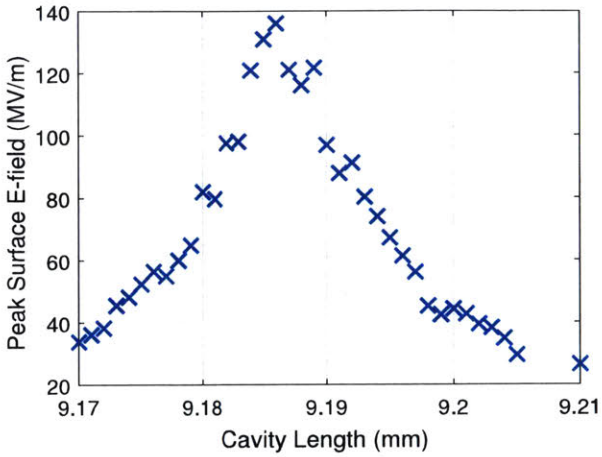

Figure 5-5: The critical tolerance of the Fabry-Perot cavity: the electric field on the sample is sensitive to 1 micrometer shifts in the overall length of the cavity.

not tilted enough to allow microwaves to spill past its edge, any tilt still results in a spherical surface facing a planar surface. Shown in Fig. 5-4b is the dependence of the strength of the surface electric field on an alumina sample as a function of the curvature of the copper mirror. Nominally curved with an 11.1 mm radius, the fields in the structure were insensitive to inaccuracies of hundreds of micrometers.

One dimension of the tangential field test structure could not be made insensitive to machining tolerances. Shown in Fig. 5-5, the resonant frequency, and thus the field on the sample was, sensitive to variations in the cavity length of about 1 micrometer. This was a tighter tolerance requirement than could be reliably achieved through direct machining. To combat this, the copper mirror was mounted on a vacuum-compatible piezoelectric actuator with a step size of less than 30 nm. As seen in Fig. 5-2, the entire cavity was mounted in a single stainless steel threaded tube to provide rigidity, disallowing vibration between the components.

5.2.2 Low Power Tests of Tangential Electric Field Structure

To verify that the piezoelectric actuator was capable of tuning the length of the cavity sufficiently accurately, and that the fields in the structure were accurately modeled, low power, high precision measurements of the structure were made. A vector network analyzer was used to sweep the frequency of an input microwave beam and measure

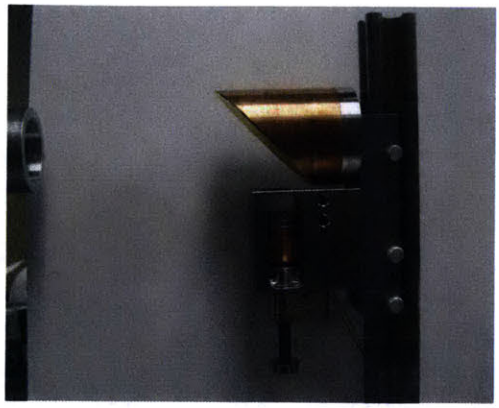

Figure 5-6: Image of the Fabry-Perot (tangential electric field) structure on low power test stand for precision measurements of cavity resonance and tunability. The piezoelectric actuator (seen at the bottom of the test structure) allowed the cavity resonant frequency to be tuned.

the reflected signal from the cavity. A photograph of the structure mounted for low power testing is shown in Fig. 5-6. The results of this low power measurement are shown in Fig. 5-7. S_{11} is the relative amplitude of the reflected signal, proportional to the square root of the power of the reflected signal. The structure was disassembled and reassembled each time the sample material was changed. Each time, the resonant frequency of the cavity was tuned to 110.080 GHz to within 1 MHz. The resonant frequency of the cavity is linearly proportional to the length of the cavity. The cavity frequency could be tuned with an accuracy of at least 1 part in 10^5. This corresponds to an accuracy of about 0.1 micrometers in cavity length, well within the 1 micrometer tolerance needed to accurately know the fields in the cavity.

Figure 5-8 shows two examples of the frequency response of the structure compared to that of the Ansys model of the structure. There is good agreement between the bandwidth of the structure and the model. This means that the total losses within the cavity and the semi transparent coupling mirror have been accurately modeled.

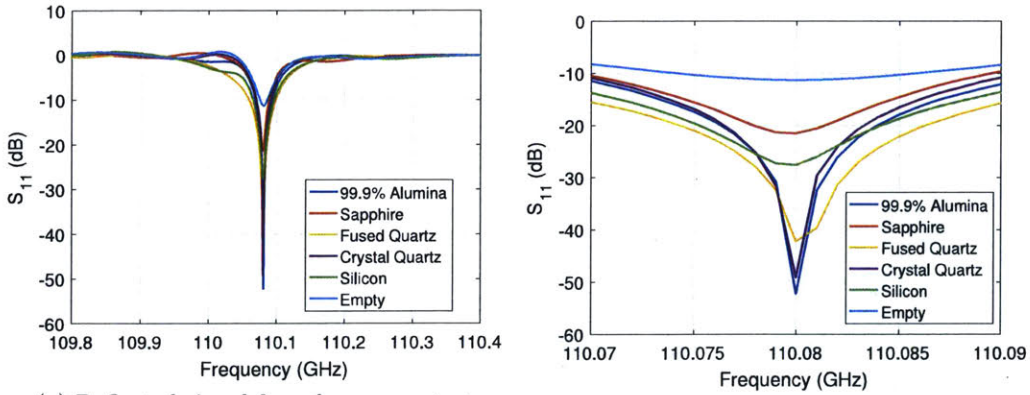

(a) Reflected signal from low power test

(b) Zoom in on resonances

Figure 5-7: Results of the lower power testing of the tangential electric field structure. The piezoelectric actuator allowed the cavity resonant frequency to be reproducibly tuned to 110.080 GHz to within 1 MHz precision. The cavity was disassembled and reassembled each time the sample material was changed. S_{11}, plotted on a logarithmic scale, is the amplitude of the reflected signal measured in a lower power test.

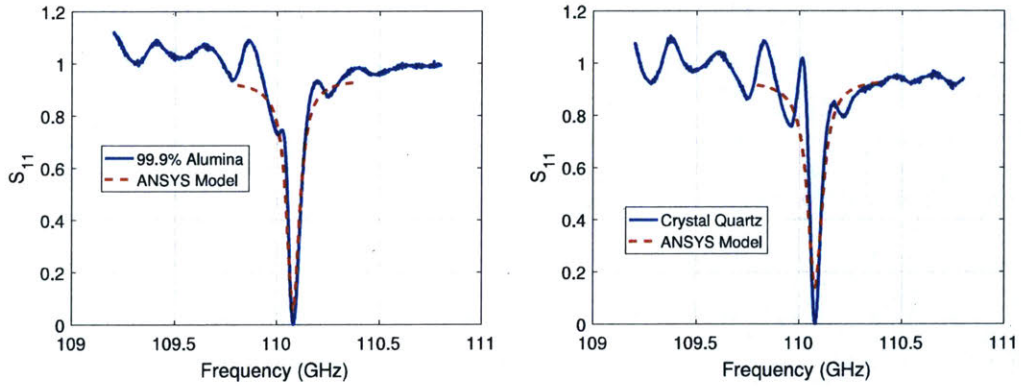

(a) Cavity with Alumina Sample

(b) Cavity with Crystal Quartz Sample

Figure 5-8: Comparison of the frequency response of the constructed Fabry-Perot cavity with the modeled cavity. S_{11}, plotted in b), is the amplitude of the reflected signal measured in a lower power test.

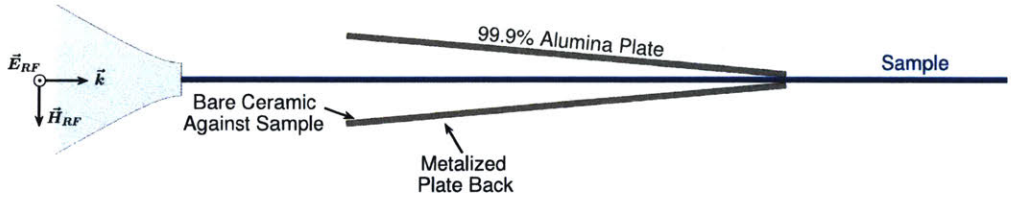

Figure 5-9: For studying multipactor with normal surface electric fields, a high power Gaussian microwave beam is coupled to a sub-wavelength dielectric rod that serves as both waveguide and sample. The fields of the excited mode are enhanced with a taper of partially metalized alumina plates.

5.2.3 Dielectric Rod Waveguide Structure for Normal Electric fields

To study dielectric multipactor with normal surface electric fields, a more unusual structure was constructed that avoided the use of a resonant cavity. This removed tight tolerances on all dimensions. The geometry of the test structure is shown in Figs. 5-9 and 5-10. The incoming microwave beam was focused to a 1.5 mm beam waist (0.55λ) on the end of a sub-wavelength (0.5 - 0.8 mm diameter) dielectric rod. In this structure, the dielectric rod acted as both a waveguide and the sample under test.

The mode excited on the dielectric rod waveguide is a distortion of the HE_{11} mode of circular dielectric waveguides. Unfortunately, this is very different from the HE_{11} mode of corrugated waveguide discussed in chapter 2. The typical HE_{11} mode of a circular dielectric waveguide, defined analytically in [91–94], is shown in Figs. 5-11 and 5-12. The mode is similar to a Gaussian beam in cross section, concentrated in the center of the dielectric rod. Seen in Fig. 5-11, field lines form loops along the rod. This mode can be readily excited by simply illuminating the end of a dielectric rod with a Gaussian beam [95, 96]. The analytical definition of the HE_{11} mode, including electric and magnetic fields in three dimensions, both inside and outside the dielectric waveguide, is rather lengthy, and therefore omitted from this writing. The equations

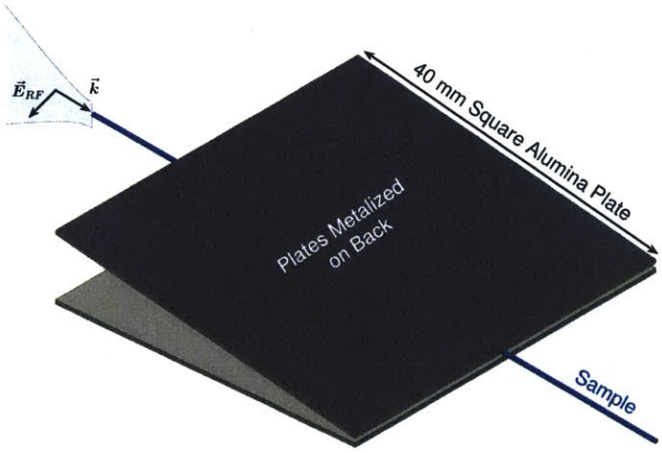

Figure 5-10: A second view of the dielectric rod waveguide structure used to study dielectric multipactor with normal surface electric fields.

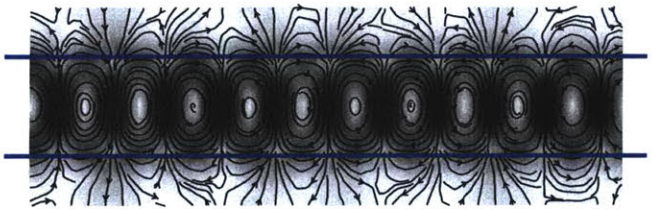

Figure 5-11: Electric fields along a solid dielectric rod waveguide that is excited by a standard HE_{11} mode. Dark regions indicate stronger electric fields. Blue lines show the boundary of the dielectric rod. This example was calculated for a 1 mm diameter sapphire rod (optical axis along the rod) excited by a 110 GHz ($\lambda = 2.72$ mm) field.

are gathered most concisely in [91], if the reader is interested in further detail.

By using a rod that is very small in cross section compared to a free-space wavelength, the mode is usefully distorted. Shown in Figs. 5-13 and 5-14, the test structure makes use of a dielectric rod that is barely large enough to support a single mode. The mode still has field lines forming loops along the rod, and the magnetic field is still well confined in the interior of the dielectric rod. However, the electric field of this distorted HE_{11} mode is strongly concentrated on the sides of the surface of the rod. Importantly, where the electric field peaks along the rod, it is also largely perpendicular to the rod's surface. Maximizing the electric field on the surface of the rods for a given input power was achieved with a rod diameter of $\lambda/(1.75n)$, where n

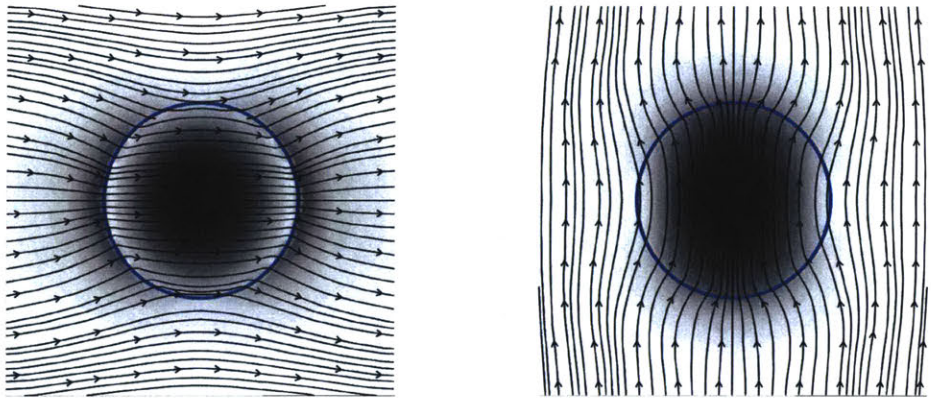

(a) Electric Field (b) Magnetic Field

Figure 5-12: Electric and Magnetic fields of a standard HE_{11} mode of a solid dielectric rod as viewed from a cross section of the rod. This example mode was excited by a horizontally polarized incident Gaussian beam. Dark regions indicate stronger fields. Blue lines show the boundary of the dielectric rod.

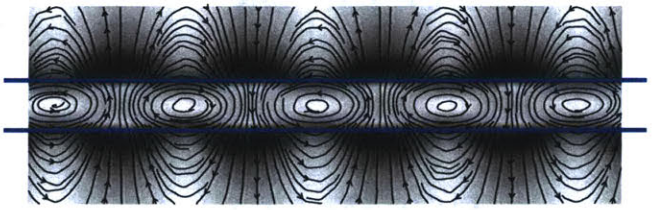

Figure 5-13: Electric fields along a solid dielectric rod waveguide that is excited by an HE_{11}-like mode. Here, the rod is too small in diameter compared to the wavelength of the incoming waves to support the standard HE_{11} mode. The mode is distorted, and the electric field is strongly concentrated on the surface of the rod. Dark regions indicate stronger electric fields. Blue lines show the boundary of the dielectric rod. This example was calculated for a 0.5 mm diameter sapphire rod (optical axis along the rod) excited by a 110 GHz ($\lambda = 2.72$ mm) field.

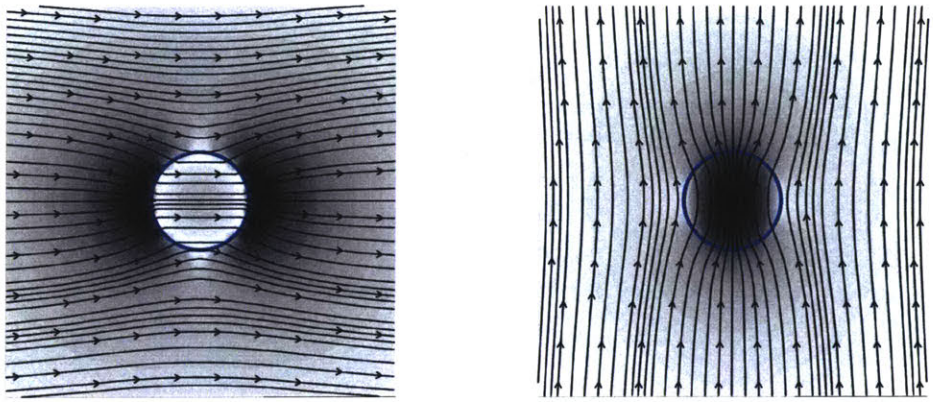

(a) Electric Field (b) Magnetic Field

Figure 5-14: Electric and Magnetic fields of an HE_{11}-like mode of a solid dielectric rod as viewed from a cross section of the rod. In this example, the rod is nearly too small in diameter to confine the microwaves, and the electric field of the distorted mode is strongly concentrated on the surface of the rod. Dark regions indicate stronger fields. Blue lines show the boundary of the dielectric rod.

is the refractive index of the rod. This is about 0.5 mm diameter for either sapphire or alumina, and 0.8 mm for fused quartz. These small diameter rods support only a single confined mode. Some of the power (about 10% in experiment) from the incident Gaussian beam does not couple to this confined mode. It excites other modes of the dielectric rod, but these higher order modes radiate away from within a few mm's of propagation along the rod.

To provide further field enhancement, alumina plates were placed at an angle above and below the dielectric rod sample. Tilted at a 5 degree angle, these plates interacted with the magnetic field of the mode. The plates are far from the sides of the rod where the electric field is concentrated. The backs of the alumina plates were metalized with silver. The sides of the alumina plates against the dielectric rod were bare alumina, avoiding the creation of a triple point.

The fields generated in the structure are shown in Figs. 5-15 and 5-16. In the figures, a 1 MW microwave beam is focused to a 1.5 mm spot size on the left end of an example 0.5 mm diameter alumina rod. Because the backs of the alumina plates

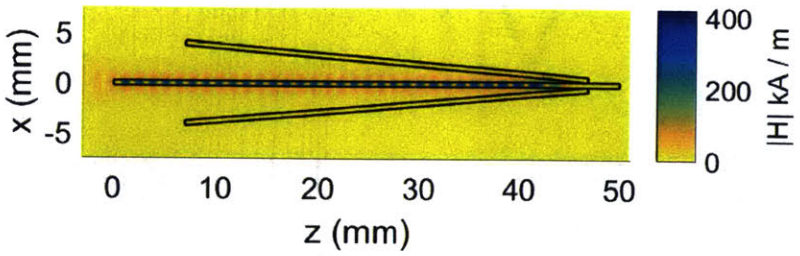

(a) Electric Field

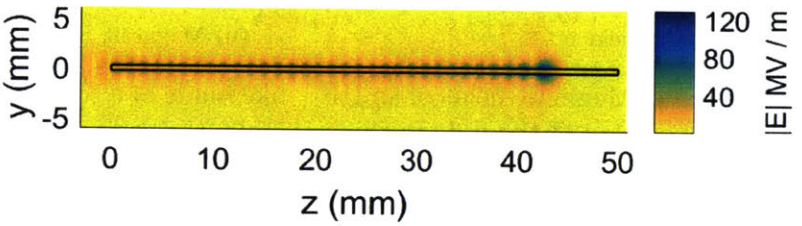

(b) Magnetic Field

Figure 5-15: Magnitudes of the magnetic and electric fields excited in the dielectric rod test structure. Note that the bottom view is rotated by 90 degrees about the dielectric rod, compared to the top view. These are the fields generated by a 1 MW Gaussian beam focused (1.5 mm beam waist) on the left end of the 0.5 mm diameter alumina rod.

are metalized, they cutoff the propagating waveguide mode near the right side of the taper. The mode is reflected back, setting up a standing wave along the rod and yielding a factor of 2 increase in the peak electric field along the surface of the dielectric rod. The sides of the rod, where the electric field is concentrated remain visible between the alumina plates, allowing for visual observation of multipactor. As the mode is cut off at the right side of the taper, no microwaves propagated beyond the end of the alumina plates to interact with triple points created by the metalized backing of the plates or the structure supporting the rod and plates.

Ceramic plates metalized on the back were used to create the taper, because the softer interaction between the waveguide mode and the ceramic plate was found to greatly reduce dimensional tolerance requirements, as opposed to using an all

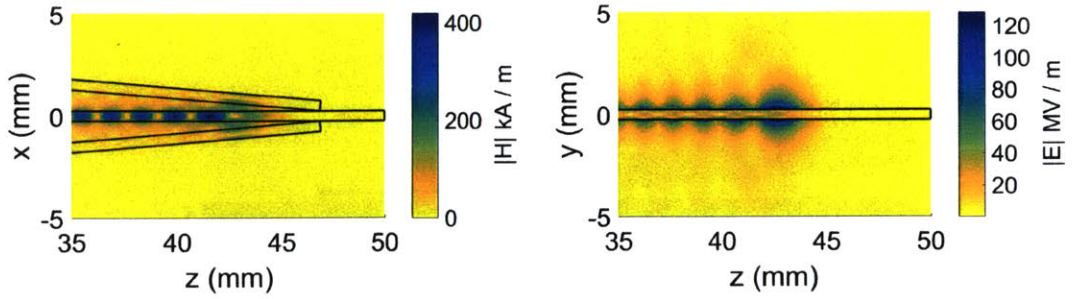

(a) Electric Field

(b) Magnetic Field

Figure 5-16: A closer look at the peak magnetic and electric field magnitudes excited in the dielectric rod structure. These are zoomed in views of the fields displayed in Fig. 5-15. The maximum magnetic field is 418 kA/m, and the maximum surface electric field is 128.5 MV/m with 1 MW of power incident on the 0.5 mm diameter alumina rod.

metal taper. Figure 5-17 defines the dimensions that are examined in the following figures for sensitivity to machining tolerances. Figure 5-18 shows the variation of peak electric field on the sample versus the thickness of the alumina plates and an offset between the plates. The thickness of the alumina plates was nominally 0.5 mm (easily measured with 5 micrometer resolution), and could vary by 25 micrometers with no significant change in the fields on the sample. An offset between the plates of 100's of micrometers had virtually no effect on the peak fields achieved on the sample. The shallow taper angle of 5 degrees meant that an offset in the position of the alumina plates had very little relative effect on the geometry of the region where the mode of the dielectric rod waveguide was cutoff by the taper.

Figure 5-19 shows the variation of peak electric field on the sample versus the angle of the plates, and the diameter of the sample dielectric rod. The structure was insensitive to changes in the taper angle by $\pm$ 2 degrees. The diameter of the dielectric rod had to be kept within a 50 micrometer range. If too small, the rod would not confine a mode at all. If too large, the rod would confine a standard HE_{11} mode and the electric field would be concentrated in the interior of the sample, rather than on its surface. This is an achievable tolerance, however. Additionally, this is an

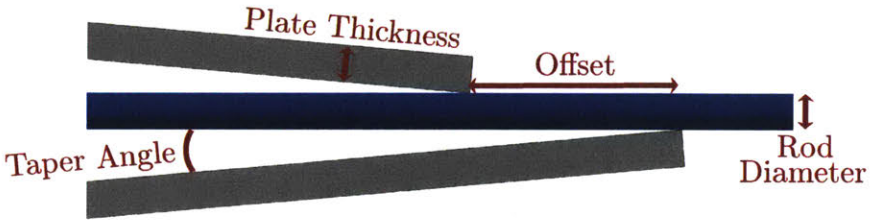

Figure 5-17: Definition of dimensions that are examined for tolerance sensitivity in Figs. 5-18 and 5-19.

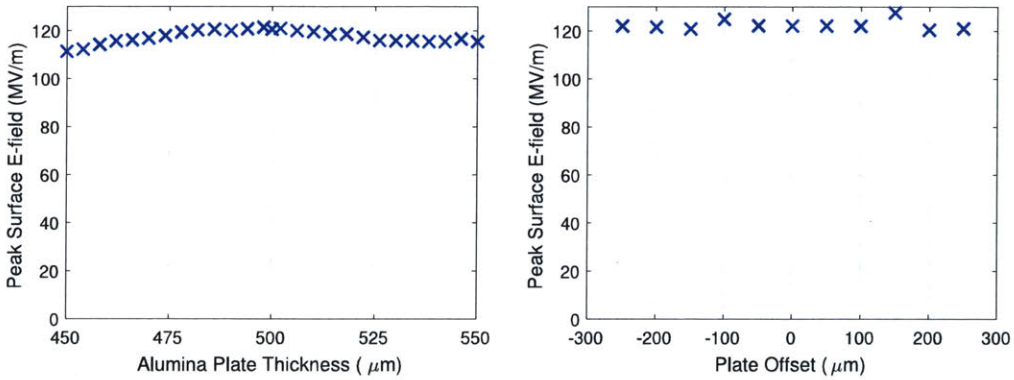

Figure 5-18: The surface electric fields in the dielectric rod structure show weak dependence on the precise thickness an positioning of the alumina plates that form a taper.

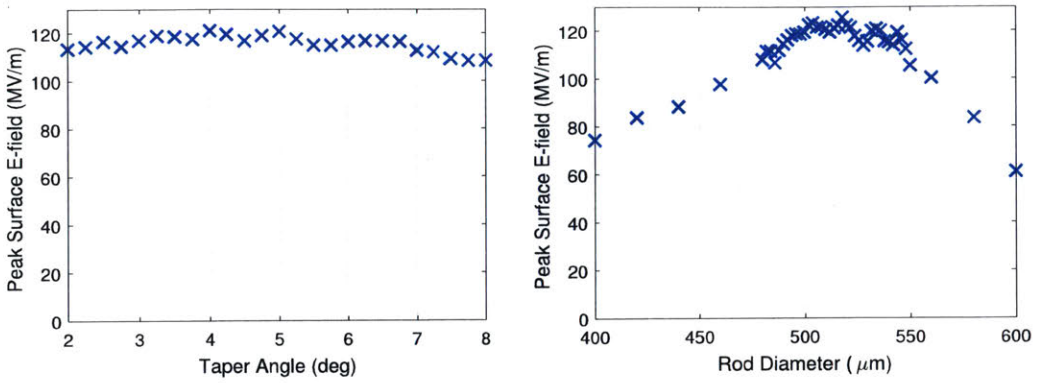

(a) (b)

Figure 5-19: a) The surface fields in the dielectric rod structure are not affected by variations in the angle of the alumina plate taper of up to $\pm$ 2 degrees about the nominal 5 degree value. b) The radius of the dielectric rod sample, in this case alumina, must be kept within a 50 micrometer range to achieve high surface electric fields.

easily measurable dimension. Many rods of each test material were purchased, and samples that were measured to be within 5 micrometers of the design diameter were used in testing.

Because the dielectric rods used in this test structure were very small compared to the wavelength of the 110 GHz microwaves, for efficient coupling, the Gaussian beam of microwaves had to be focused nearly as small as physically possible. An off axis parabolic mirror was used to focus a Gaussian beam to a 1.5 mm beam waist (0.55λ). It can be seen in Fig. 5-20 that this introduced a significant smearing of the beam waist. The coordinate system in this figure is the same as that in Figs. 5-15 and 5-16. The effect of this beam distortion on the excitation of the mode of the dielectric rod waveguide was examined. It was found that, by offsetting the incoming microwave beam in the z direction, this effect could be compensated for. Figure 5-21 shows that, by offsetting the beam by -1.8 mm, peak surface electric fields in excess of 120 MV/m could be recovered, the same values that were calculated with an ideal Gaussian beam input. Figure 5-22 shows the coupling of this tightly focused beam to the experimental test structure.

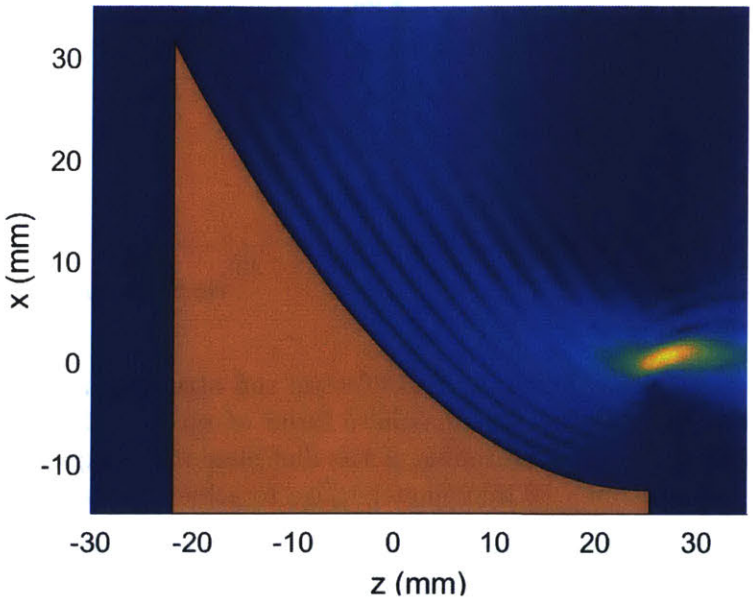

Figure 5-20: Illustration of smearing of the Gaussian beam waist introduced by using a short focal length, off axis parabolic mirror to focus to a waist of 0.55λ for coupling to a dielectric rod. A Gaussian beam of 110 GHz microwaves is incident from the positive x direction. In experiment, the normal electric field test structure would be placed at the focus of the microwave beam ($z = 27.1$ mm), and extend in the positive x direction. This is shown in Fig. 5-22.

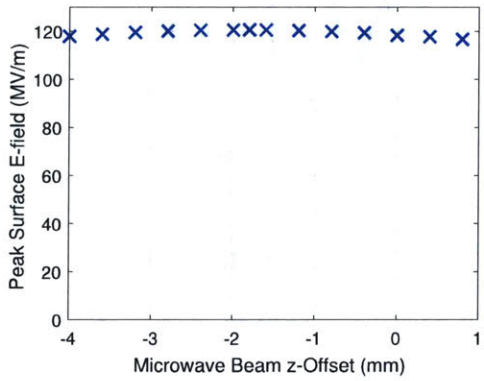

Figure 5-21: By offsetting the beam input to the short focal length parabolic mirror, the distortion of the Gaussian beam can be compensated for. The peak surface field on this example alumina rod recovers to greater than 120 MV/m with 1 MW of input power with a -1.8 mm offset in the z coordinate of Fig. 5-20.

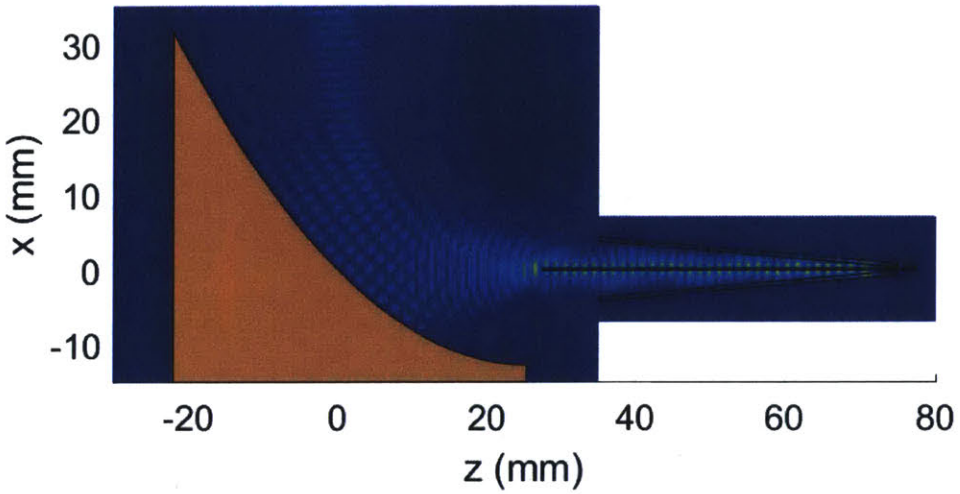

Figure 5-22: Efficiently coupling to the dielectric rod structure could be achieved despite the distortions introduced by the short focal length off axis parabolic mirror, seen in Fig. 5-20. In this figure, the incoming beam is offset horizontally -1.8 mm to compensate for the distortion.

5.2.4 Diagnostics

Three diagnostics were employed to detect and study multipactor discharges. The first two are shown in Fig. 5-1. RF diodes combined with a power divider were used to monitor forward power and reflected power from the structures. Microwave power that was scattered or absorbed by a multipactor discharge would show up as a change in the reflected power signal. From the resonant cavity for studying tangential electric fields, this would be a change in the cavity coupling, which could result in an increase or decrease in reflected power, depending on the exact parameters of the cavity. For the dielectric rod structure, missing microwave power was directly measurable as a decreased ratio of reflected power to forward power. The response of the RF diodes allowed for time resolution of nanoseconds.

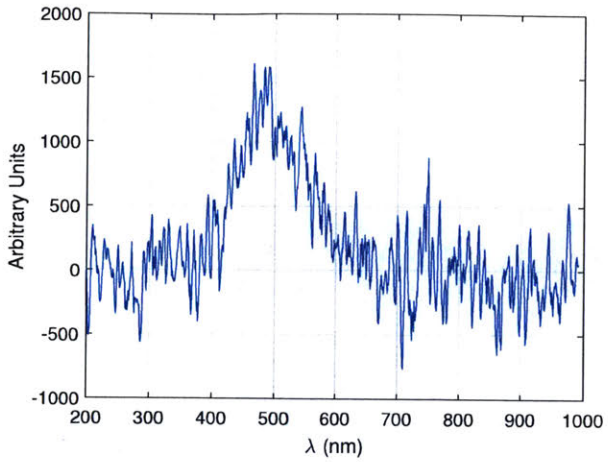

Figure 5-23: An example spectrum of light emitted from a multipactor discharge on an alumina rod. This spectrum was averaged over 1000 pulses, 3 microseconds each.

An intensified CCD imager (ICCD) was used to collect visible light from the experiments. Light from each 3 microsecond pulse of microwaves was integrated throughout the pulse. Light emitted by a dielectric multipactor is likely due to electroluminescense [97]. Impacting electrons create excited electrons and holes in the surface layers of the dielectric material. Radiative recombination of electrons and holes releases photons, resulting in a broad spectrum. The peak emission wavelength, near 490 nm for alumina, is determined by the band gap energy of the excited material. An example spectrum averaged over 1000 pulses on an alumina rod is shown in Fig. 5-23.

Electrons accelerated out the side of the test structures were collected as a means to detect multipactor. CAD drawings of each test structure, including all support structure, are shown in Fig. 5-24. On the right side of each structure is mounted a piece of copper sheet, with a concave angle facing the high field point of the dielectric sample under test. This copper piece was electrically isolated from the test structures and connected to a 50 Ohm terminal of an oscilloscope to monitor its floating potential. These dark current monitors were used to detect the presence of an energetic cloud of electrons. The monitors presented a concave face to the experiment to reduce reflection of impacting electrons.

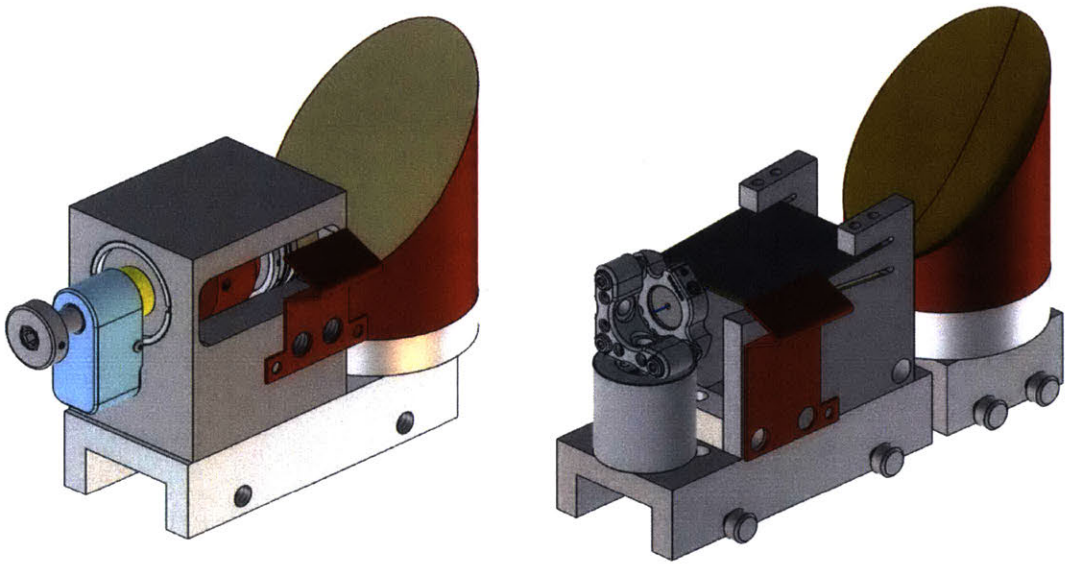

(a) Tangential electric field Structure

(b) Normal electric field Structure

Figure 5-24: Dielectric multipactor test structures. The angled copper sheet on the right side of each structure was a dark current monitor, a collector of energetic electrons.

5.2.5 Validation of Field Geometry in Normal Electric Field Structure

Because the dielectric rod test setup was not a resonant design, low power testing would not show any unique features that could be used to verify that the experimental structure matched the modeled structure. In lieu of a low power test, the visible light diagnostic was used during high power testing to verify the field structure along the dielectric rod. Figure 5-25a shows a visible light image of the test structure mounted in the vacuum chamber of the test stand. Figure 5-25b is a 3 microsecond image capturing light emission due to multipactor along the surface of the dielectric rod. In Fig. 5-26, the pattern of the visible light emission along the rod is compared to the calculated pattern of the square of the electric field along the surface of the rod. The spacing of intensity features is recreated, including the greater than half-wavelength wide maximum where the mode of the dielectric rod is cutoff and reflected. There is no theory for light intensity produced as a function of field strength in a dielectric

(a) Image of the dielectric rod structure in the high power test stand

(b) Light emission due to multipactor on an alumina rod

Figure 5-25: Black and white images showing the location of visible light emission along an alumina rod in high power testing.

(a) Light emission due to multipactor on an alumina rod

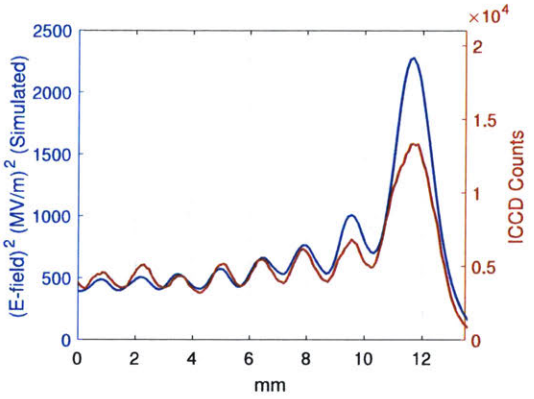

(b) RF Intensity structure versus Visible Light

Figure 5-26: A measure of brightness of visible light emission from a multipactor discharge versus the calculated electric field structure along the surface of an alumina rod.

multipactor. The amplitude of the visible light is simply compared to the square of the RF electric field, which is proportional to the RF power density flowing along the surface at each location. The agreement between the pattern of light and the calculated field structure shows that the mode of the dielectric rod is being excited, compressed, and reflected as anticipated from modeling.

Chapter 6

High Power Tests of Dielectric Multipactor at 110 GHz

Samples of sapphire, alumina, fused quartz, crystal quartz, and high resistivity silicon were tested in the structures of chapter 5, using the high power millimeter wave gyrotron described in chapter 2. Crystal quartz and silicon were only tested with tangential RF electric fields. The gyrotron was operated with 3 microsecond pulses at 110 GHz with a 1 Hz repetition rate for the duration of this study. Samples were cleaned for testing by sonicating them twice, once in acetone and once in ethanol. Test structures were assembled with sample materials and placed in a vacuum chamber, that was pumped to a base pressure of less than 1×10^{-8} Torr. The vacuum chamber, shown in Fig. 5-1, was mounted on a 3-axis translation stage. Precise alignment between the structure and the microwave beam was done using the dark current diagnostic for multipactor detection, described in section 5.2.4. It was found that the dark current monitor was low noise and highly sensitive to the presence of multipactor. The position of the vacuum chamber was tweaked to maximize the observed dark current for a given incident power level.

This same technique was employed for tuning the length of the Fabry-Perot cavity used to test samples with a tangential RF electric field. Initial tuning was done by minimizing the signal reflected from the cavity. Additional fine tuning ($\leq$ 300 nm) was performed, maximizing the dark current for a given incident microwave power.

To maximize the RF electric fields that the samples could be tested with, every sample was subjected to at least 150 thousand high power microwave pulses, slowly increasing in maximum incident power. This process allowed for slow outgassing of the surfaces under high electric fields and localized heating from multipactor. The exception to this was the samples of fused quartz, crystal quartz, and high resistivity silicon tested in the tangential electric field test structure. Confirmed with two samples each, the fused and crystal quartz wafers suffered structural damage from less than 5000 pulses in which multipactor discharge occurred. This damage occurred at the lowest value of RF electric field that would cause multipactor, just above the multipactor onset threshold. Also confirmed with two samples, high resistivity silicon wafer could not sustain fields high enough for multipactor to develop. Instead, breakdowns occurred above 13 MV/m, which steadily eroded the sample.

The maximum RF electric fields in the plots throughout this chapter are the maximum fields that could be achieved without the occurrence of a breakdown after 150 thousand processing pulses.

6.1 Results from Light Emission Diagnostics

6.1.1 Light with Tangential Electric Fields

The first diagnostic used to detect the presence of multipactor was visible light emission, captured with an Intensified CCD imager (ICCD). An example glow due to multipactor in the tangential electric field structure can be seen in Fig. 6-1. Figure 6-1b shows a black and white image of the test structure in the vacuum chamber oriented similar to the CAD model in Fig. 6-1a. The image is looking through the side of the support structure that is shown clearly in Fig. 5-24a. A focused microwave beam is incident from the left side of Fig. 6-1. Because the image is looking through the side of the Fabry-Perot cavity, the sample wafer of sapphire is being imaged nearly on edge. The glow on the surface is readily detectable in Fig. 6-1c. The light in the central bright spot was collected over the 3 microsecond microwave pulse for analysis.

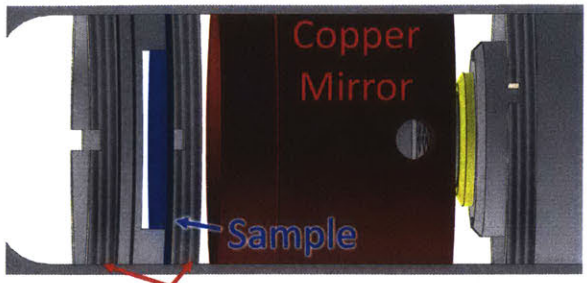

(a) CAD model of the tangential electric field cavity

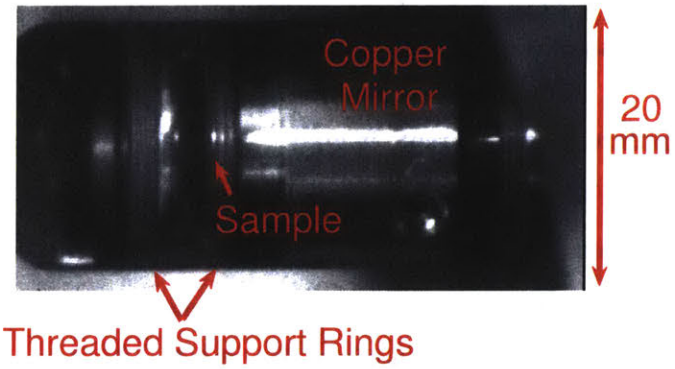

(b) Black and white ICCD image of the tangential electric field cavity

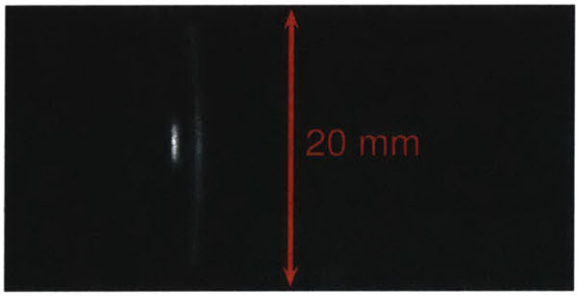

(c) Visible light emission from multipactor on a sapphire wafer

Figure 6-1: Visible light emission from multipactor on sapphire with a tangential electric field. The light emission was averaged over 300, 3 microsecond pulses.

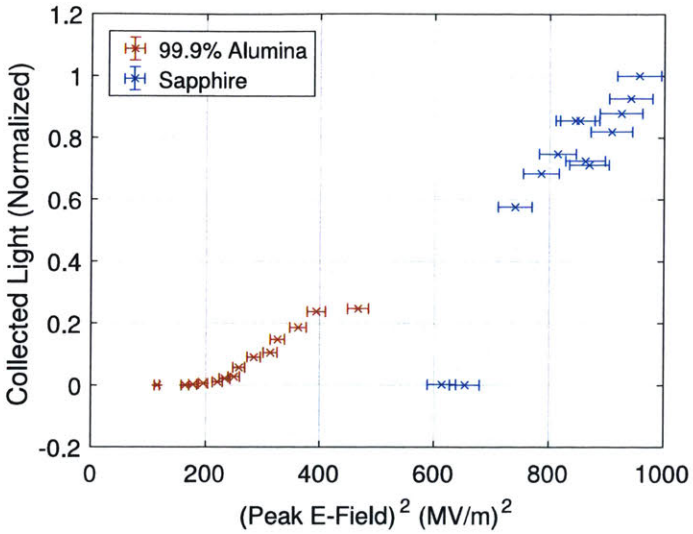

Figure 6-2: Visible light emission from multipactor with a tangential electric field. The light emission was averaged over 300, 3 microsecond pulses.

Because the sapphire is transparent, it guides some of the light to the edges of the wafer. Only light in the central bright spot, located in the center of each wafer, was as data, for consistency between opaque and transparent materials.

With a tangential RF electric field, the dependence of the collected light on the strength of the RF electric field is shown in Fig. 6-2 for alumina and sapphire. Both data sets are normalized to the same level. The horizontal error bars on this plot, and all plots in this chapter, are due to a systematic uncertainty in the absolute calibration of the electric fields. This is dominated by an uncertainty in the accuracy of the numerical calculations performed with ANSYS Electronics Desktop. For the purposes of these plots. The results of those calculations have been assigned a 1σ uncertainty of 2%. The electric fields on the horizontal axis have not been corrected for the changing cavity parameters due to the formation of multipactor. It will be shown in section 6.4.1 that the additional cavity loss due to absorption or scattering introduced by the multipactor is less than 0.5%. The fields in the cavity were dominated by the fraction of power coupling through the dielectric mirror (3.2%).

The results of Fig. 6-2 are separated for a more detailed examination in Fig. 6-3. The systematic uncertainty in RF electric field strength has been omitted for clarity. Visible light data is plotted versus the square of the electric field. Without

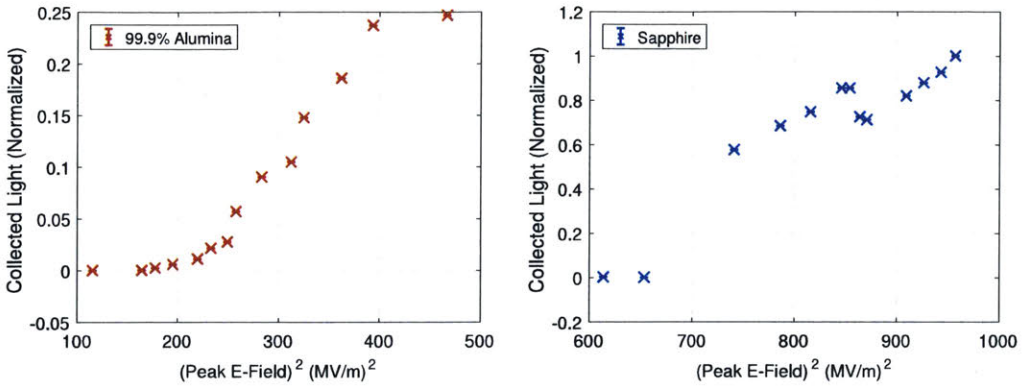

(a) Alumina (b) Sapphire

Figure 6-3: Visible light emission from multipactor with a tangential electric field. The light emission was averaged over 300, 3 microsecond pulses. The systematic uncertainty in electric field has been omitted for clarity.

a rigorous theory of electroluminescence due to multipactor, one would expect the light emission to rise linearly with available microwave power ($\propto E_{RF}^2$). This is especially true in the case of tangential RF electric fields, where the fraction of power absorbed is theoretically independent of the surface RF electric field (section 4.4.1). Complications to simple linear scaling of light emission with microwave power could arise from a changing area of multipactor discharge with increasing field strength. As this measurement was integrated over the length of the microwave pulse, it is not sensitive to length of multipactor pulses, if the rise time of multipactor is dependent upon the RF electric field strength. Other, time resolved diagnostics indicated that the multipactor developed on the rise of the microwave pulse in the majority of recorded data. These diagnostics will be presented in later sections of this chapter.

In the sapphire data, the sharp change in behavior at 29.4 MV/m ($E_{RF}^2 = 864$ $(\mathrm{MV/m})^2$) is due to the development of multipactor on the second side of the sapphire wafer. The development of a second multipactor leads to additional loss in the Fabry-Perot cavity, lowering the actual RF electric field on the surfaces of the sample. In Fig. 6-3a, the very last data point on the alumina sample also has a shift in slope of light versus RF electric field. This is also due to the development of multipactor on the second side of the sample.

6.1.2 Light with Normal Electric Fields

An example glow due to multipactor in the normal electric field structure can be seen in Fig. 6-4. Figure 6-4b shows a black and white image of the test structure in the vacuum chamber, in a similar orientation to the CAD model in Fig. 6-4a. The image is looking through the side of the support structure that is shown clearly in Fig. 5-24b. The dielectric rod that serves as both waveguide and test sample is horizontal in the middle of the image. Two white alumina plates form a taper above and below the rod. An example glow from multipactor discharge on an alumina rod is shown in Fig. 6-4c. The glow shows the pattern of a standing wave along the rod. Near the brightest spot, there is an additional glow just above and below the rod. This is due to reflection of light from the polished surfaces of the alumina plates that form the taper in the structure. For the plots below, light was collected over the area of the rod where the brightest spot exists, containing the high RF electric field spot in the structure.

With a normal RF electric field, the dependence of light on the RF electric field intensity is shown in Fig. 6-5 for alumina, sapphire and fused quartz. The *Corrected* label for the electric fields indicates that the values have been adjusted to account for the absorbed or scattered RF power that was measured to be missing from the reflected RF signal (to be discussed in section 6.4.2). The fraction of power lost to dielectric multipactor with normal RF electric fields is not negligible. For all three materials, the light emission is nearly linear with the square of the RF electric field. The vertical error bars are the standard deviation of the light emission, averaged over 300 pulses. For comparison, the data from all three samples is normalized to the same amplitude. The uncertainty is larger for the fused quartz data, because the emission was much fainter.

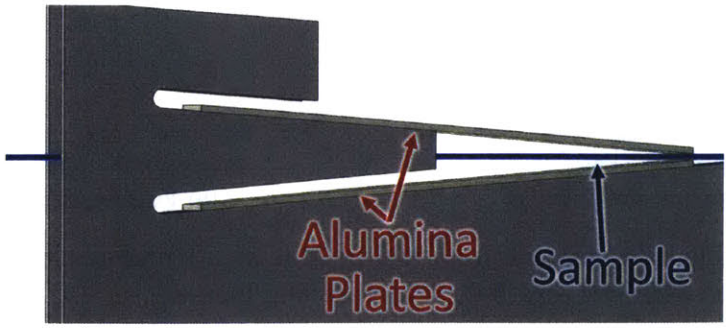

(a) CAD model of the normal electric field structure

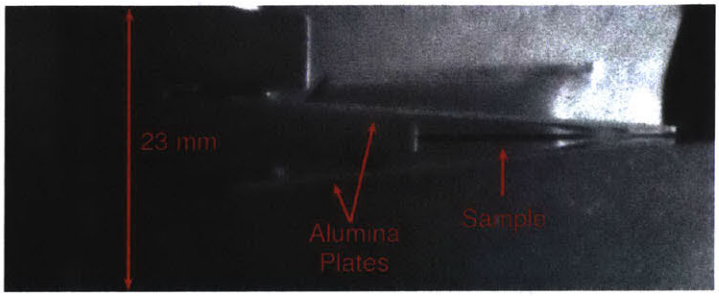

(b) Black and white ICCD image of the normal electric field structure

(c) Visible light emission from multipactor on an alumina rod

Figure 6-4: Visible light emission from multipactor on alumina with a normal electric field. The light emission was averaged over a 3 microsecond pulse.

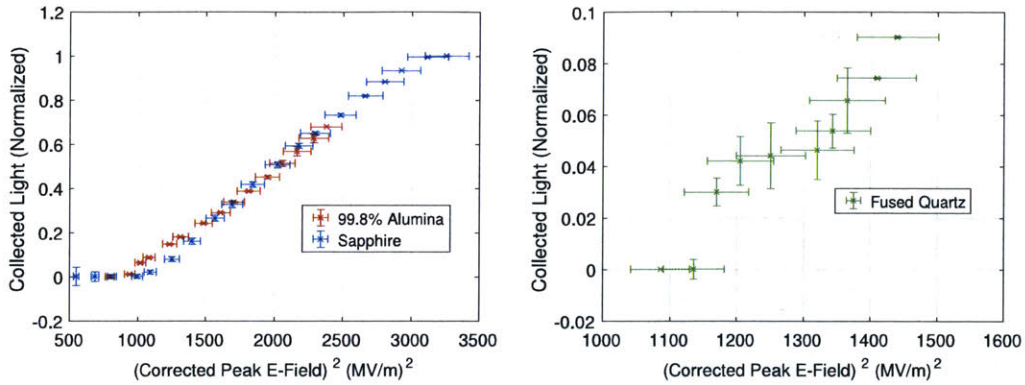

(a) Sapphire and Alumina (b) Fused Quartz

Figure 6-5: Visible light emission from multipactor with a normal electric field. The light emission was averaged over 300, 3 microsecond pulses.

6.1.3 Speculation: Why is light emission linear with RF power for normal electric fields?

This subsection discusses a possible explanation of the data in Fig. 6-5. It is, however, speculation on the author's part. The primary purpose of the visible light diagnostic (as well as the dark current diagnostic) was a binary detection of multipactor, for the purpose of determining threshold electric fields. A rigorous theory of electroluminescence due to multipactor is beyond the scope of this thesis.

Electroluminescence due to multipactor with normal electric fields is complex. The fraction of RF power deposited onto the dielectric by colliding electrons theoretical increases proportional to the RF electric field (the square root of the incident RF power, see section 4.4.2). This difference from tangential electric fields (fractional power absorption independent of field strength) is due to the average impact energy of the electrons increasing.

The number of electrons in a multipactor layer increase linearly with E_{RF}, due to the shape of the multipactor susceptibility region lower boundaries, true for either normal or tangential RF electric fields. The number of high energy electron impacts per RF cycle with tangential electric fields (N/τ from Eq. 4.12) scales with an additional factor of E_{RF} due to the impact time τ scaling as E_{RF}^{-1}. With normal

electric fields, τ in a saturated multipactor is equal to one RF cycle for high energy electrons. Due to the shape of Vaughan's model of secondary electron yield, however, the fraction of electrons in the multipactor layer that gain high energy in an RF cycle increases with E_{RF} to maintain an average secondary electron yield of 1 as the average impact energy increases beyond the peak in Vaughan's model. The shape of Vaughan's model to the right of the peak (see 3-2), combined with the scaling of impact energy for high energy electrons from a normal field multipactor, Eq. 4.13, lead to the fraction of multipactor electrons gaining significant energy to increase roughly linearly with E_{RF} in the limited electric field range of the experiments.

Thus, as with tangential electric fields, the number of electrons impacting the dielectric with energy above the band gap of the dielectric will scale as E_{RF}^2. It is speculated that the excess energy of a colliding electron above the band gap may impart more energy to the electrons that it excites to the conducting band, rather than creating additional electron-hole pairs. Assuming this conjecture is correct, the produced light will scale as E_{RF}^2, because, regardless of energy gained, a freed electron will tend to relax back to the band gap energy of the dielectric material before decaying to the ground state through photon emission.

6.2 Results from Dark Current Diagnostics

6.2.1 Dark Current with Tangential Electric Fields

The second diagnostic used to detect multipactor was a dark current collector, physically illustrated in 5-24. This dark current collector was electrically isolated from the test structures and connected to the 50 Ohm terminal of an oscilloscope. Example oscillograms are shown in Fig. 6-6. These examples were collected during the testing of a sapphire rod. For demonstration, Fig. 6-6b is an exceptional pulse, where the multipactor took nearly a microsecond to develop. In the vast majority of recorded pulses, multipactor occurred promptly during the rise of the microwave pulse and persisted throughout the pulse, as in Fig. 6-6a. The data presented in the following

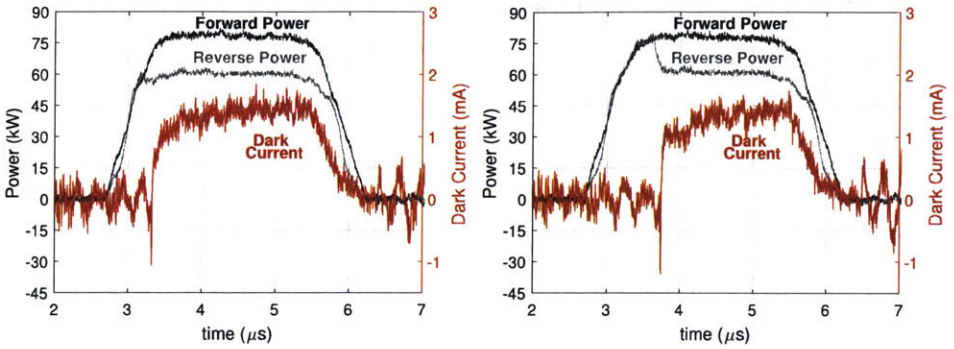

(a) Typical pulse with multipactor developing on the rise of the microwave pulse

(b) Pulse with delayed multipactor onset

Figure 6-6: Traces of forward power, reflected power, and collected current from example high power pulses on sapphire in the normal electric field structure. The timing of the multipactor is most readily apparent in the missing power from the *Reverse Power* traces. There is some charging of the *Dark Current* probe that delays the response. These traces correspond to about 43 MV/m peak surface RF electric fields.

plots was averaged over the central microsecond of the microwave pulse (4 μs to 5 μs in Fig. 6-6), and subsequently averaged over 300 pulses. Also visible in Fig. 6-6 is the reduction in power reflected from the sapphire rod after the onset of multipactor.

Figure 6-7 shows the dependence of dark current versus RF electric field strength with a tangential RF electric field. The small uncertainty in this measurement made it particularly useful for determining threshold RF electric fields for the onset of multipactor.

The sudden jumps in the data of Fig. 6-7, as well as later figures in this chapter are due to the charging of the dielectric as the multipactor forms and saturates. The dielectric is rapidly charged to DC electric fields on the order of one tenth the RF electric fields, drastically effecting the dynamics of electrons in the multipactor. For this reason, data will tend to jump to nonzero values as multipactor is formed, rather than form a smooth trend to zero signal. The effect is more pronounce, the higher the RF electric field that multipactor forms at.

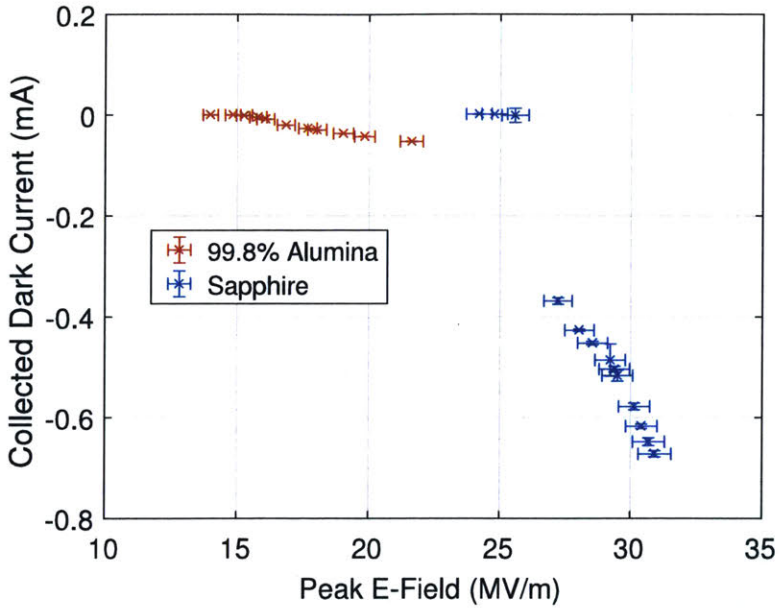

Figure 6-7: Dependence of collected dark current on the RF electric field strength with tangential fields, averaged over 300 pulses.

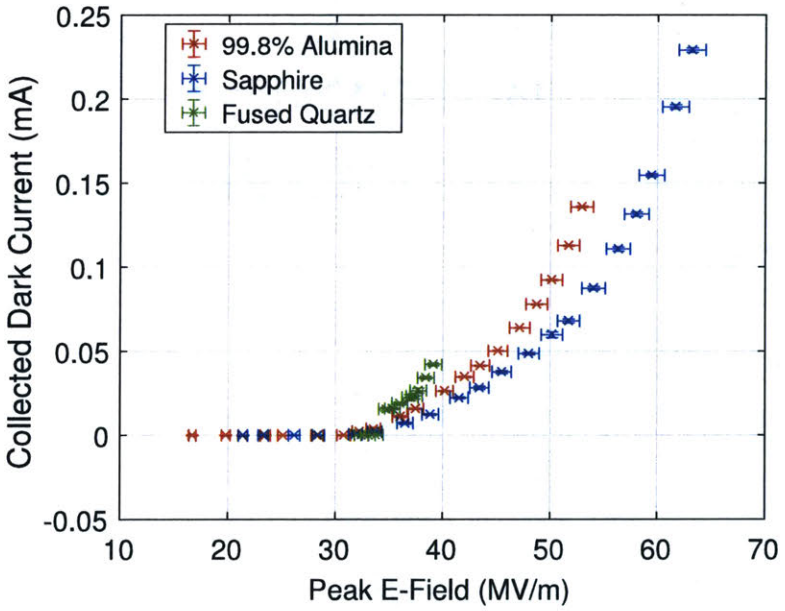

Figure 6-8: Dependence of collected dark current on the RF electric field strength with normal fields, averaged over 300 pulses.

6.2.2 Dark Current with Normal Electric Fields

Figure 6-8 shows the dependence of dark current versus RF electric field strength with a normal RF electric field. Because the quartz rod tested was larger diameter (0.8 mm vs 0.5 mm for sapphire and alumina), the dark current monitor had a 60% larger solid angle for collection of current from the quartz sample. This may contribute to the quartz data being significantly higher for a given RF electric field. As with the measurements with tangential RF electric fields, the data from the dark current monitor was precise and low noise, proving very useful for determination of multipactor onset thresholds.

The exact dependence of the magnitude of the dark current signal depended not only on the number and energy of the electrons escaping a multipactor, but also the geometry and secondary electron yield of the dark current collector itself. Due to the extended nature of the studied multipactors, and the desire to maximize sensitivity, the dark current collectors were designed with maximum collecting area. This lead to many secondary electrons generated by impacts from energetic multipactor electrons to escape the collectors. This is seen clearly in the positive currents measured in Fig. 6-8, where more secondary electrons were generated on the collector than incident electrons impacted it.

The data from the dark current monitors is used only for measurements of multipactor onset thresholds. For this purpose, it was the most sensitive and least noisy diagnostic employed. The dependence of the collected current on RF electric field strength above the multipactor threshold is not analyzed, for it has as much to do with the geometry and material of the collector as with the multipactor discharges. Study of the energy spectrum of electrons escaping a multipactor would be better served with closed experimental structures where all electrons could be captured, much different from the open structures employed in these experiments.

Material	Tangential E $[\frac{MV}{m}]$	σ $[\frac{MV}{m}]$	Model $[\frac{MV}{m}]$	Normal E $[\frac{MV}{m}]$	σ $[\frac{MV}{m}]$	model $[\frac{MV}{m}]$
Alumina	15.0	0.4	15.5	31.3	0.9	16.9
Sapphire	26.4	0.8	15.5	32.3	1.0	16.9
Fused Quartz	29.6	0.8	21.6	33.9	0.7	24.2
Crystal Quartz	24.8	0.5	27.7	N/A	N/A	N/A
Silicon* (Breakdown)	13	1	44.0	N/A	N/A	N/A

Table 6.1: Threshold RF electric fields for the onset of multipactor discharge, measured at 110 GHz. The measured thresholds are the same whether using visible light or dark current to detect the presence of multipactor. *Note that silicon failed due to electrical breakdown at 13 MV/m surface fields, but multipactor was not detected.

6.3 Measured Multipactor Discharge Thresholds

The visible light and dark current diagnostics were used to determine threshold values of RF electric field for the onset of multipactor. The threshold value was assumed to be midway between the first measurement that was at least two sigma from zero and the next lower measurement of electric field. The step size between these two data points was treated as a 2σ uncertainty, and added in quadrature with the systematic uncertainty in RF electric field. This method was employed, rather than a fitting a generic function to the plotted data, because the data tends to suddenly jump at the onset of multipactor (due to dielectric charging), rather than smoothly trend to zero signal. For both RF field orientations, the thresholds calculated from the dark current data and the collected light data were in agreement. Both diagnostics detected the multipactor onset on the same data points.

Measured thresholds are given in Table 6.1. In the table, the measured results are compared to predictions from Table 4.2. Predictions for alumina were made for a specific formulation of alumina (Lucalox) that reproduces the secondary electron yield properties of sapphire. The exact SEY properties of the high purity alumina tested are not precisely known.

The measured thresholds are compared to existing data in Fig. 6-9. Prior published data consists of two points for fused quartz (at 1.95 and 9.4 GHz) and one data point for alumina (at 11.424 GHz). The measured threshold for fused quartz at

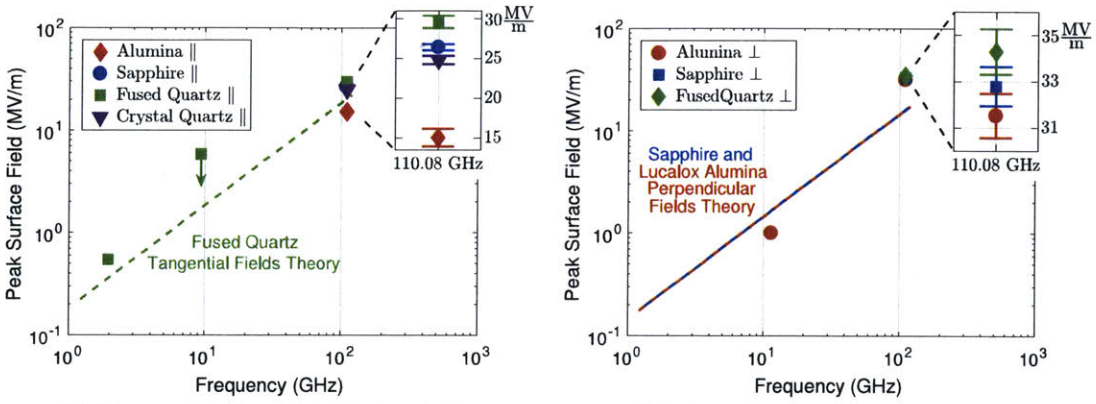

(a) Tangential electric field thresholds

(b) Normal electric field thresholds

Figure 6-9: Multipactor discharge threshold RF electric fields. Data at 110 GHz is from this study. Data below 110 GHz was previously published by other groups. The model lines are the values from Table 4.2.

9.4 GHz is an upper, because it was only detected indirectly when multipactor had built up enough to cause the test cavity to go out of resonance. Precise measurement of the multipactor onset threshold was not the goal of that study. There is just enough data to suggest that, for fused quartz with tangential RF electric fields, and alumina with normal RF electric fields, the thresholds scale linearly with frequency. This is a promising result for future applications of high power microwave and THz applications at even higher frequencies.

The dashed lines are the frequency dependence of the multipactor thresholds from Table 4.2. These theoretical thresholds were calculated for an infinite plane wave, to serve as a lower bound to the multipactor thresholds for any experimental geometry. The theory was found to under-predict multipactor thresholds by a factor of 1.2-1.7. For an easily calculable expression, this is still a very useful result for the design of future devices and experiments.

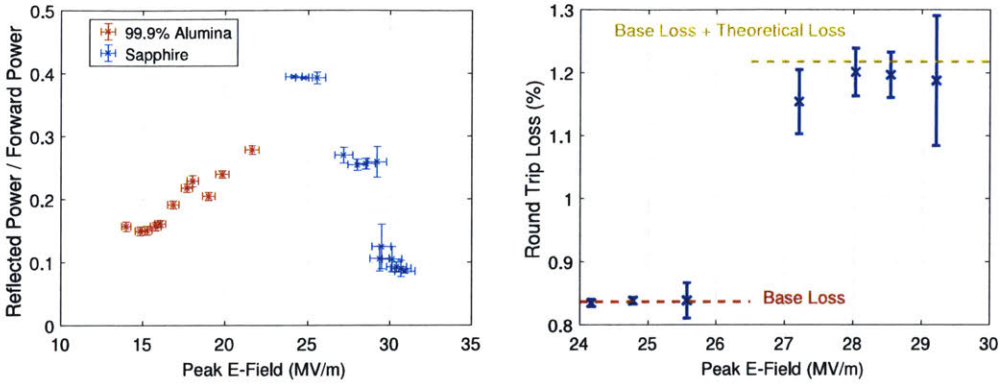

(a) Power reflected from the tangential electric field test structure.

(b) Calculated round trip loss in test cavity compared to theory.

Figure 6-10: Power absorption due to multipactor discharge with tangential electric fields. The systematic uncertainty in electric field has been omitted in b) for clarity.

6.4 Results from Reflected Power Diagnostics

6.4.1 Reflected Power with Tangential Electric Fields

A third diagnostic, reflected power, was also monitored during dielectric multipactor testing. Compared to the other two diagnostics, it was significantly less precise. It was therefore not as sensitive at detecting the threshold fields for multipactor onset. It does, however, provide an opportunity to test the power absorption by multipactor predicted in section 4.4. Notably, this allows the testing of the predictions that power loss is relatively independent of RF electric field strength with tangential RF electric fields, and linearly dependent on field strength with normal RF electric fields.

The reflected power measured from the Fabry-Perot cavity used for tests with tangential RF electric fields is shown in Fig. 6-10a. The data from the sapphire sample shows larger reflectance, giving a better signal for this diagnostic. This is because, for the later test of the alumina sample, the Fabry-Perot cavity was intentionally shortened by one half of an RF wavelength from its design value. This created a small mismatch in the curvature mode in the cavity and the curvature of the mirror at the end of the cavity, introducing a small amount of loss into the cavity. This was done to reduce the reflectivity of the cavity and yield more stable operation of the

gyrotron high power microwave source.

It is clearly noted in Fig. 6-10a that the missing power due to multipactor trends in opposite directions for alumina and sapphire. This is a result of the arrangement of the Fabry-Perot cavity. Minimum reflection from a cavity is achieved when the round trip loss in the cavity is equal to the fraction of power coupled into and out of the cavity, so-called critical coupling. With no multipactor, there is very little loss in the cavity with the sapphire sample. The additional loss due to the multipactor brought the cavity closer to critical coupling, lowering the cavity reflectivity. However, with the alumina sample, additional loss had intentionally been added to the cavity to reduce reflected power back into the gyrotron. This additional loss was greater than the fraction of power coupled through the semi-transparent mirror of the Fabry-Perot (3.2%). In this case, the additional loss due to multipactor drew the cavity further from the critically coupled condition, increasing cavity reflectivity. Additionally, loss due to the multipactor was small compared to the loss that was intentionally added to reduce reflection into the gyrotron. For this reason, the alumina signal was less sensitive to the power absorbed or scattered by the multipactor than the sapphire signal.

The first five data points for alumina are in agreement with a base cavity reflectivity of 0.15. Though the next five data points, where multipactor has formed on one side of the alumina sample, show an upward trend, they are all within 2σ of an average value of 0.22. The final, highest reflectivity data point is where the second side of the alumina wafer has developed multipactor, as evidenced from the visible light emission data in Fig. 6-2.

Because the loss in the Fabry-Perot cavity with the sapphire sample was tiny, the additional loss due to multipactor yielded unambiguous jumps in the reflectivity of the cavity. Additionally, the secondary electron yield parameters of sapphire are relatively well known, providing an excellent test of the theoretical predictions. Figure 6-10b shows a comparison of the predicted loss of RF power with the round trip loss in the cavity. Only absorption of RF energy by electrons impacting the dielectric surface is accounted for in the model. Scattering of RF power due to the thin layer

of electrons is neglected.

The round trip loss in the cavity was calculated from the reflectivity using Eq. 6.1, derivable from [98]. In this equation, b_1 is the amplitude of the reflected signal, equal to the square root of the reflectivity in Fig. 6-10a. The variable k_m is the fraction of power transmitted through the partially reflective mirror that forms one end of the Fabry-Perot cavity.

$$\text{round trip loss} = 1 - \frac{\pm b_1\sqrt{1-k_m^2} + 1 - k_m^2}{-b_1 k_m^2 + b_1 \pm \sqrt{1-k_m^2}} \tag{6.1}$$

The theoretical loss in Fig. 6-10b was calculated using an effective area of 0.07 mm^2. At 28 MV/m, this is the area of the microwave beam that is above the breakdown threshold. This does not account for any spreading of the multipactor region after the dielectric becomes charged. This single value of area was used for the range of RF electric field values plotted.

The loss from the multipactor on both sides of the sapphire wafer is not calculated, because, to keep the cavity in resonance, the length of the cavity had to be adjusted for the higher RF electric field data points. This introduces additional loss due to a mismatch between the cavity mode and the curvature of the copper mirror that forms one end of the cavity.

6.4.2 Reflected Power with Normal Electric Fields

Loss due to multipactor with normal RF electric fields is shown in Fig. 6-11 for samples of alumina, sapphire, and quartz. The "Corrected Peak E-field" on the x-axis of 6-11b accounts for the reduced electric field due to the absorption of RF power by the multipactor.

The theoretical loss is calculated assuming an effective area of 5 mm^2 for the sapphire rod (0.5mm diameter rod in a 40 mm long taper). The modeled loss matches the data well at low RF electric fields, but the loss on the sapphire and alumina rods appears to saturate above 40 MV/m. The quartz rod data was not modeled, because post experiment examination of the quartz rod tested showed structural

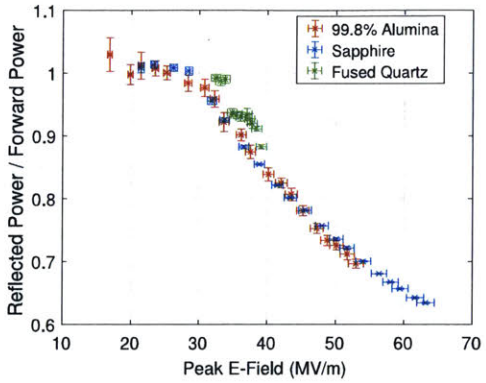

(a) Power reflected from the normal electric field test structure.

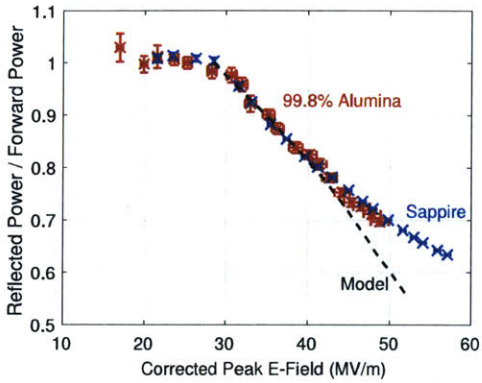

(b) Power absorption compared to theory.

Figure 6-11: Power absorption due to multipactor discharge with normal electric fields. The systematic uncertainty in electric field has been omitted in b) for clarity.

damage (missing material) near the high field location on the rod (see Section 6.5.2). This missing material would have caused an unknown amount of loss by scattering power from the propagating waveguide mode.

6.4.3 Conclusions from Reflected Power Diagnostic

For comparing RF power loss in experiment and theory, for both orientations of RF electric field, the breakdown threshold of the model curves was set at the measured value. This left one free parameter in the loss models, the "effective area." The nonuniformity of the experimental fields gave some leeway in this value. The purpose of this section is to demonstrate that the modeled loss fits well to the experimental data with realistic values of effective area. The model can thus be useful for estimating heat loads in future devices and experiments. This effective area, though, will have to be estimated, likely utilizing data from past experiments.

6.5 Observed Material Damage

6.5.1 Damage to Materials with Tangential Electric Fields

Figures 6-12 - 6-14 show visible light images of the tangential electric field samples after testing was complete. Sapphire and alumina samples showed discoloration. The discoloration was on both side of the samples, though it was very weak on the second side of the alumina sample.

Full processing could not occur on either fused quartz or crystal quartz samples. Within a few thousand shots of the development of multipactor, the quartz materials suffered structural damage. A small crack appeared in the fused quartz sample shown here in Fig. 6-13a. A large defect formed in the surface of the crystal quartz sample in Fig. 6-13b.

High resistivity silicon samples could not be tested to high enough RF electric fields to generate multipactor. Breakdowns would occur on the surface above 13 MV/m. On other samples, small breakdowns would clean the surface and cease after several high power pulses. In the case of silicon, the surface was damaged, and steady small breakdowns eventually eroded the surface enough to take the Fabry-Perot cavity out of resonance. The damage to the polished surface of the silicon can be clearly seen in Fig. 6-14.

6.5.2 Damage to Materials with Normal Electric Fields

Figure 6-15 shows metallic discoloration of the surfaces of alumina and sapphire rods after testing. The pattern of discoloration traces out the standing wave pattern of the normal electric field test structure. The pattern is more pronounced on the sapphire sample, likely because it was able to reach much higher values of RF electric field, and thus experience more energetic multipactor.

Figure 6-16 shows damage to the fused quartz rod after testing. Discoloration was limited to a browned region near the high field point on the rod. However, material was missing from one side of the rod near this high field point. As this was not a

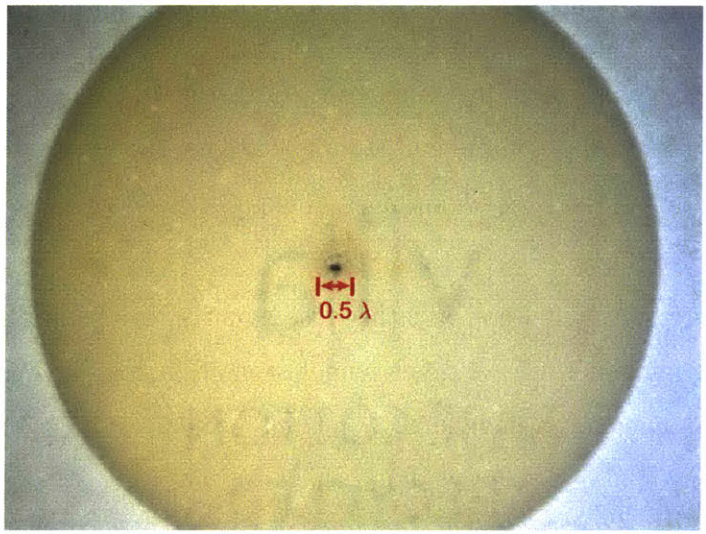

(a) 99.9% Alumina

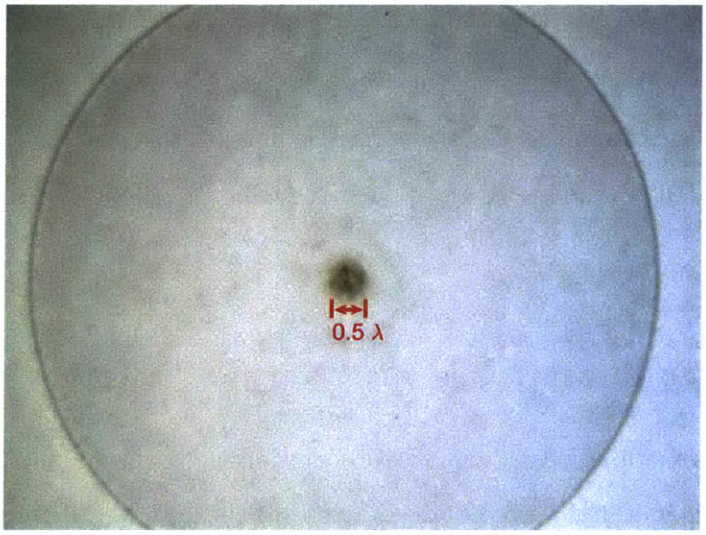

(b) Sapphire

Figure 6-12: Observed damage to wafers of alumina and sapphire tested with tangential electric fields. Discoloration was observed, but no material was eroded. Discoloration was observed on both sides of these samples.

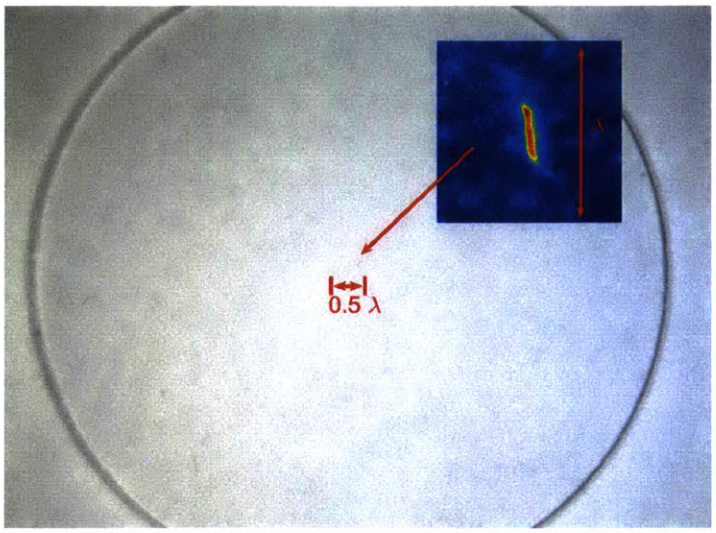

(a) Fused Quartz

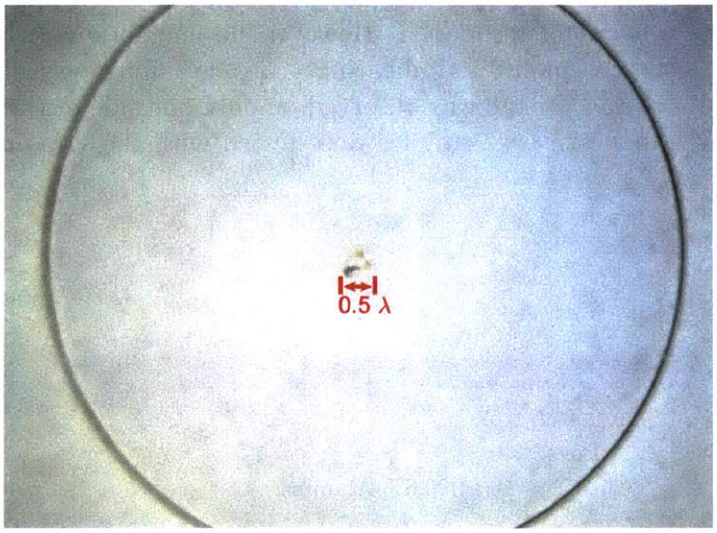

(b) Crystal Quartz

Figure 6-13: Observed damage to wafers of fused and crystal quartz tested with tangential electric fields. The false color inset in a) highlights a small crack that formed. The defect in b) is a chip of missing material. These material failures were large enough to disrupt the mode of the Fabry-Perot cavities in which the samples were being tested. Damage was limited to one side of these samples.

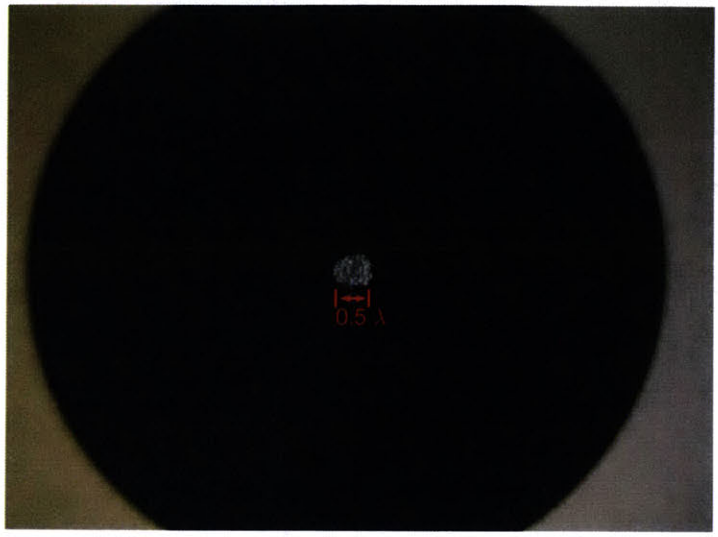

Figure 6-14: Observed damage to high resistivity silicon tested with tangential electric fields. In testing, the material was steadily eroded by breakdowns until the Fabry-Perot cavity was out of resonance. However, no energetic electrons were collected by the dark current monitor, indicating that the failure was not due to the formation of multipactor. Damage was observed on only one side of the wafer, where the electric field was highest. Two samples were tested with the same result.

(a) 99.8% Alumina

(b) Sapphire

Figure 6-15: Observed damage to rods of alumina and sapphire tested with normal electric fields. Discoloration was observed, but no material was eroded.

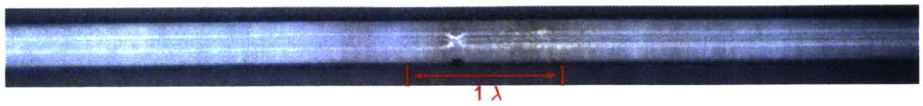

Figure 6-16: Observed damage to a fused quartz rod tested with normal electric fields. This photograph focuses on a section of material that was eroded by the multipactor discharge.

resonant structure, loss due to this defect did not affect the strength of fields in the structure by more than a few percent. From the first observation of multipactor, to the conclusion of the processing, the multipactor onset threshold rose by less than 5%. The sharp edge of this defect, however, may be the reason that the quartz rod could not be tested to very high RF electric field values, despite processing.

6.6 Conclusions of Dielectric Multipactor Testing

The experiments at 110 GHz have greatly expanded the set of published data available for understanding dielectric multipactor. The measurements of multipactor threshold fields were made at frequencies ten times higher than previously existing data. Compared with published data for fused quartz with tangential RF electric fields, and alumina with normal RF electric fields, it can be concluded that multipactor onset thresholds scale linearly with frequency, as predicted in [6] and later theoretical papers. This is a very promising result for future applications, especially at even higher microwave frequencies.

Furthermore, the simple method for calculating lower bound multipactor thresholds in section 4.5 was found to be within a factor of two of all existing experimental data, regardless of experiment geometry. The simple theory was found to underpredict breakdown thresholds by a factor of 1.4-2. This yields safe lower bound predictions that could be used to avoid multipactor in the design of future experiments or high power microwave devices.

Experimental data was collected to verify predicted values of power absorption by multipactor. With normal RF electric fields, the power absorption was found to

scale roughly linearly with RF electric field, in agreement with the theory (section 4.4.2). This was observed once before in an experiment performed at 11.424 GHz in [76]. With tangential RF electric fields, power absorption was found to be largely independent of RF electric field strength. This was predicted in [22], but never experimentally tested. Finally, the theoretical values of power absorption, in either field orientation, were found to agree with experimental data with realistic values of effective area. Thus, these models can be useful for estimating heat loads in devices and experiments that cannot avoid operational regimes with dielectric multipactor.

Post-experiment examination of tested samples revealed that alumina and sapphire materials were discolored, but largely undamaged after 150 thousand high power pulses. With normal electric fields, alumina was found to perform nearly as well as sapphire. These two materials seem suitable for use in high power microwave devices and accelerators in which multipactor may occur. Conversely, every sample of fused or crystal quartz suffered structural damage from multipactor. Multipactor on these materials should be minimized in high power microwave devices.

High resistivity silicon has low microwave loss, and low secondary electron yield, suggesting that it would be a useful material. However, in testing with tangential RF electric fields at 110 GHz, this material was unable to sustain fields above a relatively low 13 MV/m without the occurrence of breakdowns resulting in severe surface damage. High resistivity silicon is likely unsuitable for high power microwave applications with high surface electric fields.

Chapter 7

Microwave Breakdown in Air at 110 GHz: Introduction and Prior Work

This chapter and chapter 8 relate studies of microwave gas breakdown at millimeter wave frequencies, specifically at 110 - 124 GHz. A "breakdown", here, is when a sufficiently strong electric field is applied across a gas, such that it is partially ionized and becomes conductive. The study of gas breakdown with DC fields dates back centuries, leading to such fundamental discoveries as cathode rays (electron beams), x-rays, and optical spectroscopy. Extensions of the field to RF and microwave frequency electric fields, however, are more recent, beginning in the mid 1940's.

When an electric field of sufficient strength to produce a breakdown is applied across a gas, electrons and ions in the gaseous medium are accelerated to very high energies. Unless the frequency of the field is high enough so that the direction of the force on the charged particles is changed before the particles traverse the gas-containing enclosure, impacts with walls or electrodes are likely to produce other charged particles, multiplying the electron or ion concentration in the gas. When the rate at which electrons are produced exceeds the rate at which they disappear, the rapid increase in concentration causes the gas to become conductive and visibly emissive, constituting a breakdown. The electrons tend to play a dominant role in the breakdown process, because they are accelerated so much more by a given electric field than the more massive ions. Secondary electron and ion production by impacts

on walls or electrodes are characteristics of DC and low frequency breakdowns. Such breakdowns can be more dependent on the material and condition of electrode surfaces than on the properties of the gases being studied.

Microwave breakdown in gases flourished as a field of study only after World War II, as the development of radar led to widespread use and improvement of powerful microwave equipment. The very high frequencies ($>$ 300 MHz) used in studies of microwave breakdowns mean that, when fields are applied across a gas, electrons move only a short distance before the direction of the field is reversed. Electrons are not swept out of the discharge region by the electric field, but rather drift out with relatively low velocities, producing few secondary effects at the surfaces of the gas-containing enclosure. This is the defining characteristic of studies of microwave breakdowns versus earlier studies of low frequency discharges. Studies of microwave breakdowns allow the study of interactions between electrons, atoms, and ions without disturbance from the surrounding container or electrodes.

Breakdowns at conventional microwave frequencies, ranging up to a few 10's of GHz, have been extensively studied since the mid 1940's [99,100]. Particular emphasis was placed on predictions of breakdown threshold electric fields as a function of gas species, pressure, and experimental geometry, in the first two decades [101]. The development of high power sources at millimeter wave frequencies (30 - 300 GHz), motivated largely by nuclear fusion research, has opened up a new regime for study [102–104]. The development of high power, high frequency sources, such as gyrotrons, has made it possible to create plasmas in free space in atmospheric pressure air at frequencies greater than 100 GHz [105, 106].

Understanding microwave breakdowns at millimeter wave and higher frequencies is potentially useful for exotic applications such as remote detection of radioactive materials [107–109] or beamed energy rocket propulsion [105, 110]. In current and near future applications such as high frequency, high altitude radar, it is important that breakdown thresholds in air are accurately known, so that breakdowns can be avoided.

From 2008 to 2016, a series of experiments were performed to study a unique

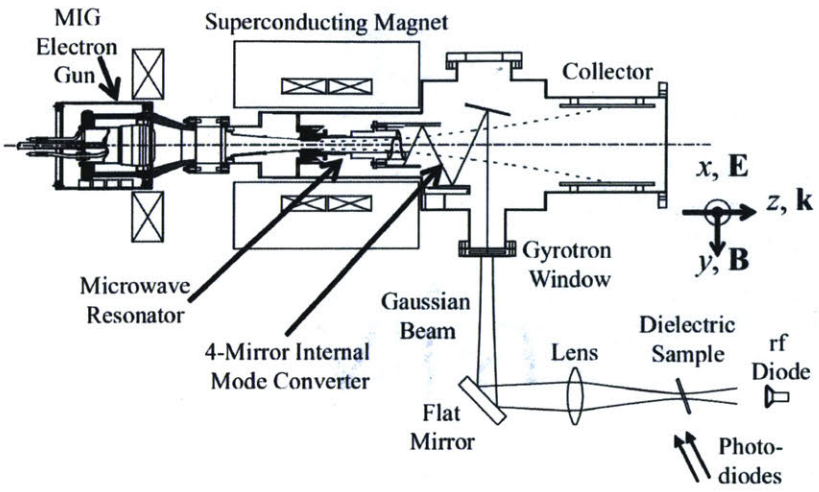

Figure 7-1: Schematic representative of the experimental setup of early experiments studying 110 GHz air breakdowns, reproduced from [1].

millimeter wave breakdown plasma at MIT. Sections 7.1 and 7.2 will provide an overview of work that was done prior to the work of this thesis. This overview focuses on studies of breakdowns in air, while some of the published research also include results in pure nitrogen, argon, or helium.

7.1 Air Breakdowns at 110 GHz: Initial Observations

In 2008, Y. Hidaka first published observations of a 110 GHz microwave discharge in air [1]. The setup of this experiment is shown in Fig. 7-1. An earlier version of the gyrotron discussed in chapter 2 served as the high power microwave source. This gyrotron was setup to produce 3 microsecond pulses of up to 1.5 MW of power at 110 GHz. A linearly polarized microwave beam, polarized in the z-axis of Fig. 7-1, was produced in air from the output window of the gyrotron. A lens was used to focus the Gaussian beam to a 4 mm spot size, allowing testing with peak RF electric fields greater than 6 MV/m. The dielectric sample in Fig. 7-1 was only used in some observations. It was removed to allow viewing of the plasma in a simple Gaussian

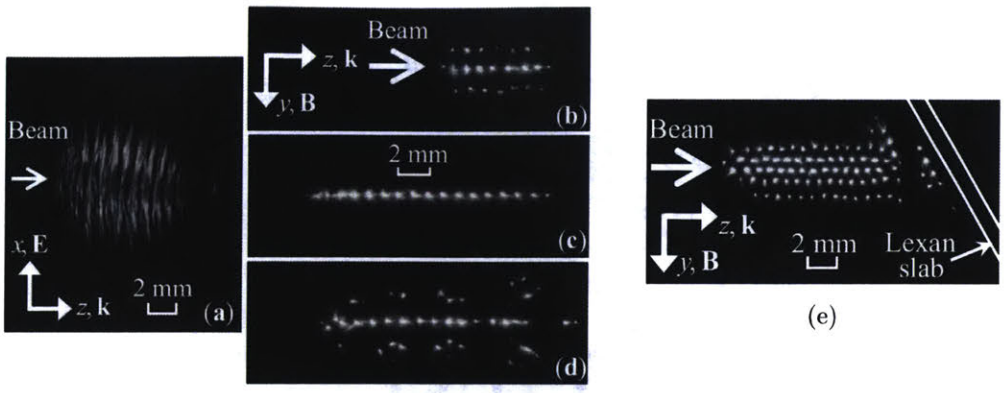

Figure 7-2: Visible light emission from 110 GHz breakdowns at 760 Torr, integrated over a 3 microsecond microwave pulse. In (e), a lexan dielectric slab was positioned in the microwave beam, to observe breakdown near a surface. This data is reproduced from [1].

beam geometry. Later experiments would add a pressure chamber and additional diagnostics, but used this same basic experimental setup.

Unique at the time of this experiment, the high output power of the gyrotron allowed for breakdown to be studied in atmospheric pressure air, with no initiators, such as fine wires, placed near the focus of the Gaussian beam. This was the first study of atmospheric pressure gas breakdown with millimeter waves in free space. The results were more interesting than anticipated.

Figure. 7-2 shows visible light images of the 110 GHz breakdown plasma at 760 Torr (1 atmosphere). Figure 7-2a is an "E-plane" image. The microwave beam is polarized parallel to the page. Subfigures b - e show "H-plane" images, where the microwave beam is polarized out of the page. The plasma was found to spontaneously form a two-dimensional array of plasma filaments. The filaments were elongated in the direction of the microwave electric field (subfigure a). The filaments were regularly spaced approximately a quarter wavelength apart ($\lambda = 2.72$ mm) in the plane perpendicular to the electric field.

It was hypothesized in [1] that the quarter wavelength spacing could be due to sequential formation of the filaments, propagating toward the microwave source. One filament forms near the microwave beam focus, reflecting microwaves upstream toward the microwave source. This creates interference peaks in the microwave field at

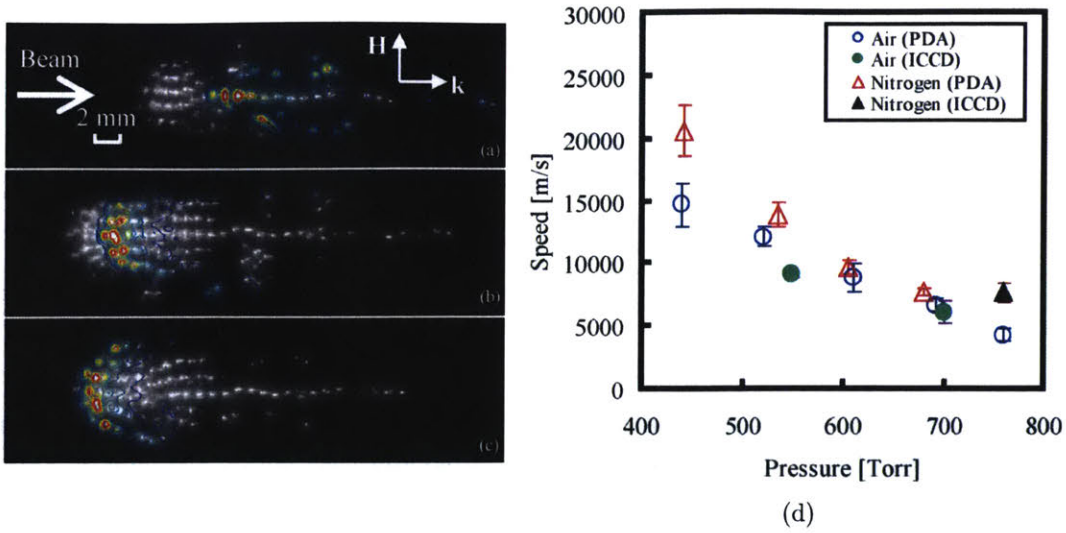

(d)

Figure 7-3: (a)-(c) Visible light emission from 110 GHz breakdowns at 710 Torr. The black and white images are integrated over a 3 microsecond microwave pulse. The color contours overlaid are from 49 ns exposures taken at (a) t = 400 ns, (b) 1.28 μs, and (c) 1.52 μs since the start of the microwave pulse. In (d), the propagation velocity of the plasma toward the microwave source is plotted as a function of pressure in air and nitrogen. The data labeled PDA is measured with a photodiode array. The data labeled ICCD is measured using images such as those in (a)-(c). This data is reproduced from [8].

distances of $\lambda/4$, $3\lambda/4$, $5\lambda/4$, etc., upstream of the first filament. It was suggested in this paper that, if successive filaments form quickly enough at the $\lambda/4$ position, it could preclude the formation of filaments with $\lambda/2$ spacing that one would naively predict from a constructive interference pattern.

The complex geometry of the observed plasma array was unexpected. That it arose from a geometrically simple system, a focused Gaussian beam in free space, made this plasma promising for testing models of plasma-microwave interaction. This gained the interest of a number of theory groups outside of MIT that produced numerical models of the plasma. Their work is summarized in section 7.3.

7.2 Subsequent Experimental Work

To support the ongoing theory efforts outside of MIT, additional experiments were carried out at MIT to further characterize the dynamics of a high power, 110 GHz

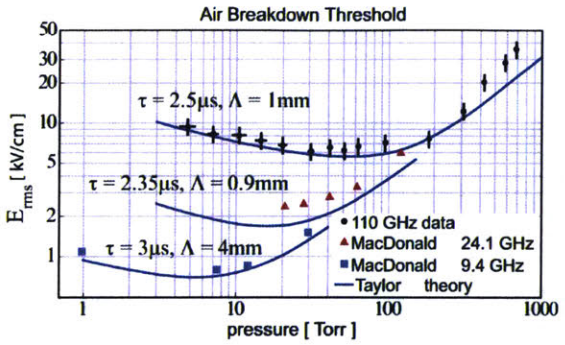

(a) Breakdown thresholds

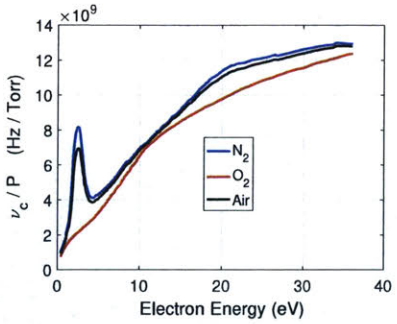

(b) Electron collision frequency

Figure 7-4: (a) RF Breakdown thresholds as a function of air pressure, reproduced from [9]. (b) Electron collision frequency in air, calculated from experimental data [10].

air breakdown. The first diagnostic added was a fast-framing intensified CCD imager (ICCD), capable of taking images as short as 2 ns. Figure 7-3 shows the first results of this diagnostic, from [8]. In the visible light images of Fig. 7-3a-c, a slow camera was used to integrate an image of the plasma over the 3 microsecond microwave pulse. This image is shown in black and white. Overlaid on this are false colored contours that correspond to light intensity captured with a 49 ns exposure. It can be seen that, at one instant, only a small portion of the plasma array exists. Figure 7-3d shows the measured propagation velocity of the plasma ionization front, measured as a function of background gas pressure.

In this experiment, there is a statistical uncertainty in the location and timing of the very first filament of the plasma array. Each 49 ns exposure required a separate microwave pulse. Similarly structured plasmas were manually selected from many recorded data points, to measure the plasma velocity. This shot-to-shot variation is the primary source of the uncertainty in the data points of Fig. 7-3d.

In [9], A. Cook documented the pressure dependence of the observed plasma structure. It was shown that, due to decreasing collisionality, the size of the filaments along the propagation direction of the microwave beam tended to expand and blur. Filamentary structure remained visible down to pressures as low as 40 Torr in air. Figure 7-4a shows the measured threshold electric field for initiating breakdowns as a func-

tion of background gas pressure. In the figure, the breakdown threshold values are well predicted by the theory of Taylor [111]. The theory curve, Eq. 7.1, is a phenomenological model that was developed to predict breakdown thresholds in lower frequency microwave breakdowns [111].

$$E_{threshold} = P\left(1+\omega^2/\nu_c^2\right)^{1/2} 3.75\left[(D_e/P\Lambda^2)+6.4\times10^4\right]^{3/16} \tag{7.1}$$

The constants in this equation are in cgs units, giving a resulting electric field in V/cm. In this model, P is the gas pressure in Torr, ω is the microwave angular frequency, and Λ is the spacing between parallel plates in cm. For a free space Gaussian beam, $\Lambda = \omega_0/\pi$ is used, where ω_0 is the spot size of the Gaussian beam [101]. D_e is the free diffusion coefficient for electrons. In air, the free diffusion coefficient for electrons is approximately $1.3\times10^6(\mathrm{cm^2s^{-1}Torr})/P$. The final remaining variable is the electron collision frequency, ν_c. For air, this is a complex function of electron energy, displayed in Fig. 7-4b. Historically, though, good agreement with experiments in air was found by taking $\nu_c = 5.3\times10^9(\mathrm{Hz/Torr})\times P$. Despite the discrete array nature of the 110 GHz breakdown, the model, Eq. 7.1, is in excellent agreement with the experimental data.

In [11], the use of a fast-framing ICCD to capture the dynamics of the plasma was expanded. Using similar techniques to [8], the propagation of the ionization front parallel to the microwave electric field was documented. The results with a linearly polarized microwave beam are shown in Fig. 7-5. The publication [11] also contains data on a plasma formed with a circularly polarized microwave beam, where discrete disks of plasma form, rather than filaments.

In Fig. 7-5(f), the lengths of several separate filaments are plotted over time. Each data series corresponds to a different filament. Peak propagation velocities for the ionization front of the plasma exceeded 100 km/s. The data in Fig. 7-5f is compared

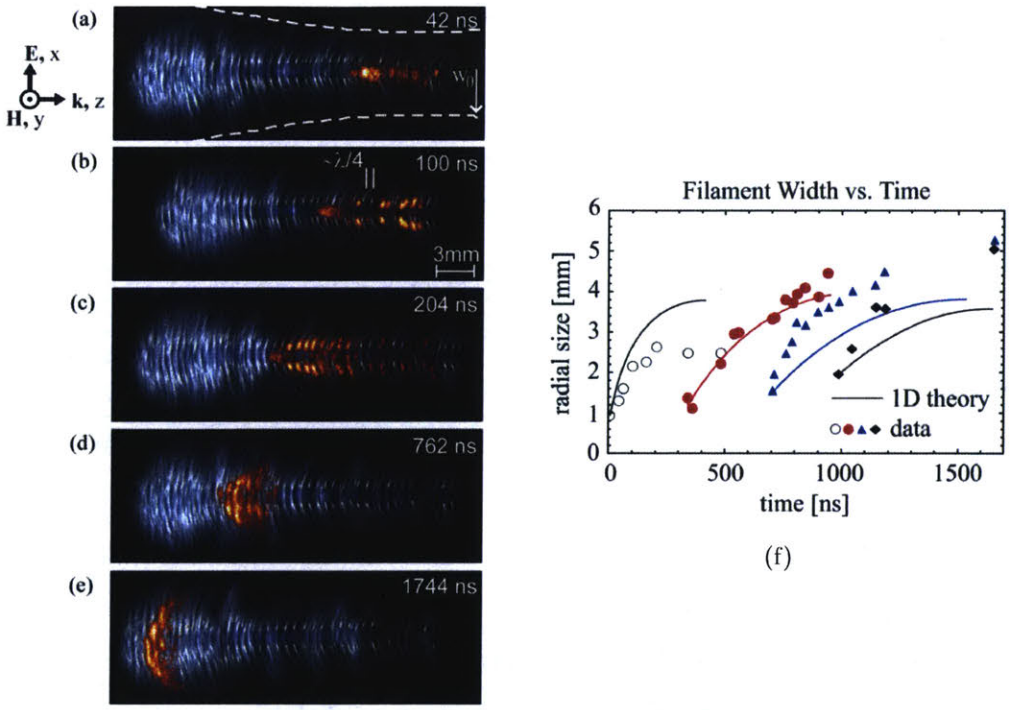

Figure 7-5: (a)-(e) Visible light emission from 110 GHz breakdowns at 760 Torr. The blue images are integrated over a 3 microsecond microwave pulse. The orange contours overlaid are from 10 ns exposures taken at successively later elapsed times, indicated on each image. In (f), the propagation ionization front along the electric field polarization direction is plotted. Each set of data traces the evolution of a different filament. This data is reproduced from [11].

to a simple one-dimensional theory, Eq. 7.2, from [15].

$$\text{ionization front velocity} = v = 2\sqrt{D_e \nu_i} \tag{7.2}$$

$$\frac{\partial n_e}{\partial t} = D_e \nabla^2 n_e + \nu_i n_e \tag{7.3}$$

Eq. 7.2 is a solution to the electron continuity equation, Eq. 7.3, including an ionization source and assuming a time independent diffusion coefficient and ionization rate. As in Eq. 7.1, D_e is the free electron diffusion coefficient at 760 Torr. For the theory lines in Fig. 7-5f, the net ionization rate, ν_i is approximated as

$$\nu_i = \nu_a \left[\left(\frac{E_{RF}}{E_c} \right)^{\beta} - 1 \right] \tag{7.4}$$

where $\nu_a = 5 \times 10^4 (Hz/Torr) \times P$ is the electron-neutral attachment rate in air at pressure P, E_{RF}/E_c is the ratio of the incident RF field amplitude to the threshold breakdown field, from Fig. 7-4a, and β is an empirically determined constant (β = 5.33 for air) [111]. The local electric field in the Gaussian beam varies as a function of radius and distance to the beam focus. This causes variation in the local ionization rates, leading to the curves in Fig. 7-5f.

In [112], RF diagnostics were used to map out the scattering of RF power from the plasma array. Averaged over the entire microwave pulse, the plasma was found to absorb as much as 45% of the incident RF power. Only 1% of the power was reflected back toward the microwave source. The majority of the RF power not absorbed is scattered in a broad cone approximately perpendicular to both the orientation of the plasma filaments, and the direction of the incoming microwaves.

In [12], graduate student J. Hummelt introduced the first plasma diagnostic to the experiment, using a high resolution spectrometer to extract a few physical parameters of the plasma. Figure 7-6 shows the results of this diagnostic. Spectroscopy was collected of the 353.7 nm, 357.7 nm, and 394.3 nm lines of molecular nitrogen present in the air breakdown plasma. The complex line shapes were fit using the commercial software SPECAIR to extract vibrational and rotational temperatures of the plasma at pressures from 1 to 100 Torr, and as a function of RF electric field strength.

The plasma was found to be far from thermal equilibrium. Vibrational temperatures of molecular nitrogen were found to range from 4200-6200 K, while rotational temperatures were 300-500 K. The rotational temperatures serve as a good proxy for the temperature of the background gas. The relaxation time of rotational energy to translational energy in molecular nitrogen is approximately 300 ns/Torr $\times$ P at 300 K background temperatures [113]. This is short compared to the 3 microsecond microwave pulse, indicating little gas heating in the brightest portions of the plasma.

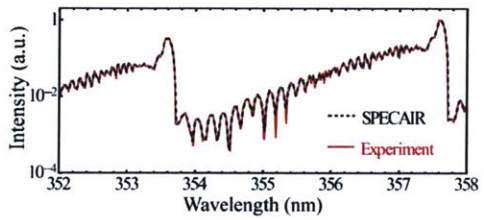

(a) Example emission spectrum at 30 Torr pressure of air

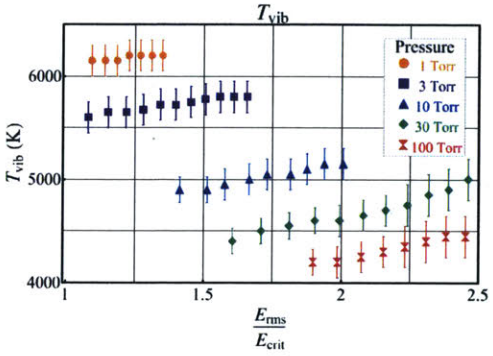

(b) Vibrational temperature measured from comparison of 353.7nm and 357.7nm nitrogen lines

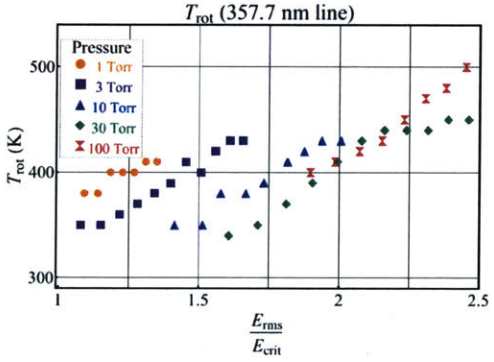

(c) Rotational temperature from fitting of the 357.7 nm nitrogen rotational bandhead of nitrogen.

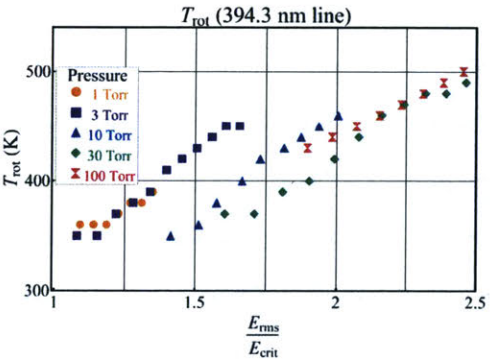

(d) Rotational temperature from fitting of the 394.3 nm rotational bandhead of nitrogen.

Figure 7-6: (a) Example fit to experimental spectroscopic data using SPECAIR. (b)-(d) are measured temperatures extracted from SPECAIR fits to emission features of nitrogen, as seen in (a). This data is reproduced from [12].

7.3 Air Breakdowns at 110 GHz: Theoretical Studies Performed Outside of MIT

The continued experimental characterization of a 110 GHz air breakdown plasma was motivated by the interest and work of a number of theory groups outside of MIT. The spontaneously complex plasma arising from a simple experimental geometry was a nearly ideal test case for numerical models of microwave-plasma interactions in weakly ionized plasmas. The efforts of these outside groups are summarized in this section.

7.3.1 A 1D Model by S. K. Nam and J. P. Verboncoeur

The first numerical theory came from the research group of J. P. Verboncoeur, then at UC Berkeley. In [114], a one-dimensional model was presented to explain the $\lambda/4$ spacing of the plasma filaments. The model consisted of 1D plasma fluid equations, with the RF electric field acting as a source of electron kinetic energy, and an assumed Maxwellian distribution of electron energy. The model employed, and was a test of, the group's earlier published numerical technique for calculation of the reflection, absorption, and transmission of the RF electric field in the nonuniform plasmas from [115]. For simplicity, this calculation used monatomic argon as the background gas, in lieu of an air mixture. The results of the one-dimensional model agreed with the hypothesis of the original experimental paper [1]. In the model, filaments form sequentially toward the microwave source. A new filament forms at a distance $\lambda/4$ upstream of the first plasma filament. The new filament reaches an electron density sufficient to absorb or reflect a large portion of the incident RF power, disrupting the interference pattern setup by reflection from the first filament. This process happens more quickly than electrons from the first filament can diffuse to the $(2n + 1)\lambda/4$ distances, where n is a positive integer. In addition to a qualitative explanation of the filament spacing, this model predicted peak electron densities of about 4.5×10^{23} m^{-3}.

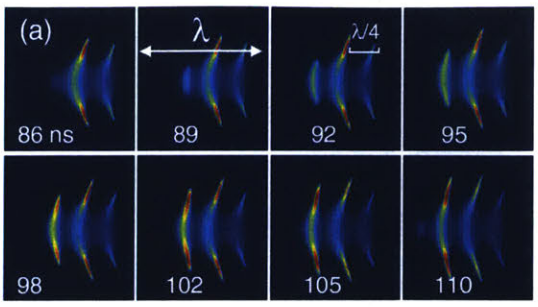

(a) Electron Density in E-plane

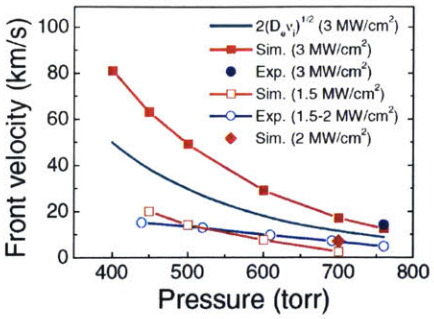

(b) Ionization Front Velocity

Figure 7-7: (a) Calculated E-plane view of plasma density as a function of time, from [13]. The electron density ranges from 0 (blue) to 3×10^{21} m^{-3} (red). The calculation was performed at atmospheric pressure (760 Torr) in air. (b) Comparison of plasma ionization front velocity calculated in [13] compared to experiments from [8].

7.3.2 A 2D Model by J. P. Boeuf, B. Chaudhury, and G. Q. Zhu

Through a series of papers, the group of J. P. Boeuf at the Laboratoire Plasma et Conversion d'Energie (LAPLACE) developed a two-dimensional finite-difference time-domain (FDTD) model of the air breakdown plasma [13–16]. The model numerically integrates Faraday's law, Eq. 7.5, and Ampere's law, Eq. 7.6, to calculate electromagnetic fields. An electron continuity equation, Eq. 7.7, and a simplified electron momentum transfer equation, Eq. 7.8, are integrated to calculate plasma parameters. The electromagnetic fields and the plasma are coupled through the current term: $\vec{J} = en_e\vec{v}_e$.

$$\nabla \times \vec{E} = -\mu_0 \frac{\partial \vec{H}}{\partial t} \tag{7.5}$$

$$\nabla \times \vec{H} = \varepsilon_0 \frac{\partial \vec{E}}{\partial t} + \vec{J} \tag{7.6}$$

$$\frac{\partial n_e}{\partial t} = D_{eff}\nabla^2 n_e + n_e\left(\nu_i - \nu_a\right) - r_{ei}n_e^2 \tag{7.7}$$

$$\frac{\partial \vec{v}_e}{\partial t} = -\frac{e\vec{E}}{m_e} - \nu_c\vec{v}_e \tag{7.8}$$

In these equations, $\vec{E}$ is the electric field, $\vec{H}$ is the magnetic field, μ_0 is the per-

meability of free space, ε_0 is the permittivity of free space, $\vec{J}$ is current, n_e is electron density, and $\vec{v}_e$ is electron velocity. The variables, ν_i, ν_a, r_{ei} are ionization frequency, electron-neutral attachment frequency, and electron-ion recombination rate. These three variables are obtained from the numerical Boltzmann equation solver BOLSIG+ [116]. This model makes use of an effective diffusion coefficient, Eq. 7.9, that is a balance between free diffusion, D_e, and ambipolar diffusion, D_a.

$$D_{eff} \approx \frac{\alpha D_e + D_a}{\alpha + 1} \text{ with } \alpha = \frac{\lambda_D^2 \nu_i}{D_e} \tag{7.9}$$

$$\lambda_D = \sqrt{\frac{\varepsilon_0 k T_e}{e^2 n_e}} \tag{7.10}$$

The length, λ_D, is the Debye length. The Boltzmann constant is k, T_e is electron temperature, and e is the charge of an electron. The integration time step was one RF cycle, averaging dynamics of the electron population of one RF period.

This two-dimensional model qualitatively reproduced the structure of the plasma filament array, seen in Fig. 7-7a. Additionally, the model was able to match the propagation velocity of the plasma ionization front toward the microwave source. This quantitative comparison is seen in Fig. 7-7b. This model predicted a peak electron density of about 3×10^{21} m^{-3}.

7.3.3 Major Differences Between the Two Models

The early model of Nam and Verboncoeur, [114], was published when only a single experimental paper had been written [1]. There are two important differences between this model and the later models by Boeuf et. al. First, for simplicity, [114] used Argon as the background gas. The second major difference is the use of an ambipolar diffusion coefficient for electron diffusion in the electron continuity equation, Eq. 7.7, versus the effective diffusion coefficient used by Boeuf et. al. The ambipolar coefficient of electron diffusion, D_a, is about 100 times smaller than the free diffusion coefficient, D_e. With ambipolar diffusion, the mobility of the electrons is reduced by space charge forces that maintain the quasi-neutrality of the plasma. The diffusing electrons

must drag heavy ions behind them. In general, use of the ambipolar coefficient is appropriate when a plasma is large compared to its Debye length, Eq. 7.10. Guessing realistic values for electron temperature, T_e, and electron density, n_e, each plasma filament is about one thousand Debye lengths in diameter.

The use of ambipolar diffusion was justified in the bulk of the plasma. However, at the edges of each filament, the plasma density (electron density) goes essentially to zero. Thus at the edges of the filaments, and between the plasma filaments, the effective diffusion coefficient, Eq. 7.9, is dominated by free diffusion of electrons. This difference between the earliest model of [114] and later models, [13–16], leads to a factor of 100 difference in predicted peak electron densities (4.5×10^{23} m^{-3} in [114] versus (3×10^{21} m^{-3} in [13]). The two models, though, essentially agreed on predictions of plasma ionization front velocity. This is because the propagation velocity is approximately given by $v = 2\sqrt{D\nu_i}$ where D is the diffusion coefficient. The much higher ionization frequency, ν_i, of argon (as compared to air) used in [114] compensated for the factor of 100 difference in diffusion coefficient between the two models.

7.3.4 Later Theoretical Work

In [17], Q. Zhou and Z. Dong reproduced the 2D numerical model of Boeuf et. al. and varied the input background gas pressure. This publication examined the predictions of the model at gas pressures from 100 to 760 Torr. The model was able to qualitatively reproduce the blurring of the filamentary structure seen experimentally in [9]. Additionally, this work produced predictions of peak electron density as a function of air pressure. These predictions are compared to experimental results from this thesis in section 8.1, Fig. 8-4b.

The model of Boeuf et. al. was modified to include and examine the effects of heating of the neutral background gas on a single plasma filament in [18]. This publication is discussed in detail and compared to experimental results from this thesis in section 8.2.5.

In [117, 118], V. E. Semenov et. al. developed a simplified one-dimensional model

of a high frequency microwave breakdown. Approximations included a constant and uniform diffusion coefficient, D, and attachment frequency, ν_a, and a constant ionization frequency, ν_i. This simple model was numerically integrated with very high time resolution, compared to the more sophisticated models thus far discussed. One major prediction of this work was that, above an RF electric field strength of $1.2E_c$, the threshold RF electric field, the plasma ionization front propagation velocity will increase linearly with RF electric field strength. The relatively long, 500 ns rise time of the microwave source described in chapter 2 has precluded testing of this prediction. At such high peak RF electric fields, plasma will tend to form and begin propagating during the rise time of the microwave pulse.

Chapter 8

Electron Density and Gas Density Measurements in a Millimeter Wave Breakdown

Though a number of experimental papers have been published, prior to this thesis on the 110 GHz air breakdown plasma, many physical parameters of the plasma remained unknown. This chapter presents thesis work on two plasma diagnostics. Peak plasma electron density and dynamic measurements of neutral gas density are reported.

8.0.1 Experimental Setup

The experimental setup for this work is shown in Fig. 8-1. A pulsed gyrotron (not shown in Fig. 1) was used to create a linearly polarized, quasi-optical beam. The gyrotron, as configured at the time of this experiment, could generate up to 1.4 MW of power at 110 GHz and up to 1 MW at 124.5 GHz [34]. Pulse lengths were 3 μs at 110 GHz and 2.2 μs at 124.5 GHz. In Fig. 8-1, microwaves propagate in the z direction, and are polarized out of the page, in the y direction. Mirrors guide the microwave beam from the gyrotron window into a gas chamber. Inside the chamber, a high density polyethylene lens was used to focus the beam to a small spot size, 3.2 mm and 2.6 mm 1/e radius in RF electric field at 110 and 124.5 GHz, respectively.

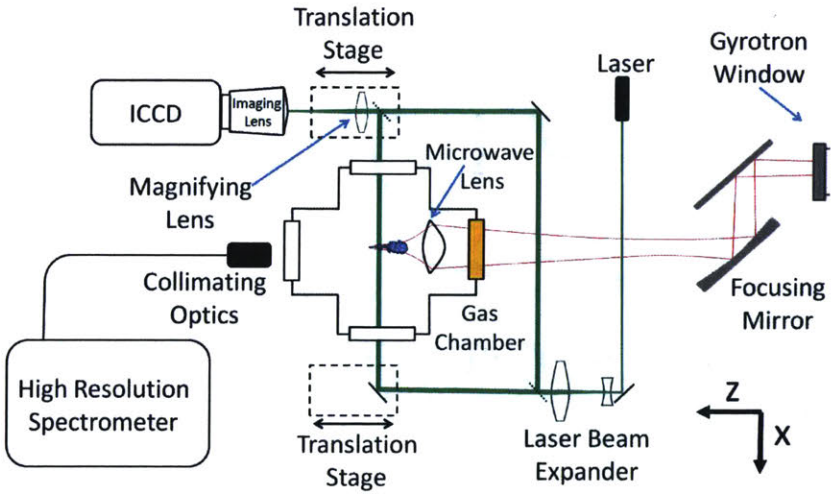

Figure 8-1: Schematic of the experiment for study of a Microwave Breakdown.

Air pressure in the chamber and input microwave power were varied as necessary for the experiments.

8.0.2 Millimeter-Wave Discharge Plasma

Example microwave discharges in 750 Torr air are shown in Fig. 8-2. The example discharges were created with 750 kW, 2.2 μs pulses of linearly polarized 124.5 GHz microwaves (wavelength = 2.4 mm). Microwaves were incident from the right of each image. The polarization of the incident microwaves was rotated by 90° between Figs. 8-2a and 8-2b. For these images, light was collected with 3 μs exposures, capturing light from the entire lifetime of the discharge plasma.

As seen in chapter 7, the plasma spontaneously forms a two-dimensional filamentary structure with filaments oriented along the electric field of the polarized incident microwaves. The plasma array is a dynamic formation. An initial plasma filament forms near the focal point of the incoming microwave beam. This initial filament reflects and absorbs much of the incoming microwaves. Reflected microwaves interfere with incoming microwaves to produce hot spots in the RF electric field toward the microwave source. A subsequent filament then forms at the hot spot. In this manner, the plasma array propagates upstream toward the source. The original filament and

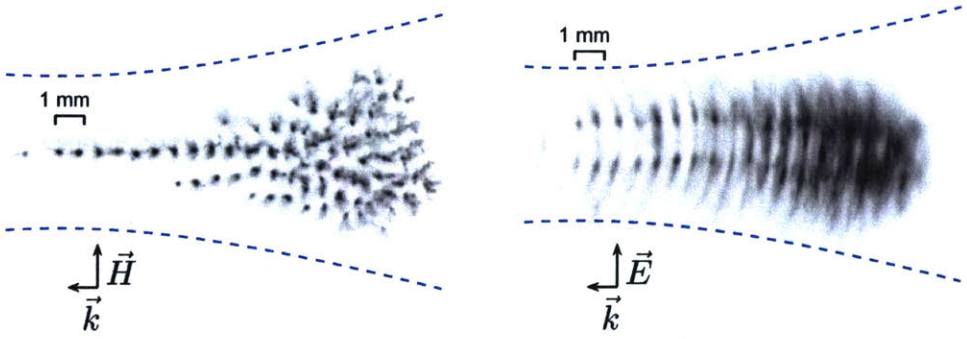

(a) H-plane (b) E-plane

Figure 8-2: Monochrome visible light images of a plasma discharge initiated by a focused 750 kW, 124.5 GHz microwave pulse in 750 Torr air. 3 μs exposures were used to gather all visible light from discharges created with 2.2 μs microwave pulses. These are negative images. The darkest regions correlate with the strongest light emission. The polarization of the microwave beam was rotated 90° between a) and b). The dashed lines denote the $1/e$ power contour of the incident Gaussian beam.

subsequent filaments spread along the electric field lines over time scales of nanoseconds. Several filaments can coexists at a single time. Filaments closer to the source absorb and scatter a large fraction of the incoming microwaves away from the axis of the incident Gaussian beam. In Fig. 8-2b, this causes a shadow to form in the plasma along the axis of the Gaussian beam. Visible light emission from the plasma is strongest about $\lambda/4$ above and below the axis, where the plasma persists longer.

8.1 Electron Density Measurement

8.1.1 Optical Emission Spectroscopy, H_α Line Broadening

Peak electron density was measured using optical emission spectroscopy. A high resolution spectrometer was combined with an ICCD camera as a visible light detector. Electron density was measured from the Stark broadening of the $n = 3$ to $n = 2$ transition of hydrogen, the H_α line at 656.3 nm. The subscript α indicates that this is the first line (lowest energy) of the Balmer series of hydrogen lines.

Dry air was bubbled through deionized water to introduce humidity. Hydrogen

was present in the form of small amounts of dissociated water vapor. Like collisions between hydrogen atoms were neglected as a broadening mechanism, because of the low concentration of hydrogen present in the experiment. Background spectra were collected by creating discharges in dry air. These discharges lacked any measurable hydrogen lines.

Broadening mechanisms for the H_β line at 486.1 nm have been derived in detail for use as a diagnostic of plasma electron density [119,120]. In the presented experiment, the H_β line is obscured by strong emission from molecular nitrogen. Use of other lines of the hydrogen Balmer series for Stark broadening measurements has been explored in the literature [121]. The H_α line was chosen for its strong signal-to-noise ratio. Equations 8.1-8.5 were adapted for use with the H_α line following the derivation in [119]. In these equations, T is neutral gas temperature in Kelvin, P is neutral gas pressure in Torr, and n_e is electron density in units of m^{-3}. Neutral gas temperature was estimated from [12] to be 400 ± 100 K. This did not significantly contribute to the uncertainty in the final values of n_e.

$$\Gamma_{Stark} = A n_e^{\gamma} \tag{8.1}$$
$$A = (1.65 \pm 0.16) \times 10^{-14} \text{ nm};$$
$$\gamma = 0.583 \pm 0.002$$

$$\Gamma_{VdW} = 1.1 P T^{-0.7} \text{ nm} \tag{8.2}$$

$$\sigma_{instr} = 1.65 \times 10^{-2} \text{ nm} \tag{8.3}$$

$$\sigma_{nat} = 6.51 \times 10^{-5} \text{ nm} \tag{8.4}$$

$$\sigma_{Dop} = 2.34 \times 10^{-4} T^{0.5} \text{ nm} \tag{8.5}$$

Eqs. 8.1-8.5 are for the half-width at half-maximum of a broadened peak. A σ symbol indicates a Gaussian broadening mechanism. A Γ indicates a Lorentzian broadening mechanism. Experimental data were fit with Voigt profiles, convolutions of Gaussian and Lorentzian profiles. The relationship between Stark broadening of

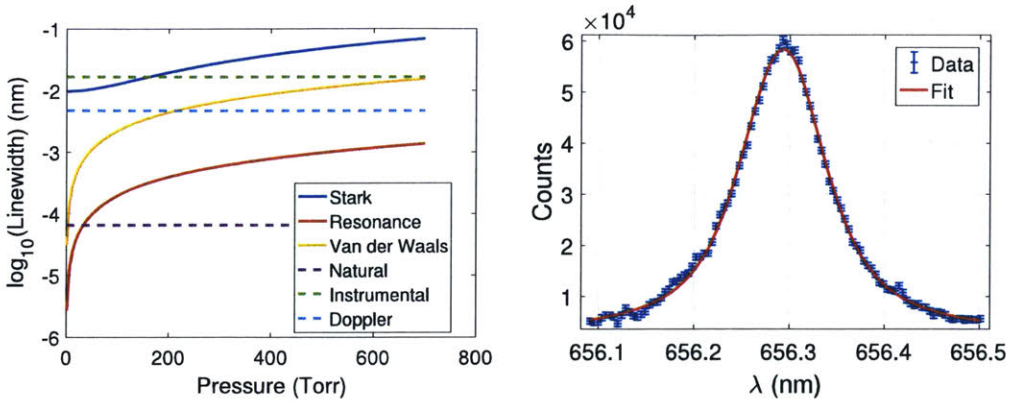

(a) Broadening of the H_α Line (b) Voigt Profile Fit to Experimental Data

Figure 8-3: a) Broadening mechanisms, eqs. 8.1 - 8.5, calculated for the H_α line at 400 K. b) Example fit of a recorded H_α line with a Voigt profile. The example data was collected at $P = 300$ Torr with a normalized electric field of $E/E_{crit} = 3$.

the H_α line and electron density, Eq. 8.1, was derived from a fit to numerically modeled data [122]. A and γ are fit parameters. The uncertainty in these parameters was the primary source of uncertainty in the final results.

Instrumental broadening, σ_{instr}, Eq. 8.3, is a measured parameter of our spectrometer and ICCD setup. Natural broadening, σ_{nat}, Eq. 8.4, was calculating using published atomic transition probabilities [123]. Doppler broadening, σ_{Dop}, Eq. 8.5, was adapted from the H_β equation in [119] with a multiplicative factor of $\lambda_{H\alpha}/\lambda_{H\beta}$, where λ indicates the central wavelength of the broadened spectral line. Van der Waals broadening, Γ_{VdW}, broadening due to collisions with unlike particles, Eq. 8.2, was calculated using the relative intensities of the seven transitions that make up the H_α line [124].

A plot of the broadening mechanisms as a function of pressure can be seen in Fig. 8-3a. In this plot, the gas temperature was assumed to be 400 K. For Stark broadening, the electron density was assumed to be equal to the critical density, Eq. 8.6.

$$n_c = \frac{m_e c_0}{e^2}\left(\omega^2 + \nu_c^2\right) \tag{8.6}$$

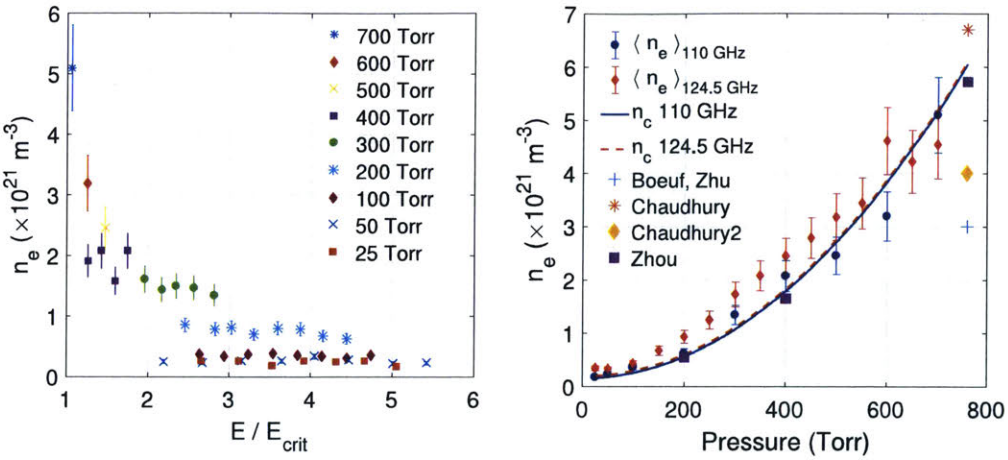

(a) Electron Density versus RF Electric Field (b) Electron Density versus Air Pressure

Figure 8-4: (a) Electron density, n_e vs E/E_{crit}. E_{crit} is the threshold RF electric field for initiating breakdown in air in free space. (b) Electron density, n_e, closely follows the pressure dependence of the critical density for reflection of incoming microwaves, Eq. 8.6. The referenced theoretical data points come from: Boeuf [14], Zhu [15], Chaudhury [13], Chaudhury2 [16], Zhou [17].

$$f_{pe} = \frac{\omega_{pe}}{2\pi} = \frac{1}{2\pi}\sqrt{\frac{n_e e^2}{m_e \varepsilon_0} - \nu_c^2} \tag{8.7}$$

$$\nu_c = \left(5.3 \times 10^9 \frac{\text{Hz}}{\text{Torr}}\right) P \tag{8.8}$$

The critical density is defined as the density at which the plasma frequency, f_{pe}, is equal to the frequency of the incoming microwaves. Plasma frequency due to free electrons in a collisional plasma is given in Eq. 8.7. The pressure dependence arises from the collision frequency, ν_c, of electrons with neutrals in air, estimated using the simple relation in Eq. 8.8. The variables m_e, e, and ε_0 are the mass of the electron, the charge of the electron, and the permittivity of free space, respectively. In Eq. 8.6, ω is the angular frequency of the incident microwaves. An example fit to experimental data is shown in Fig. 8-3b.

Pressure (Torr)	E_{crit} (MV/m)
20	0.97
30	0.87
40	0.93
50	0.89
60	0.95
100	1.01
200	1.09
300	1.72
450	2.87
600	4.02
700	5.08

Table 8.1: Threshold values of RF electric field for initiating breakdown, compiled from [9].

8.1.2 Electron Density Results

In Fig. 8-4a, the peak electron density was measured as the power of the incoming microwaves was varied. This data was collected at 110 GHz. The x-axis in this figure is the peak electric field of incident waves relative to the critical field for initiating breakdown, E_{crit}, which has been measured for 110 GHz microwaves [9]. Experimental values of E_{crit} are shown in Table 8.1 for reference. The table shows peak values of RF electric field at the focal point of the microwave beam. These are greater than the RMS values reported by Cook et. al., [9], by a factor of $\sqrt{2}$.

At $P = 200$ and 300 Torr, measured electron density is shown to slightly decrease as incoming microwave power is increased. The spectroscopic measurement was performed by collecting light from the entire plasma array. As microwave power is increased, the plasma becomes much larger, extending more into low electric field regions of the Gaussian beam. The collection of the signal from the entire plasma is likely the cause of this trend of decreasing n_e versus E/E_{crit}.

Figure 8-4b shows how the peak electron density varies with pressure for both 110 and 124.5 GHz microwaves. Data was collected at the highest values of E/E_{crit} for each pressure shown in Fig. 8-4a, to maximize the strength of the signal measured. For both frequencies, the electron density is well represented by the critical density,

n_c, given by Eq. 8.6. In Fig. 8-4b, measured electron density is compared with the values of peak electron density predicted by several numerical models [13–16]. Most of these models predict peak electron density only for $P = 760$ Torr and are in reasonable agreement with the experiment. The two-dimensional model by Zhou et. al., [17], predicts values of electron density at pressures from $P = 200$ to 760 Torr, and shows good agreement with the experiment.

8.2 Gas Density Measurements

8.2.1 Two-Dimensional Visible Laser Interferometry

The temperature (and density) of the neutral gas is a fundamental property of weakly ionized plasmas. Recently, a numerical model of gas heating has been produced by Kourtzanidis et. al., [18], that recreates many of our experimental parameters at 110 GHz and atmospheric pressure. Experimental measurements of neutral gas density as a function of time and space have been performed to allow for comparison with this model.

Gas density was measured using a two-dimensional visible light laser interferometer. Laser interferometry is an established method to measure gas temperature in low frequency microwave discharges [125–129]. Two wavelengths of light, 532 and 635 nm, were used to separate phase shift due to free electrons from phase shift due to heated neutral gas. A Mach-Zehnder interferometer was constructed around the discharge plasma, as shown in Fig. 8-1. Diode laser beams were expanded to 1 cm in diameter in order to image a large portion of the discharge. Movable optical elements were used to sweep the measurement arm of the interferometer across the array of plasma filaments. An imaging lens focused on the location of the discharge was necessary to counter refraction of the laser light due to the heated gas. A magnifying lens was employed to enhance spatial resolution of the plasma array.

One mirror of the interferometer was tilted to produce a pattern of interference fringes on the ICCD detector. A microwave discharge in the measurement arm of the

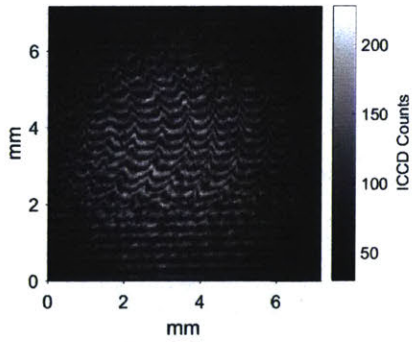

(a) Raw Interferogram

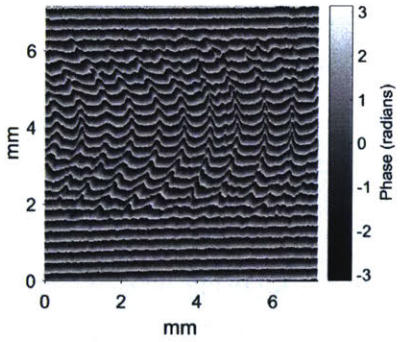

(b) Phase Shift with 2π Uncertainty

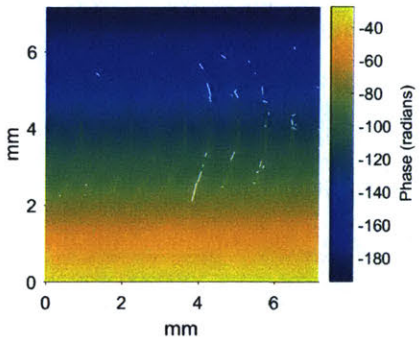

(c) Unwrapped Phase Shift

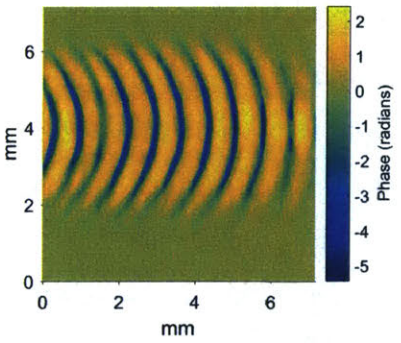

(d) Phase Shift with Background Subtracted

Figure 8-5: An example of raw and processed interferograms, gathered at $P = 750$ Torr. (a) is a raw ICCD image of the interference pattern imprinted on the output laser of the interferometer. In (b) a 2D Morelet continuous wave transform was used to filter out high and low spatial frequencies from the raw data, returning phase shift within a range of $-pi$ to pi. In (c) the phase has been unwrapped. In (d) the phase shift due to the tilted mirror has been subtracted, leaving only phase shift due to the plasma.

interferometer caused the interference fringes to bend away from their plasma-free positions. An example of this can be seen in Fig. 8-5a. In the absence of a plasma, the interference pattern would be a series of horizontal fringes. Intense, localized gas heating yielded complex interferograms with sharp features. Phase shift was extracted from interferograms using two-dimensional continuous wavelet transforms [130, 131], as opposed to the more common FFT techniques used to analyze less complex interferograms. The two-dimensional wavelet transform functioned as a filter, eliminating high and low spatial frequencies from the data. An example of filtered data is shown in Fig. 8-5b. The darkest values were set to phase shift $-\pi$ and the brightest values were set to $+\pi$. Phase between the two extremes is linearly proportional to the brightness of the filtered data. Phase unwrapping was performed using IDEA interferometry software [132], making using of the two dimensional phase unwrapping method in [133]. An example of experimental data with unwrapped phase is shown in Fig. 8-5c. The large vertical gradient in phase is due to the intentionally tilted mirror in the interferometer. The white lines in subfigure (c) are "branch cuts": discontinuities in the unwrapped phase. The location of the branch cuts was a random product of the sharp features in subfigure (a), that approached the scale of the ICCD pixels. The background phase due to the tilted mirror is subtracted from the data in Fig. 8-5d, leaving only the phase shift due to the plasma. This final image has been averaged over 25 separate pulses. This was done to remove the branch cuts, that occur in random locations in each recorded interferogram.

Microwave discharges studied with the interferometer were created with 750 kW, 2.2 μs pulses of 124.5 GHz microwaves. After transmission losses, this created a peak electric field of 6.3 MV/m at the focal point, 1.1 times the critical field for initiating breakdown at 750 Torr.

Line integrated gas density is calculated from measured phase shift using Eq. 8.9.

$$\Delta\phi = \frac{2\pi R_G}{\lambda_{probe}} \int (\rho - \rho_0)\, dl \tag{8.9}$$

The neutral gas number density is ρ, with the background value given by ρ_0. R_G

is the Gladstone-Dale constant, with units of one over density. The value of the Gladstone-Dale constant depends upon gas composition, and has been tabulated for common gases [134]. This constant relates gas density to refractive index at a given wavelength of light.

8.2.2 Plasma Array Dynamics

Figs. 8-6 - 8-8 show the time progression of visible light emission and gas heating due to the microwave discharge at air pressures of 150, 450, and 750 Torr. The microwave beam is incident from the right. Data shown here were collected viewing the E-plane of the microwave discharge, as in Fig. 8-2b. The visible light images of the plasma are 10 ns exposures, as opposed to the 3 μs exposures seen in Fig. 8-2. The interferometric data was gathered using 10 ns exposures averaged over 25 discharges, to increase signal to noise. The movable optics of the interferometer were swept horizontally, and multiple images were stitched together to show a greater extent of the plasma array.

For the interferometry experiments, the location and timing of the plasma filaments was made highly reproducible by the inclusion of a needle point initiator downstream from the focus of the microwave beam. In Figs. 8-6 - 8-8, the tip of the initiator is at 1 mm along the horizontal axis. The focal point of the microwave beam is at 7 mm. The existence of plasma along the horizontal axis to the left of the microwave beam focal point is due to the needlepoint initiator. This plasma formed on the needlepoint during the rise time of the microwave pulse. It provided seed electrons that caused an initial plasma filament to form consistently at a given time to within ± 2 ns. To the right of the focal point, the structure of the plasma array was the same as observed without the initiator, but the timing and the position were much more consistent.

Arrows at 120 ns in Fig. 8-7 and 100 ns in Fig. 8-8 indicate the filaments that were further analyzed to obtain local values of gas density, presented in the following subsections. The time scales in these figures are set so that 0 ns occurs when visible light is first detected at the location of the example plasma filaments. The time scale

for $P = 150$ Torr data in Fig. 8-6 is set so that 0 ns occurs when visible plasma first forms at the focal point of the microwave beam.

At the locations where visible plasma is seen in Figs. 8-6 - 8-8, gas density cavities formed. At $P = 150$ Torr in Fig. 8-6, filamentary structure is faintly observable in the visible light time sequence. At 1300 ns, gas heating is shown to greatly diminish neutral gas density where the tips of plasma filaments previously existed, while showing much weaker heating along the axis of the Gaussian beam. The filamentary structure of the visible plasma is increasingly clear at higher pressure in Figs. 8-7 and 8-8.

8.2.3 Single-Filament Local Gas Density

For air pressures of $P = 450$ and 750 Torr, high collisionality caused heated gas to form an orderly array of filaments much like that seen in visible light emission from the plasma. The assumption that, for thin slices perpendicular to the filaments, the cross sections have cylindrical symmetry allowed the extraction of local gas density from the line integrated data of Figs. 8-7 and 8-8. This was made possible, because the one-dimensional portion of the plasma array, seen in the left half of Fig. 8-2a, allowed the signal from a single filament to be isolated.

For cylindrically symmetric systems, line integrated gas density is related to the profile of local gas density by the Abel transform, Eq. 8.10. A density wave of compressed gas formed around each heated plasma filament. This yielded a non-monotonic profile in $\Delta\rho$ versus r, gas density versus radius of each filament, rendering many common methods of inverting the Abel transform unusable. An iterative method for computing the inverse Abel transform was chosen to invert the non-monotonic gas density profiles [135].

$$\langle \Delta\rho L \rangle (x) = 2 \int_x^\infty dr\, \rho(r) \frac{r}{\sqrt{r^2 - x^2}} \tag{8.10}$$

The coordinate system used to analyze local gas density is illustrated in Fig. 8-9. Distance along an electric field line is denoted by s, and distance perpendicular to a

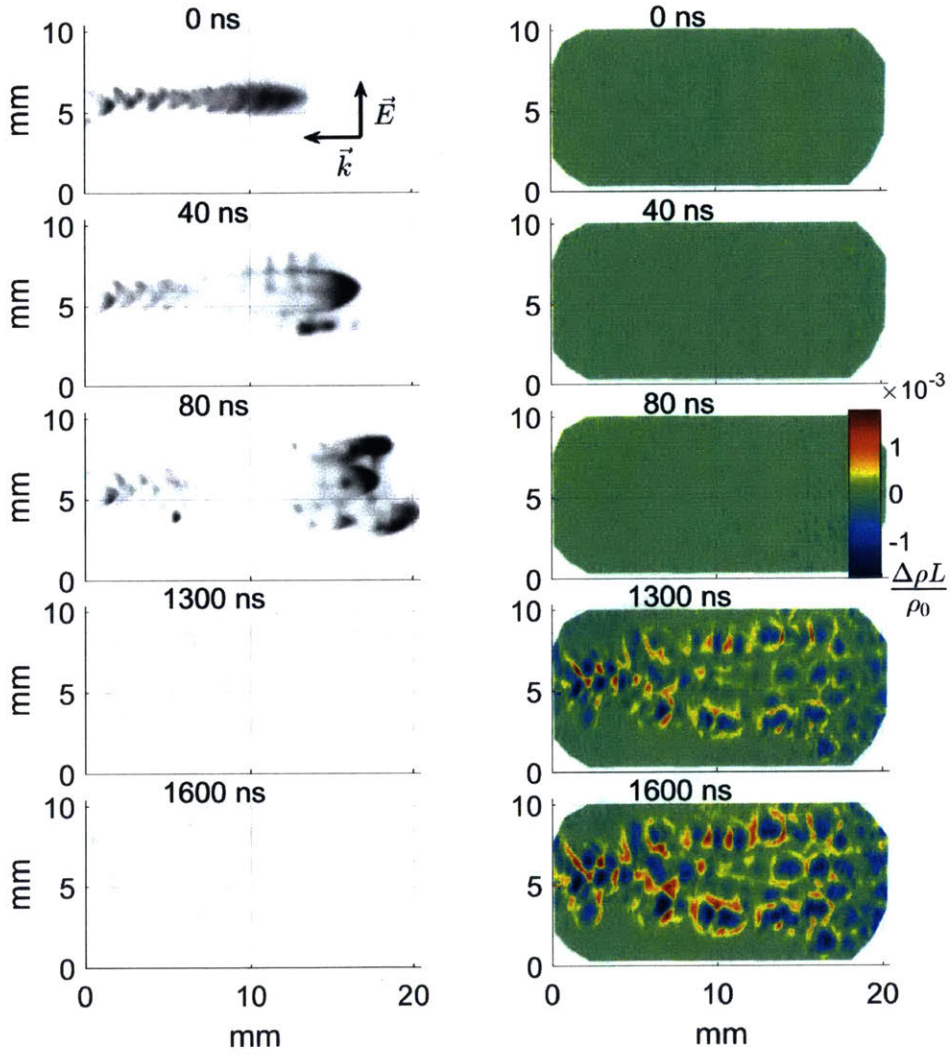

(a) Visible Light

(b) Line Integrated Gas Density

Figure 8-6: Time evolution of visible light emission and gas heating at $P = 150$ Torr. Line integrated gas density is in units of m.

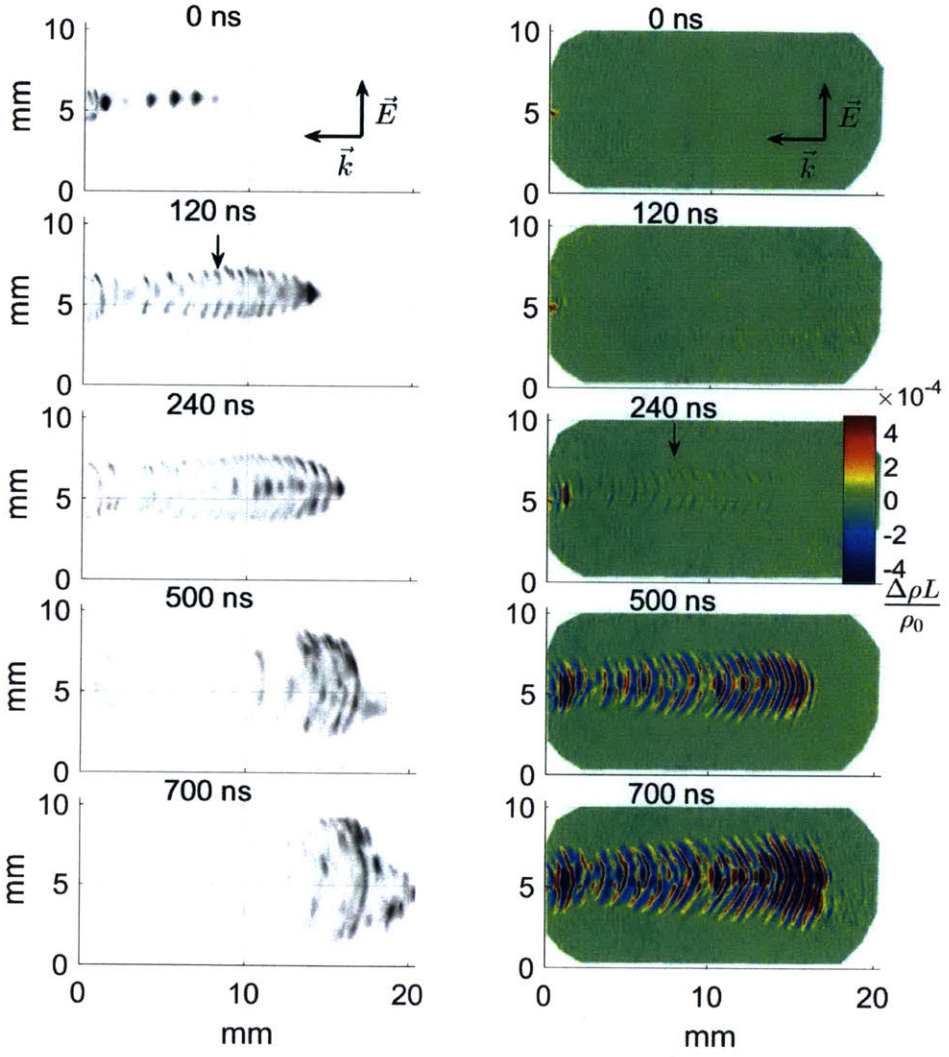

(a) Visible Light

(b) Line Integrated Gas Density

Figure 8-7: Time evolution of visible light emission and gas heating at $P = 450$ Torr. A black arrow indicates the location of the filament that was further analyzed to generate the local gas density data in Figs. 8-10a and 8-11. Line integrated gas density is in units of m.

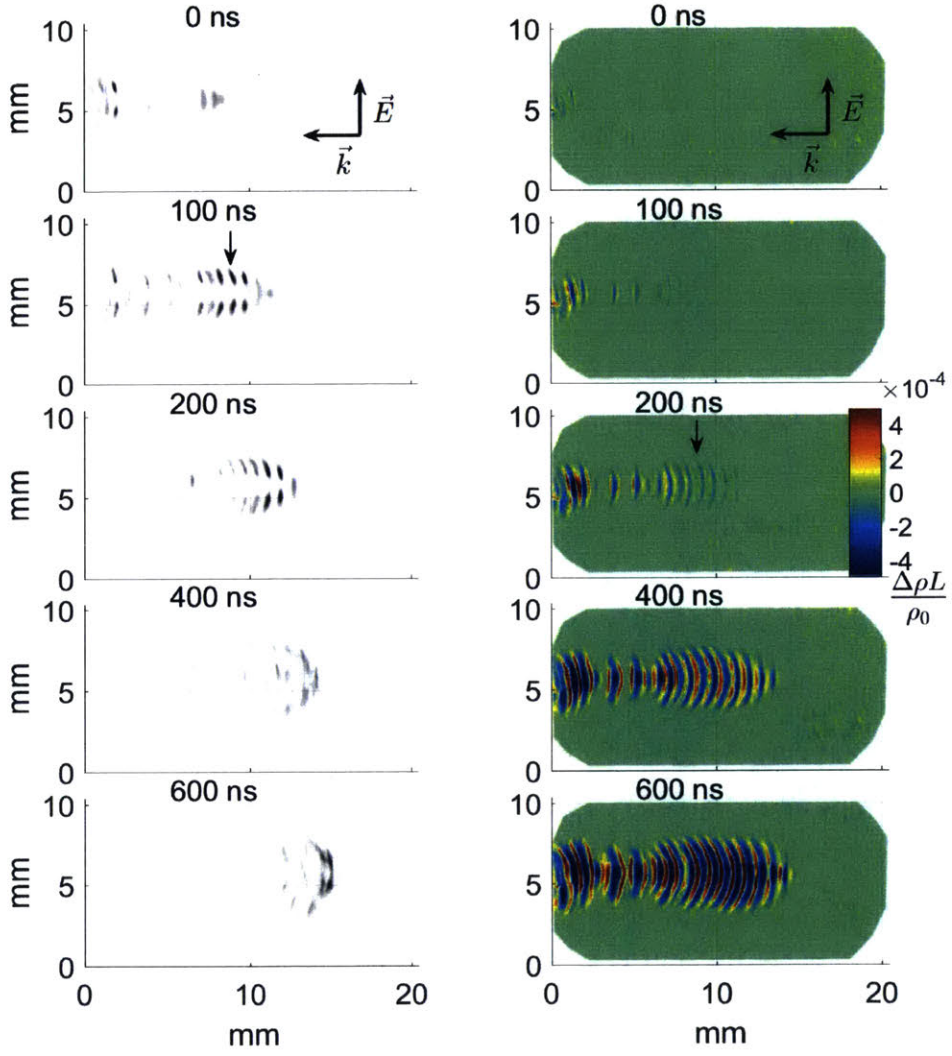

(a) Visible Light

(b) Line Integrated Gas Density

Figure 8-8: Time evolution of visible light emission and gas heating at $P = 750$ Torr. A black arrow indicates the location of the filament that was further analyzed to generate the local gas density data in Figs. 8-10b, 8-12, and 8-13. Line integrated gas density is in units of m.

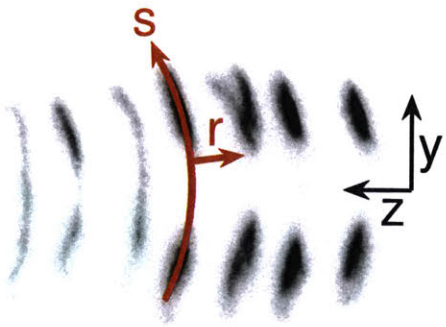

Figure 8-9: Coordinate system used for displaying local gas density values. Distance along RF electric field lines is s. Distance perpendicular to field lines is r. Cylindrical symmetry is assumed for thin slices perpendicular to the curved centerline. The lab coordinates z and y are as defined in Fig. 8-1.

field line is denoted by r. A curved centerline was fit to each filament analyzed. A radial profile was fit to a slice of the filaments every 16 μm along each centerline, the spatial resolution of our detector.

Analysis at early times was limited by detector sensitivity, which scales linearly with pressure. Analysis at late times was limited by expansion of heated filaments into neighboring filaments. Once the outgoing density waves begin to collide, our assumption of cylindrical symmetry in the curved coordinate system fails. For this reason, analysis of local data was stopped at 280 ns for $P = 450$ Torr and at 200 ns for $P = 750$ Torr.

Contour plots of the results for $P = 450$ and 750 Torr are displayed in Fig. 8-10. Comparing Fig. 8-10a and b, it is observed that the gas density profiles of the filaments are pressure dependent. As pressure is decreased, gas heating is increasingly concentrated in the tips of each filament. This can also be seen in Figs. 8-6 - 8-8.

8.2.4 Local Results at $P = 450$ Torr

Local gas density along the filament axis at $P = 450$ Torr is illustrated in greater detail in Fig. 8-11. This plot shows the variation of gas density along the centerline of the filament, at $r = 0$. It can be seen that gas heating is most intense near the tips of the filament (large values of $|s|$), reaching density reductions greater than 80%

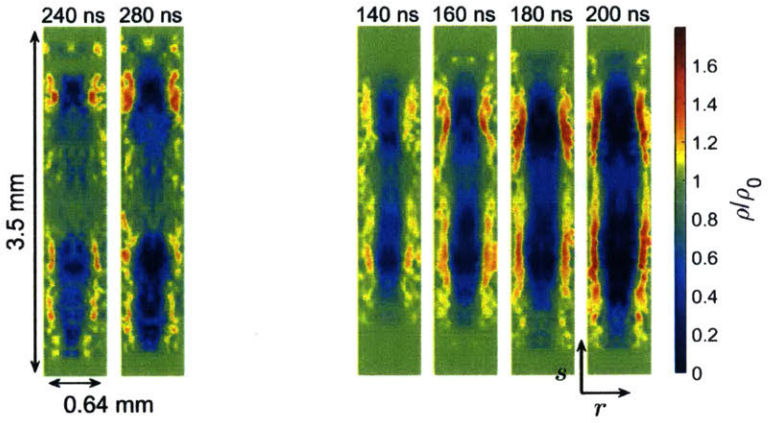

(a) 450 Torr (b) 750 Torr

Figure 8-10: Local values of neutral gas density extracted from line integrated data. These are displayed using the coordinate system defined in Fig. 8-9.

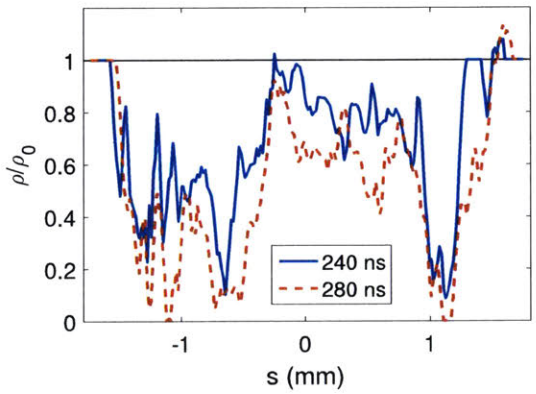

Figure 8-11: Variation of neutral gas density, ρ, along the centerline ($r = 0$) of a filament at $P = 450$ Torr. Variables r and s are defined in Fig. 8-9.

depletion of background gas.

8.2.5 Local Results at $P = 750$ Torr

Local gas density values for $P = 750$ Torr are compared to numerical results from Kourtzanidis et. al., [18], where a two-dimensional planar simulation of a single, non-propagating filament was created by 110 GHz plane waves coming from both positive and negative z in 760 Torr air, in Figs. 8-12 and 8-13. Each plane wave had an

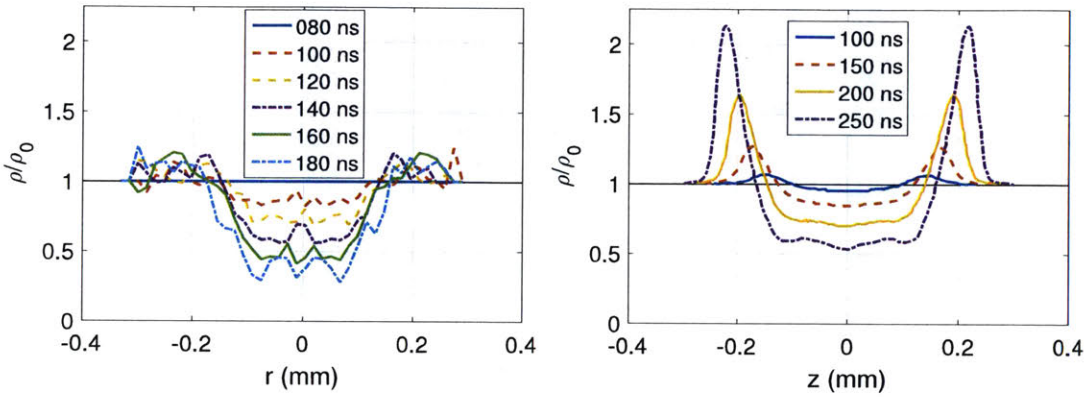

(a) 750 Torr Experimental Data (b) 760 Torr Numerical Model [18]

Figure 8-12: Radial dependence of neutral gas density, ρ, across the center of a filament ($s = 0$) at $P = 750$ Torr. a) Experimental results extracted from line integrated data shown in Fig. 8-8b. b) Numerical model from Kourtzanidis et al. [18]. The coordinates r and s are defined in Fig. 8-9. The variable z is distance parallel to the propagation of the microwaves in the 2D numerical model.

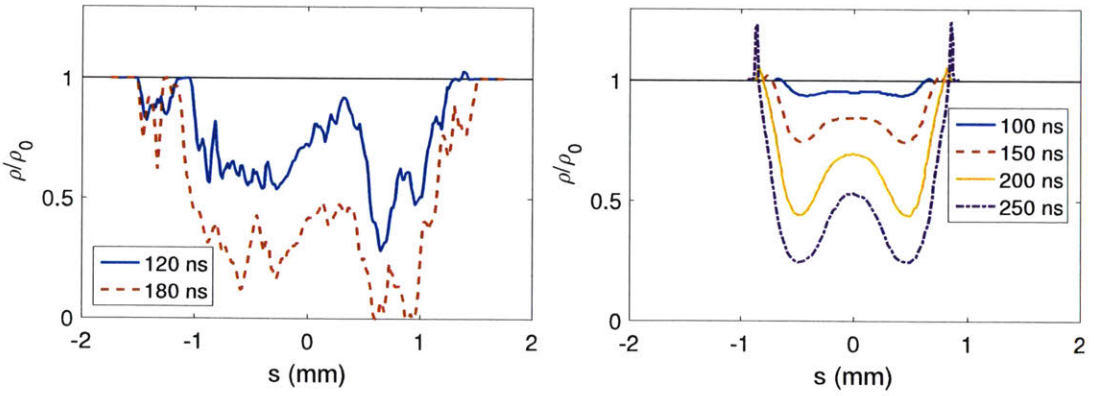

(a) 750 Torr Experimental Data (b) 760 Torr Numerical Model [18]

Figure 8-13: Variation of neutral gas density ρ along the centerline, ($r = 0$), of a filament at $P = 750$ Torr. a) Experimental results extracted from line integrated data shown in Fig. 8-8b. b) Numerical model from Kourtzanidis et. al. [18]. Variables r and s are defined in Fig. 8-9.

amplitude of 2.5 MV/m, giving a maximum total electric field of 5 MV/m at the location of the plasma filament.

The experimental results in this section were collected with 124.5 GHz microwaves, with a wavelength that is 13% smaller than that in the simulation. To avoid assumptions about the scaling of plasma structures with wavelength, the experimental results were not rescaled for comparison with the simulations. This small change in dimensions is insignificant when comparing the overall structure and time scales of the plasma.

The radial dependence of gas density at $s = 0$ is compared with the numerical simulation in Fig. 8-12. The time scale of the experimental data is in agreement with that of the simulation. Gas heating only leads to significant changes in gas density 100 ns after visible plasma is formed. The simulation also correctly predicts the existence of outward moving density waves. However, Kourtzanidis et. al. predict higher amplitude density waves than are observed in our experiments. This is due to the two-dimensional planar geometry of their simulation. Conservation of mass in the approximately cylindrical geometry of the experiment leads to smaller values of $|\Delta\rho|$ at increasing $|r|$ in Fig 8-12a.

Figure 8-13 compares the experiment with the numerical simulation along the centerline of the filament. As predicted in the simulation, on-axis heating is peaked at the tips of the filament, though heating at the filament tips is seen to be stronger in the experiment. Discrepancies in the length of the filament along s is explainable by the rapid propagation of the experimental plasma. The simulated plasma of Kourtzanidis et. al. is limited in overall length in the s direction to approximately $\lambda/2$ by interaction between the plasma and heated neutral gas. This gas heating, however, takes 100 ns to turn on. In the presented experiment, the discharge plasma propagates toward the microwave source on time scales that are much shorter than 100 ns. The experimental plasma has no time to interact with perturbations to the density of the background gas. The length of the plasma filament would thus be predicted to be longer in the propagating experiment than the stationary filament of the numerical simulation.

8.3 Conclusions

Spectroscopic measurements of electron density have been carried out on a microwave discharge plasma initiated by a focused Gaussian beam at 110 and 124.5 GHz. Stark broadening of the H_α line was used to obtain values of peak electron density at varying levels of microwave power at pressures from 25 to 700 Torr. The electron densities were found to closely follow the trend of the critical electron density for reflecting the incoming microwaves, given by Eq. 8.6. Electron density was found to vary only weakly with input power. Experimental values of electron density show agreement with several theoretical models, most notably the pressure dependent predictions of [17].

Two-dimensional interferometric measurements of gas density were carried out on a microwave discharge plasma at 124.5 GHz. Gas density was probed with visible lasers and a fast gating ICCD. Gas heating was found to decrease neutral gas density by more than 80% in very localized regions. Two-dimensional structure of the heated gas filaments was resolved. Making allowances for differences in geometry between experiment and simulation, recent numerical simulations by Kourtzanidis et. al. [18] were found to successfully predict many aspects of the heated gas filaments.

The publications [17] and [18] were extensions to the two-dimensional model of Boeuf et. al. [13–16], discussed in detail in section 7.3.2. This model has successfully reproduced the plasma propagation velocity of millimeter wave gas breakdowns (see Fig. 7-7b). Including the extensions of [17, 18], this model has successfully predicted the pressure dependent electron density and many aspects of the neutral gas heating in the system. The experimental measurements of this thesis, combined with those of earlier work, have enabled rigorous testing of the numerical model of Boeuf et. al., and it has been found to well describe many aspects of the complex plasma of a millimeter wave breakdown in air.

Chapter 9

Summary, Discussion, and Future Work

MIT's 1.5 MW, 110 - 124 GHz pulsed gyrotron is a unique resource, providing high power microwaves in a region of the electromagnetic spectrum that has historically not been available, for either research or application. In this thesis, this gyrotron has been exploited to study a variety of discharge phenomena, in vacuum and in gases, at frequencies an order of magnitude higher than previous experimental work.

9.1 Dielectric Multipactor

9.1.1 Experimental Results

A test stand was constructed to facilitate the study of dielectric multipactor discharges at 110 GHz. Two separate test structures were designed, to allow independent study of multipactor discharges with either tangential or normal surface RF electric fields. The experimentally measured multipactor discharge thresholds at 110 GHz have greatly expanded the set of published data available for understanding dielectric multipactor. The measurements of multipactor threshold fields were made at frequencies ten times higher than previously existing data. Compared with published data for fused quartz with tangential RF electric fields, and alumina with normal RF electric fields, it

can be concluded that multipactor onset thresholds scale linearly with frequency, as predicted in [6] and later theoretical papers.

Experimental data was collected to verify predicted values of power absorption by multipactor. With normal RF electric fields, the power absorption was found to scale roughly linearly with RF electric field, in agreement with the theory and experiment performed at 11.424 GHz in [76]. With tangential RF electric fields, power absorption was found to be largely independent of RF electric field strength. This was predicted in [22], but never experimentally tested. Finally, the theoretical values of power absorption, in either field orientation, were found to quantitatively agree with experimental data with realistic values of discharge area. Thus, these models can be useful for estimating heatloads in devices and experiments that cannot avoid operational regimes with dielectric multipactor.

Post-experiment examination of tested samples revealed that alumina and sapphire materials remained largely undamaged after 150 thousand high power pulses, with the exception of some discoloration. With normal electric fields, alumina was found to perform nearly as well as sapphire. Of the materials tested, these two materials are most suitable for use in high power microwave devices and accelerators in which multipactor may occur. Conversely, every sample of fused or crystal quartz suffered structural damage from multipactor. Multipactor on these materials should be minimized in high power microwave devices. High resistivity silicon was also tested with tangential RF electric fields. Samples were found to deteriorate at relatively low RF electric fields of 13 MV/m, though multipactor was not detected on the surfaces. High resistivity silicon is likely unsuitable for high power microwave applications with high surface electric fields.

9.1.2 Expansion of Existing Theory

Numerical theory of multipactor discharges on dielectric surfaces has existed since 1998 [6, 22], primarily in the form of Monte Carlo calculations. Existing theory predicted that the electric fields (RF and DC) necessary to initiate and sustain dielectric multipactor should scale linearly with frequency, though the majority of theory work

was constrained to the geometry of an RF beam passing through a window, with RF electric fields tangential to the dielectric surface. In this specific geometry, it was also predicted that the fraction of incoming RF power dissipated by dielectric multipactor is independent of the incident RF intensity.

The published Monte Carlo models used a simplified model of secondary electron yield, and neglected the RF magnetic field. Later publications explored the effect of the RF magnetic field [78–81], though these publications neglected the effects of focusing of electron impact times into a specific RF phase over the course of multiple electron impact, secondary electron launch, and subsequent secondary electron impact cycles. This led to significant disagreement in the predictions of electron impact energies and DC electric fields in a saturated, steady-state multipactor between [78–81] and the earlier publications, though the model did provide a good qualitative explanation of the effects of the RF magnetic field on electron dynamics.

The theory presented in this thesis builds on the Monte Carlo model of [6]. The theory presented in chapter 4 modified some of the underlying math of the calculation to allow for electrons to be lost (absorbed by the dielectric or escaped from the multipactor region), while still reproducing the predictions of [6] in conditions where electron loss is negligible. This allowed for the use of a realistic model of secondary electron yield (where low energy electrons are captured by the dielectric surface), as well as the extension of the model toward zero DC electric fields (where electrons may never return to the dielectric surface). All previously published numerical models of dielectric multipactor had used the same simplified model of secondary electron yield. It was found that the use of a realistic model of secondary electron yield, in a geometry with tangential RF electric fields, had a minimal impact on predicted DC electric fields, electron impact energies and electron transit times in a multipactor that had achieved stead-state. The realistic secondary electron yield model did, however, raise the upper threshold of RF electric field, above which multipactor will not occur, by a factor of more than 2.

The model was further extended by the inclusion of the RF magnetic field. This had been explored in [78–81], though neglecting the physics of RF phase focusing. In

the presented theory, the RF magnetic field was incorporated into the full Monte Carlo calculation, allowing direct comparison with the results of simpler calculations. The RF magnetic field effectively limits the maximum energy that electrons can gain from the RF electric field. This, combined with the effects of the realistic secondary electron yield model, completely eliminated the upper RF electric field threshold for materials of interest as RF windows. This has implications for experiment design, as quickly raising the RF intensity to "burn through" the region of multipactor susceptibility, successfully used in metallic particle accelerator structures, cannot be used to avoid multipactor on dielectric windows.

The model was additionally extended to a geometry with an RF electric field normal to a dielectric surface, similar to that encountered in a dielectric-lined waveguide that is designed as part of a particle accelerating structure. Models of similar geometry have been published [82], but, like previous models, a simplified model of secondary electron yield was used, and magnetic fields were neglected. Due to the lack of analytical solutions to electron motion with normal RF electric fields, the results of these published models were also less general, and it was necessary to directly calculate multipactor susceptibility regions for the materials tested in this thesis. The model presented in this thesis reproduced the prediction [76] that, to first order, the fraction of absorbed RF power is linearly proportional to the incident RF electric field. The model also provided insight into deviations from this first order behavior that arise from RF loading (absorption of a significant portion of the incident RF power) and changing electron impact energies of a steady-state multipactor with a realistic secondary electron yield model.

The inclusion of the RF magnetic field had negligible effects on the boundaries of the multipactor susceptibility regions with this geometry, because the magnetic field does not strongly affect electron impact times, as it does in the tangential field geometry. The use of a realistic model of secondary electron yield did extend multipactor susceptibility regions to higher values of RF electric field than previously published results, but not so much as to eliminate the possibility of quickly "burning through" this region, before charge can accumulate on the dielectric (see Fig. 4-10).

A fair amount of theoretical work has been done predicting the parameters of steady-state multipactor on a dielectric surface, but an accurate theory for predicting the threshold RF electric fields at which the dielectric multipactor is initiated remains elusive. The Monte Carlo model presented in this thesis predicts that, for an uncharged dielectric (zero DC electric field), multipactor should not spontaneously arise from a single electron impact. Secondary electrons tend to escape the region near the dielectric surface. Section 4.5 presents a simplistic model of the charging of a dielectric in a plane-wave RF field subject to impacts from stray electrons of unspecified source. This leads to a simple prediction of RF breakdown threshold, Eq. 4.16, reproduced below.

$$E_{RF} \approx \frac{\omega}{e}\sqrt{4mV_1} \tag{6.16}$$

Numerically accounting for the shape of Vaughan's model of secondary electron yield raises the predictions of RF thresholds above those given by Eq. 4.16 by about 20%. Predicted values accounting for the secondary electron yield model are collected in Table 4.2. The assumption of a plane-wave RF electric field, and the neglect of discharging of the dielectric material will lead this model to under predict the threshold RF electric field. However, this model was found to under predict multipactor thresholds measured in this thesis and those in previously published work by a factor of 2 or less, regardless of experiment geometry.

9.2 Millimeter Wave Discharges in Air

Prior studies performed at MIT discovered the complex nature of a mm-wave air discharge generated in free space by a focused, high power mm-wave beam. The plasma exhibits a two-dimensional structure of filaments, aligned with the RF electric field polarization, with approximately quarter-wavelength spacing. Since the publication of the initial observations of this spontaneously complex plasma, a number of theory groups outside of MIT have published numerical models to explain the plasma structure and predict additional properties. As part of this thesis work, spectroscopic measurements of Stark broadening of the H_α line were carried out to measure peak

electron density in the plasma as a function of background gas pressure and incident RF intensity. The optics of the existing experiment were then modified to create a plasma with highly reproducible initial filament placement and timing ($\sim$ 2 ns jitter). This allowed the development of time resolved diagnostics: visible light imaging and two dimensional laser interferometry. The visible light imaging and laser interferometry measurements were carried out simultaneously. A series of visible light images with 20 ns time resolution illuminated the dynamics of the plasma array, largely confirming previously reported details that showed the existence of only a few plasma filaments at any one time. Two-dimensional laser interferometry was used to measure changes in the background gas density as a function of time and space. This line integrated data was inverted to yield local values of gas density, allowing a thorough comparison with the predictions of published numerical theories. The measured values agreed quantitatively in magnitude and timing with the published model of [18], an extension to an earlier two-dimensional model [13–16] to include the effects of gas heating. The measurements of electron density, gas density perturbations due to heating, and previously made measurements of plasma propagation velocity have all been found to quantitatively agree with the predictions of this set of publications, well validating this particular numerical model of microwave-plasma interaction in a weakly ionized plasma.

9.3 Continuing Work on Millimeter Wave Breakdowns

9.3.1 A Laser-Driven Quasioptical Switch for Controlling and Shaping Megawatt Microwave Pulses

To enhance the versatility of MIT's 1.5 MW, 110 GHz gyrotron, a laser-driven semiconductor switch has been developed to shorten and shape the nominally 3 microsecond long microwave pulses. A schematic of this switch is shown in Fig. 9-1. A 532 nm laser, producing $\sim$ 6 ns pulses of up to 230 mJ is used to illuminate one or two semiconductor wafers. Gallium arsenide and silicon wafers have both been success-

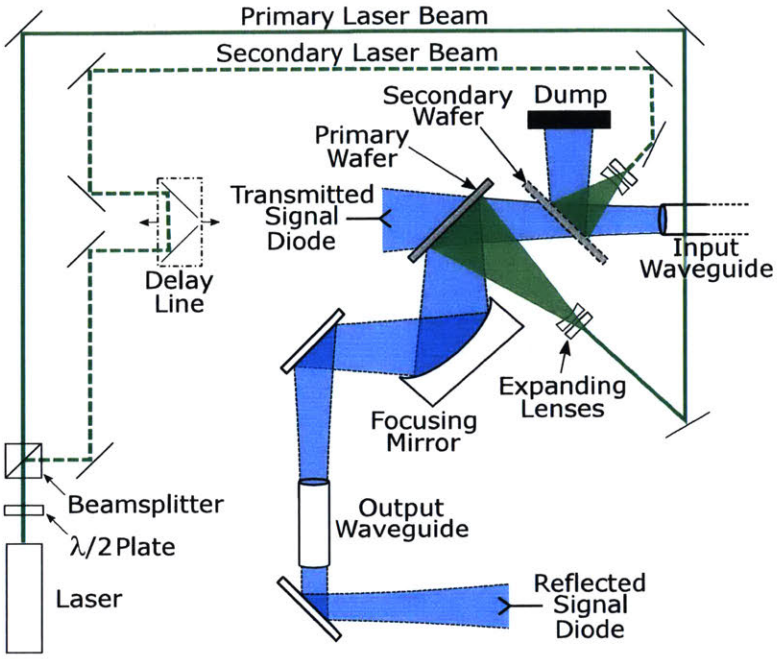

Figure 9-1: Experimental setup of the laser driven semiconductor switch. 110 GHz microwaves, seen in blue, are generated by the MIT 1.5 MW gyrotron (not shown) and enter the setup from the input waveguide. Beams from the high energy pulsed laser are shown in green. Reproduced from [19].

fully tested. In their normal state, the wafers are transparent to the microwave beam. Illumination by the high energy laser pulse induces photoconductivity, temporarily rendering the wafers mirror-like to the microwaves.

From the gyrotron, microwave pulses nominally have a 3 microsecond full-width at half-maximum (FWHM) with a ~500 ns rise and fall time. This laser driven switch allows the shortening of the rise and fall times to a few ns. Additionally, a pulse of a few ns to tens of ns can be picked out of the long pulse output from the gyrotron. Example output pulses from this switch can be seen in Fig. 9-2. This switch was developed to allow testing of 110 GHz discharges in metallic accelerating structures, where the full 3 microsecond microwave pulse would cause excessive surface heating in the structure. A publication is being prepared on the design and testing of this system [19]. The added experimental versatility provided by this switch can also be employed to further the study of multipactor discharges.

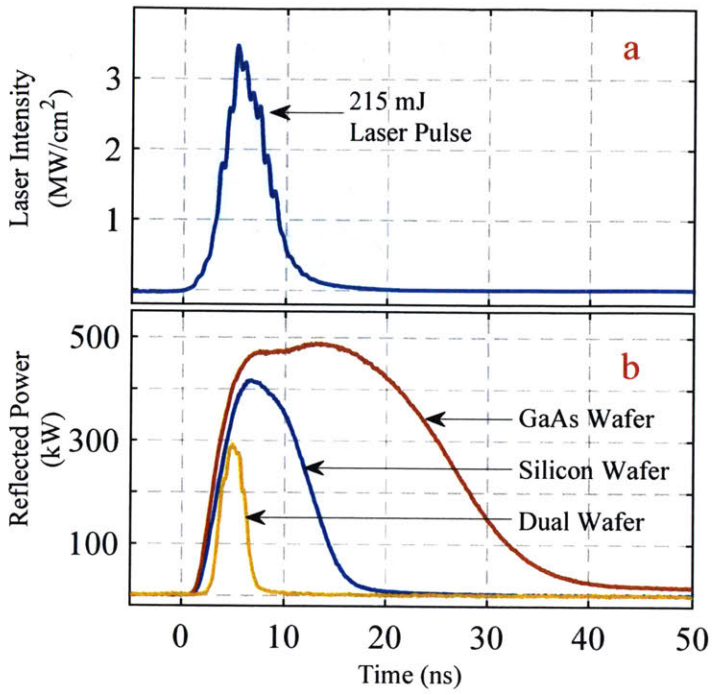

Figure 9-2: (a) Measured 532 nm laser pulse used to excite the Si and GaAs wafers, averaged over 100 pulses. The modal structure is inherent to the laser design. (b) Reflected pulses from a single GaAs wafer (red) and Si wafer (blue) with 525 kW incident 110 GHz RF power. An example pulse produced using two wafers is in yellow, with Si as the primary wafer (illuminated by 120 mJ of laser energy), and GaAs as the secondary wafer (illuminated by 100 mJ of laser energy). Adjusting an optical delay line (see Fig. 9-1) allows for continuous varying of the dual-wafer pulse width. Reproduced from [19].

9.3.2 Breakdowns in a Metallic Accelerating Structure at 110 GHz

RF discharges on metallic surfaces in vacuum are not well understood theoretically. It is hoped that, by raising the operating frequency of metallic, RF-driven electron accelerating structures by orders of magnitude, one can achieve extremely high accelerating gradients in a compact structure. Current state-of-the-art RF accelerating structures are limited to accelerating gradients of about 100 MV/m in copper structures at 11 GHz. In collaboration with SLAC, testing has begun on a copper cavity, designed to mimic an accelerating structure, using the MIT 110 GHz gyrotron and the microwave pulse shortening switch described in the previous section [20, 21, 136].

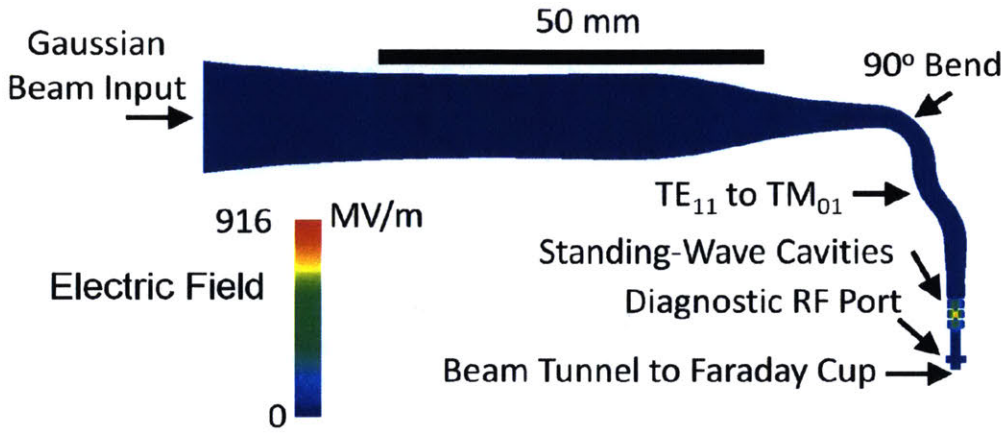

Figure 9-3: Electric RF fields in the mm-wave (specifically 110 GHz) accelerating structure that is being tested in collaboration with SLAC. The fields are calculated with 1 MW of power in the incident Gaussian Beam. Reproduced from [20, 21].

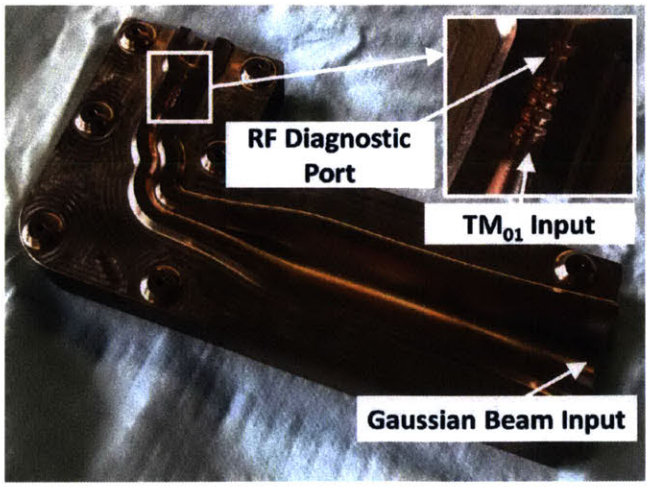

Figure 9-4: Photographs of the interior of the mm-wave accelerating structure, reproduced from [20].

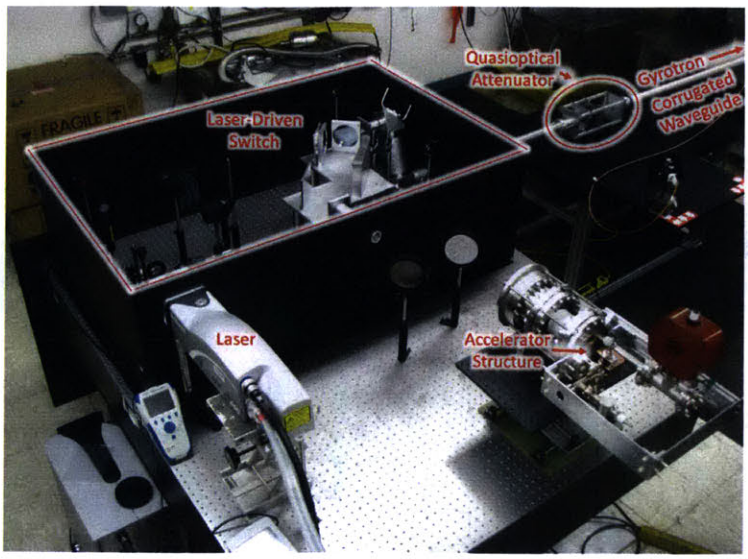

Figure 9-5: Photograph of the laboratory setup for testing of a 110 GHz metallic accelerating structure. The gyrotron microwave source is off the right side of the image. The photograph includes the laser-driven switch described in section 9.3.1.

The electromagnetic design of the experiment can be seen in Fig. 9-3. A horn accepts the Gaussian microwave beam output of the gyrotron. A long section of horn and bent waveguide converts the Gaussian beam to the TM_{01} mode of a circular waveguide, the standard operating mode of many metallic linear accelerators. This TM_{01} mode is coupled into a 3 cavity structure, though high fields are only excited in the central cavity. Fields in this figure are calculated assuming 1 MW of input power from the MIT gyrotron. The peak fields in the structure of 916 MV/m correspond to a time averaged accelerating gradient in the central cavity of about 400 MV/m.

The copper accelerating structure was fabricated in two pieces of copper and brazed together. The machined copper structure can be seen in Fig. 9-4. The structure has already been installed in the laboratory, and high power testing is currently underway. A photograph of the structure, mounted to a vacuum chamber, and aligned with the output of the laser-driven semiconductor switch is shown in Fig. 9-5. The structure has thus far survived testing at accelerating gradients in excess of 100 MV/m with 10 ns long pulses, and testing will continue to push to higher fields.

9.4 Opportunities for Future Work on Dielectric Multipactor

The newly constructed laser-driven semiconductor switch allows experiments with sharp rise time ($\lesssim 5$ ns) microwave pulses of variable length. This opens up the possibility to study and exploit the formation time of dielectric multipactor, something that has thus far been largely neglected, both experimentally and theoretically. One Monte Carlo calculation has been carried out to study the evolution of a dielectric multipactor discharge over time [22]. The key results of this calculation are reproduced in Fig. 9-6. The calculation was started with an areal electron density of 10 cm^{-2} with a 10 V/m DC electric field on a fused quartz window geometry (tangential RF electric fields), subject to an RF electric field of 3 MV/m at 2.45 GHz. After each impact of the simulated macroparticles, the total number of electrons, and the DC electric field were adjusted. The x-axis of each plot in Fig. 9-6 tracks the number of impacts and relaunches of each macroparticle as a proxy for time. This can be roughly converted to time by integrated the average transit time between impact for each bounce, shown in Fig. 9-6(e).

The total time elapsed between the start of this calculation and the formation of a multipactor discharge is greater than 10 microseconds, orders of magnitude greater than any experiment. This, however, is strongly a function of the arbitrarily chosen initial electron density and DC electric field. The suggestive part of this calculation is the prediction that the multipactor grows from about 1% to 100% of the saturated value of electron density, and dissipated power in about 4 ns, integrating the transit times for impacts 19-24. Though this is a rough estimate, it gives us a theoretical minimum build up time for a multipactor discharge. Provided the input RF electric field is scaled linearly with input RF frequency, this result is nearly independent of frequency. Average electron impact energies will remain the same. The macroparticle transit time, in this geometry, is independent of the RF field. Higher frequency discharges will take a little longer to grow to higher saturated DC electric fields, though this is an extension of the steepest part of the exponential rise in electron

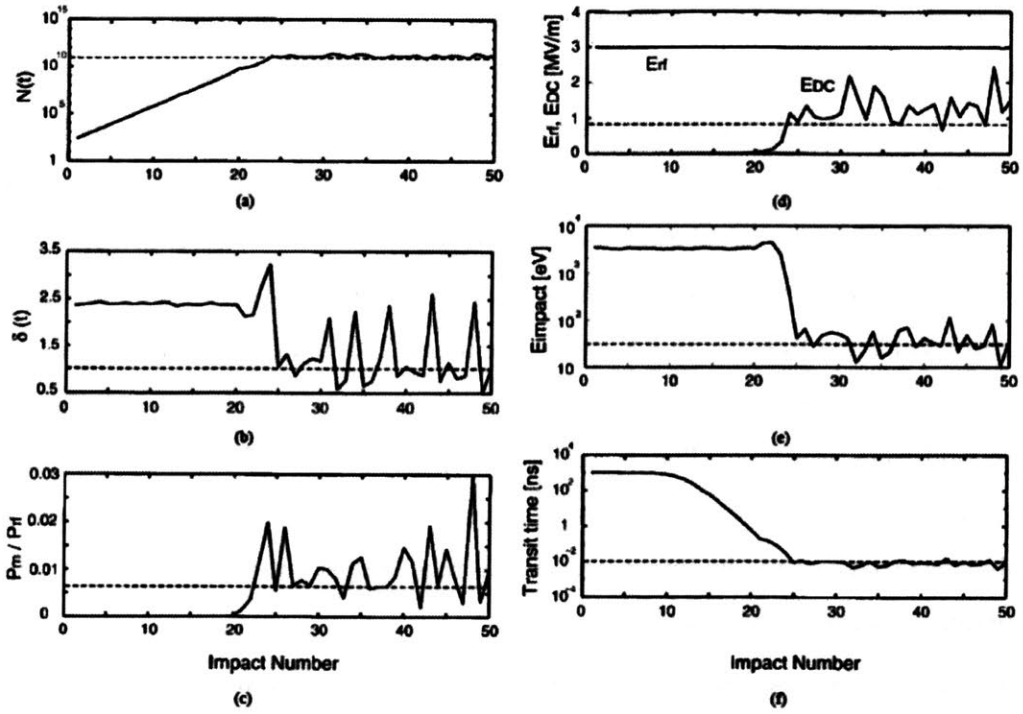

Figure 9-6: Theoretical evolution of a multipactor as a function of macroparticles impacts, reproduced from [22]. All subfigures share the same x-axis. The y-axis of each subfigure is averaged over all macroparticles in the Monte Carlo calculation. The total number of particles in the multipactor region is N, the average secondary electron yield is δ, and the fraction of incident RF power absorbed by the multipactor is P_m/P_{rf}. This calculation was performed for a 10 cm^2 area of a fused quartz window subject to a 2.45 GHz incident field of 3 MV/m (tangential RF electric field). The electron density of the multipactor grows from 1% to 100% of its saturated value between impacts 19-24, over about 4 ns.

density, and the additional necessary impact transit times will be negligibly short.

The switch presented in section 9.3.1 can provide triangular pulses with a FWHM of 3 ns. With the existing gallium arsenide wafers, these pulses can be extended to 20 ns. Undoped silicon wafers could be acquired to provide switch relaxation times of microseconds. This would allow probing of the formation time of a multipactor discharge, and an experimental verification of how short pulses need to be to avoid the phenomenon altogether.

Additionally, the theory of dielectric multipactor presented in chapter 4 suggests that the region of multipactor susceptibility exists in a relatively narrow band of RF electric field values with RF electric fields normal to the dielectric surface. If the high power microwave pulse can be swept to high enough RF electric field before a multipactor discharge can develop, this could provide an avenue for long-pulse operation of dielectric lined waveguide accelerating structures. The semiconductor switch could be configured to provide long RF pulses, but shorten the rise-time of the gyrotron pulses from ~500 ns to less than 5 ns. This may be sufficiently fast to sweep past the multipactor susceptibility region.

An accurate theory of the formative stages of dielectric multipactor discharge has remained elusive since study of the field began in earnest in 1998. We now have the proper tools to experimentally probe the phenomenon, possibly leading to a more complete understanding of multipactor discharge.

Bibliography

[1] Y. Hidaka, E. M. Choi, I. Mastovsky, M. A. Shapiro, J. R. Sirigiri, and R. J. Temkin. Observation of large arrays of plasma filaments in air breakdown by 1.5-MW 110-GHz gyrotron pulses. *Phys. Rev. Lett.*, 100:035003, 2008.

[2] D. S. Tax. *Experimental Study of a High Efficiency Step-Tunable MW Gyrotron Oscillator.* PhD thesis, Massachusetts Institute of Technology, Cambridge, MA, USA, 2013.

[3] R. G. Carter. *Microwave and RF Vacuum Electronic Power Sources.* Cambridge University Press, Cambridge, UK, 1965.

[4] E. M. Choi. *Experimental Study of a High Efficiency Gyrotron Oscillator.* PhD thesis, Massachusetts Institute of Technology, Cambridge, MA, USA, 2007.

[5] S. K. Jawla, J. P. Hogge, and S. Alberti. Theoretical investigation of iterative phase retrieval algorithm for quasi-optical millimeter-wave rf beams. *IEEE Trans. Plasma Sci.*, 37:403, 2009.

[6] R. A. Kishek and Y. Y. Lau. Multipactor discharge on a dielectric. *Phys. Rev. Lett.*, 80(1), 1998.

[7] J. R. M. Vaughan. Secondary emission formulas. *IEEE Trans. Electron Devices*, 40(4), 1993.

[8] Y. Hidaka, E. M. Choi, I. Mastovsky, M. A. Shapiro, J. R. Sirigiri, R. J. Temkin, G. F. Edmiston, A. A. Neuber, and Y. Oda. Plasma structures observed in gas breakdown using a 1.5 MW, 110 GHz pulsed gyrotron. *Phys. Plasmas.*

[9] A. Cook, M. Shapiro, and R. Temkin. Pressure dependence of plasma structure in microwave gas breakdown at 110 GHz. *Appl. Phys. Lett.*, 97:011504, 2010.

[10] R. B. Brode. The quantitative study of the collisions of electrons with atoms. *Rev. Mod. Phys.*, 5:257, 1933.

[11] A. M. Cook, J. S. Hummelt, M. A. Shapiro, and R. J. Temkin. Measurements of electron avalanche formation time in w-band microwave air breakdown. *Phys. Plasmas*, 18:100704, 2011.

[12] J. S. Hummelt, M. A. Shapiro, and R. J. Temkin. Spectroscopic temperature measurements of air breakdown plasma using a 110 GHz megawatt gyrotron beam. *Phys. Plasmas*, 19:123509, 2012.

[13] B. Chaudhury, J. P. Boeuf, and G. Q. Zhu. Pattern formation and propagation during microwave breakdown. *Phys. Plasmas*, 17:123505, 2010.

[14] J. P. Boeuf, B. Chaudhury, and G. Q. Zhu. Theory and modeling of self-organization and propagation of filamentary plasma arrays in microwave breakdown at atmospheric pressure. *Phys. Rev. Lett.*, 104:015002, 2010.

[15] G. Q. Zhu, J. P. Boeuf, and B. Chaudhury. Ionization-diffusion plasma front propagation in a microwave field. *Plasmas Sources Sci. Technol.*, 20(3):035007, 2011.

[16] B. Chaudhury and J. P. Boeuf. Computational studies of filamentary pattern formation in a high power microwave breakdown generated air plasma. *IEEE Trans. Plasma Sci.*, 38(9):2281, 2010.

[17] Q. Zhou and Z. Dong. Modeling study on pressure dependence of plasma structure and formation in 110 GHz microwave air breakdown. *Appl. Phys. Lett.*, 98:161504, 2011.

[18] K. Kourtzanidis, F. Rogier, and J. P. Boeuf. Gas heating effects on the formation and propagation of a microwave streamer in air. *J. Appl. Phys.*, 118:103301, 2015.

[19] J. F. Picard, S. C. Schaub, G. Rosenzweig, J. C. Stephens, M. A. Shapiro, and R. J. Temkin. Laser-driven semiconductor switch for generating nanosecond pulses from a megawatt gyrotron. *Will Be Submitted to Appl. Phys. Lett. in 2019*, 2019.

[20] E. A. Nanni, V. A. Dolgashev, A. Haase, J. Neilson, S. Tantawi, S. C. Schaub, R. J. Temkin, and B. Spataro. Prototyping high-gradient mm-wave accelerating structures. *J. Phys.: Conf. Ser.*, 874, 2017.

[21] E. A. Nanni, V. A. Dolgashev, S. Jawla, J. Neilson, M. Othman, J. Picard, S. Schaub, B. Spataro, S. Tantawi, and R. J. Temkin. Results from mm-wave accelerating structure high-gradient tests. In *Proc. 43rd Int. Conf. on Infrared, Millimeter, Terahertz Waves*, 2018.

[22] L. K. Ang, Y. Y. Lau, R. A. Kishek, and R. M. Gilgenbach. Power deposited on a dielectric by multipactor. *IEEE Trans. Plasma Sci.*, 26(3), 1998.

[23] P. F. Goldsmith. *Quasioptical Systems.* IEEE Press.

[24] J. Lesurf. *Millimetre-wave Optics, Devices & Systems.* Adam Hilger.

[25] K. J. Sleger, R. H. Abrams, and R. K. Parker. Trends in solid-state microwave and millimeter-wave technology. *Applied Microwave*, 12:24, 1990.

[26] J. P. Anderson. *Experimental Study of a 1.5-MW, 110-GHz Gyrotron Oscillator.* PhD thesis, Massachusetts Institute of Technology, Cambridge, MA, USA, 2005.

[27] C. R. Crowell. The richardson constant for thermionic emission in schottky barrier diodes. *Solid-State Electron.*, 8:395, 1965.

[28] A. S. Gilmore. *Principles of Traveling Wave Tubes.* Artech House.

[29] J. P. Anderson, S. E. Korbly, R. J. Temkin, M. A. Shapiro, K. L. Felch, and S. Cauffman. Design and emission uniformity studies of a 1.5-MW gyrotron electron gun. *IEEE Trans. Plasma Sci.*, 30:2117, 2002.

[30] S. N. Vlasov, L. I. Zagryadskaya, and M. I. Petelin. Transformation of a whispering gallery mode, propagating in a circular waveguide, into a beam of waves. *Radio Eng. Electron. Phys.*, 12:14, 1975.

[31] G. G. Denisov, A. N. Kuftin, V. I. Malygin, N. P. Venediktov, D. V. Vinogradov, and V. E. Zapevalov. 110 GHz gyrotron with built-in high-efficiency converter. *Int. J. Electron.*, 72:1079, 1992.

[32] J. P. Anderson, M. A. Shapiro, R. J. Temkin, I. Mastovsky, and S. R. Cauffman. Studies of the 1.5-MW 110-GHz gyrotron experiment. *IEEE Trans. Plasma Sci.*, 32(3), 2004.

[33] E. M. Choi, C. D. Marchewka, I. Mastovsky, J. R. Sirigiri, M. A. Shapiro, and R. J. Temkin. Experimental results for a 1.5 MW, 110 GHz gyrotron oscillator with reduced mode competition. *Phys. Plasmas*, 13, 2006.

[34] D. S. Tax, B. Y. Rock, B. J. Fox, S. K. Jawla, S. C. Schaub, M. A. Shapiro, R. J. Temkin, and R. J. Vernon. Experimental results for a pulsed 110/124.5-GHz megawatt gyrotron. *IEEE Trans. Plasma Sci.*, 42(5):1128, 2014.

[35] E. J. Kowalski, D. S. Tax, M. A. Shapiro, J. R. Sirigiri, R. J. Temkin, T. S. Bigelow, and D. A. Rasmussen. Linearly polarized modes of a corrugated metallic waveguide. *IEEE Trans. Microw. Theory Tech*, 58(11), 2010.

[36] M. A. Shapiro and R. J. Temkin. Calculation of a hyperbolic corrugated horn converting the tem_{00} mode to the he_{11} mode. *J. Infrared Millim. Terahertz Waves*, 32, 2011.

[37] S. K. Jawla, E. A. Nanni, M. A. Shapiro, P. P. Woskov, and R. J. Temkin. Mode content determination of terahertz corrugated waveguides using experimentally measured radiated field patterns. *IEEE Trans. Plasma Sci.*, 40(6), 2012.

[38] A. H. W. Beck and H. Ahmed. *An Introduction to Physical Electronics*, page 196. Elsevier, New York, 1968.

[39] V. H. Ritz, R. E. Thomas, J. W. Gibson, and J. Klebanoff. Secondary electron emission characteristics of oxidized beryllium cathodes. *Surface Interface Anal.*, 11, 1988.

[40] A. Shih and C. Hor. Secondary emission properties as a function of the electron incidence angle. *IEEE Trans. Electron Devices*, 40(4), 1993.

[41] J. R. M. Vaughan. Multipactor. *IEEE Trans. Electron Devices*, 35(7), 1988.

[42] J. R. M. Vaughan. A new formula for secondary emission yield. *IEEE Trans. Electron Devices*, 36(9), 1989.

[43] R. G. Lye and A. J. Dekker. Theory of secondary emission. *Phys. Rev.*, 107, 1957.

[44] O. Hachenberg and W. Brauer. *Secondary Electron Emission from Solids*, pages 413–499. Academic Press, New York, 1959.

[45] P. H. Dawson. Secondary electron emission yields of some ceramics. *Journal of Applied Physics*, 37(9), 1966.

[46] R. A. Kishek, Y. Y Lau, L. K. Ang, A. Valfells, and R. M. Gilgenbach. Multipactor discharge on metals and dielectrics: Historical review and recent theories. *Phys. Plasmas*, 5(5), 1998.

[47] C. Gutton. Sur la décharge électrique à fréquence très élevée. *Comptes-Rendus Hebdomadaires des Séances de l'Académie des Sciences*, 178.

[48] P. T. Farnsworth. Television by electron image scanning. *J. Franklin Inst.*, 218, 1934.

[49] Institute news and radio notes. *Proc. IRE*, 24(2):149, 1936.

[50] W. G. Abraham. *Interactions of Electrons and Fields in Cavity Resonators.* PhD thesis, Stanford University, 1950.

[51] W J. Gallagher. The multipactor effect. *IEEE Trans. Nucl. Sci*, 26(3), 1979.

[52] C. Bates, G. deLhery, P. Fischer, and J. Hartley. Multipactor electron gun for millimeter wave tubes. In *1981 International Electron Devices Meeting*, pages 339–343, 1981.

[53] P. E. Ferguson and R. D. Dokken. A high power x-band receiver protector. In *1974 International Electron Devices Meeting (IEDM)*, pages 591–591, 1974.

[54] T. P. Carlisle. X-band high-power multipactor receiver protector. *IEEE Transactions on Microwave Theory and Techniques*, 26(5), 1978.

[55] R. F. Bilotta. Receiver protectors: A technology update. *Microw. J.*, 40(8), 1997.

[56] D. H. Preist and R. C. Talcott. On the heating of output windows of microwave tubes by electron bombardment. *IEEE Trans. Electron Devices*, 8, 1961.

[57] J. R. M. Vaughan. Observations of multipactor in magnetrons. *IEEE Trans. Electron Devices*, 15(11), 1968.

[58] A. S. Gilmore. *Microwave Circuits*, page 206. D. Van Nostrand Company, INC., Princeton, NJ, 1964.

[59] Y. Saito ; S. Michizono ; S. Anami ; S. Kobayashi. Surface flashover on alumina rf windows for high-power use. *IEEE Trans. Electron Devices*, 28(4), 1993.

[60] A. J. Hatch. Suppression of multipacting in particle accelerators. *Nucl. Instr. Methods*, 41(2), 1966.

[61] P. M. Lapostolle and A. L. Septier. *Linear Accelerators*, page 917. North Holland, Amsterdam, 1970.

[62] C. M. Lyneis, H. A. Schwettman, and J. P. Turneaure. Elimination on electron multipacting in superconducting structures for electron accelerators. *Appl. Phys. Lett.*, 31, 1977.

[63] R. Boni, V. Chimenti, P. Fernandes, R. Parodi, B. Spataro, and F. Tazzioli. Reduction of multipacting in an accelerator cavity. *IEEE Trans. Nucl. Sci.*, 32(5), 1985.

[64] V. Shemelin. Multipactor in crossed rf fields on the cavity equator. *Phys. Rev. St. Accel. Beams*, 16, 2013.

[65] N. Rozario, H.F. Lenzing, K.F. Reardon, M.S. Zarro, and C.G. Baran. Investigation of telstar 4 spacecraft ku-band and c-band antenna components for multipactor breakdown. *IEEE Trans. Microwave Theory Tech.*, 42, 1994.

[66] A. D. Woode and J. Petit. Investigations into multipactor breakdown in satellite microwave payloads. *Microw. J.*, 14(4), 1990.

[67] A. D. Woode and J. Petit. Design data for the control of multipactor discharge in spacecraft microwave and rf systems. *Microw. J.*, 35(1), 1992.

[68] Juan de Lara, Francisco Pérez, Manuel Alfonseca andLuis Galán amd Isabel Montero, Elisa Román, and David Raboso Garcia-Baquero. Multipactor prediction for on-board spacecraft rf equipment with the mest software tool. *IEEE Trans. Plasma Sci.*, 34(2), 2006.

[69] F. Hähn, W. Jacob, R. Beckmann, and R. Wilhelm. The transition of a multipactor to a low-pressure gas discharge. *Phys. Plasma*, 4, 1998.

[70] J. R. M. Vaughan. Some high power window failures. *IEEE Trans. Electron Devices*, 8, 1961.

[71] F. Krienen. Electron wind in strong wave guide fields. *IEEE Trans. Nucl. Sci.*, 32(5), 1985.

[72] S. Yamaguchi, Y. Saito, S. Anami, and S. Michizono. Trajectory simulation of multipactoring electrons in an s-band pillbox rf window. *IEEE Trans. Nucl. Sci.*, 39, 1992.

[73] A. Neuber, J. Dickens, D. Hemmert, H. Krompholz, L. L. Hatfield, and M. Kristiansen. On the heating of output windows of microwave tubes by electron bombardment. *IEEE Trans. Plasma Sci.*, 26(3), 1998.

[74] O. A. Ivanov, M. A. Lobaev, V. A. Isaev, and A. L. Vikharev. Suppressing and initiation of multipactor discharge on a dielectric by an external dc bias. *Phys. Rev. ST Accel. Beams*, 13, 2010.

[75] A. S. Sakharov, V. A. Ivanov, Yu. A. Tarbeeva, and M. E. Konyzhev. Theoretical and experimental study of microwave power absorption by a singlesided multipactor discharge on a dielectric. *Plasma Phys. Reports*, 38(13), 2012.

[76] J. G. Power, W. Gai, S. H. Gold, A. K. Kinkead, R. Konecny, and C. Jing. Observation of multipactor in an alumina-based dielectric-loaded accelerating structure. *Phys. Rev. Lett.*, 92, 2004.

[77] C. Jing, W. Gai, J. G. Power, R. Konecny, S. H. Gold, W. Liu, and A. K. Kinkead. High-power rf tests on x-band dielectric-loaded accelerating structures. *IEEE Trans. Plasma Sci.*, 33(4), 2004.

[78] A. Sazontov, V. Semenov, M. Buyanova, N. Vdovicheva, D. Anderson, M. Lisak, J. Puech, and L. Lapierre. Multipactor discharge on a dielectric surface: Statistical theory and simulation results. *Phys. Plasmas*, 12, 2005.

[79] A. G. Sazontov and V. E. Nechaev. Effects of rf magnetic field and wave reflection on multipactor discharge on a dielectric. *Phys. Plasmas*, 17, 2010.

[80] A. G. Sazontov, V. E. Nechaev, and N. K. Vdovicheva. The susceptibility diagrams of a multipactor discharge on a dielectric: Effects of rf magnetic field. *Appl. Phys. Lett.*, 98, 2011.

[81] A. G. Sazontov, V. E. Nechaev, and N. K. Vdovicheva. Statistical prediction of microwave window breakdown: Effects of rf magnetic field. *IEEE Trans. Plasma Sci.*, 40(2), 2012.

[82] L. Wu and L. K. Ang. Multipactor discharge in a dielectric-loaded accelerating structure. *Phys. Plasmas*, 14, 2007.

[83] O. V. Sinitsyn, G. S. Nusinovich, and T. M. Antonsen. Self-consistent nonstationary two-dimensional model of multipactor in dielectric-loaded accelerator structures. *Phys. Plasmas*, 16, 2009.

[84] A. S. Sakharov, V. A. Ivanov, and M. E. Konyzhev. Multipactor discharge on a dielectric at different inclination angles of the microwave electric field relative to the dielectric surface. *Plasma Phys. Reports*, 39(13), 2013.

[85] A family of embedded runge-kutta formulae. *Journal of Computational and Applied Mathematics*, 6(1):19 – 26, 1980.

[86] Ansys, Inc. Ansys electronics desktop [online]. available: www.ansys.com 2015.

[87] V. V. Parshin. Dielectric materials for gyrotron output windows. *Int J Infrared Milli Waves*, 15(2), 1994.

[88] J. W. Lamb. Miscellaneous data on materials for millimetre and submillimetre optics. *Int J Infrared Milli Waves*, 17(12), 1996.

[89] V. V. Parshin, M. Y. Tretyakov, and M. A. Koshelev. Instrumental complex and the results of precise measurements of millimeter- and submillimeter-wave propagation in condensed media and the atmosphere. *Radiophys. Quantum El.*, 52(8), 2009.

[90] C. R. Jones, J. Dutta, G. Yu, and Y. Gao. Measurement of dielectric properties for low-loss materials at millimeter wavelengths. *Int J Infrared Milli Waves*, 32(6), 2011.

[91] C. Yeh and F. I. Shimabukuro. *The Essence of Dielectric Waveguides*, pages 137–150. Springer, New York, 2008.

[92] J. R. Carson, S. P. Mead, and S. A. Schelkunoff. Hyper-frequency wave guides: Mathematical theory. *Bell Syst. Tech. J*, 15(2), 1936.

[93] E. Snitzer. Cylindrical dielectric waveguide modes. *J. Opt. Soc. Am*, 51(5), 1961.

[94] P. J. B. Clarricoats. Propagation along unbounded and bounded dielectric rods. part 1: Propagation along an unbounded dielectric rod. *Proc. IEEE Part C: Monographs*, 108(13), 1961.

[95] D. Marcuse. Excitation of the dominant mode of a round fiber by a gaussian beam. *Bell Syst. Tech. J*, 49(8), 1970.

[96] A. W. Snyder. Excitation and scattering of modes on a dielectric or optical fiber. *IEEE Trans. Microw. Theory Tech*, 17(12), 1969.

[97] C. R. Li and T. S. Sudarshan. Characteristics of preflashover light emission from dielectric surfaces in vacuum. *IEEE Trans. Dielectr. Electr. Insul.*, 2(3), 1995.

[98] A. S. Gilmore. *Microwave Tubes*, page 474. Artech House, Norwood, MA, 1986.

[99] Y. P. Raizer. *Gas Discharge Physics*. Springer, Berlin, 1991.

[100] A. V. Gurevich, N. D. Borisov, and G. M. Milikh. *Physics of Microwave Discharges.* Gordon and Breach, Amsterdam, 1997.

[101] A. D. MacDonald. *Microwave Breakdown in Gases.* John Wiley and Sons, Inc., New York, 1966.

[102] N. A. Bogatov, Y. V. Bykov, N. P. Venediktov, S. V. Golubev, V. G. Zorin, A. G. Eremeev, and V. E. Semenov. Light-distribution of the bichromic gelatin layer during hologram registration on the contradirected circuit. *Sov. J. Plasma Phys.*, 12(6):725, 1986.

[103] T. V. Borodacheva, S. V. Golubev, V. G. Zorin, A. G. Eremeev, and V. E. Semenov. *Sov. J. Plasma Phys.*, 15(1):62, 1989.

[104] A. L. Vikharev, A. M. Gorbachev, A. V. Kim, and A. L. Kolysko. Formation of small-scale structure of microwave discharge in high-pressure gas. *Sov. J. Plasma Phys.*, 18(8):554, 1992.

[105] Y. Oda, K. Komurasaki, K. Takahashi, A. Kasugai, and K. Sakamoto. Plasma generation using high-power millimeter-wave beam and its application for thrust generation. *J. Appl. Phys.*, 100:113307, 2006.

[106] V. L. Bratman, S. V. Golubev, I. V. Izotov, Y. K. Kalynov, V. A. Koldanov, A. G. Litvak, S. V. Razin, A. V. Sidorov, V. A. Skalyga, and V. G. Zorin. Features of plasma glow in low pressure terahertz gas discharge. *Phys. Plasmas*, 20:123512, 2013.

[107] D. Kim, D. Yu, A. Sawant, M. S. Choe, I. Lee, S. G. Kim, and E. M. Choi. Remote detection of radioactive material using high-power pulsed electromagnetic radiation. *Nature Comm.*, 8:15394, 2017.

[108] G. S. Nusinovich, R. Pu, T. M. Antonsen Jr., O. V. Sinitsyn, J. Rodgers, A. Mohamed, J. Silverman, M. Al-Sheikhly, Y. S. Dimant, G. M. Milikh, M. Y. Glyavin, A. G. Luchinin, E. A. Kopelovich, and V. L. Granatstein. Development of THz-range gyrotrons for detection of concealed radioactive materials. *J. Infrared Millim. Terahertz Waves*, 32(3), 2011.

[109] V. L. Granatstein and G. S. Nusinovich. Detecting excess ionizing radiation by electromagnetic breakdown of air. *J. Appl. Phys.*, 108:063304, 2010.

[110] Y. Oda, Teppei Shibata, K. Komurasaki, K. Takahashi, A. Kasugai, and K. Sakamoto. Thrust performance of microwave rocket under repetitive-pulse operation. *J. Propul. Power*, 25:118, 2009.

[111] W. C. Taylor, W. E. Scharfman, and T. Morita. Voltage breakdown of microwave antennas. In L. Young, editor, *Advances in Microwaves, Vol. 7*, pages 59–130. Academic Press, New York, 1971.

[112] A. M. Cook, J. S. Hummelt, M. A. Shapiro, and R. J. Temkin. Millimeter wave scattering and diffraction in 110 GHz air breakdown plasma. *Phys. Plasmas*, 20:043507, 2013.

[113] D. R. Miller and R. P Andres. Rotational relaxation of molecular nitrogen. *J. Chem. Phys.*, 46(9), 1967.

[114] S. K. Nam and J. P. Verboncoeur. Theory of filamentary plasma array formation in microwave breakdown at near-atmospheric pressure. *Phys. Rev. Lett.*, 103:055004, 2009.

[115] H. C. Kim and J. P. Verboncoeur. Reflection, absorption and transmission of te electromagnetic waves propagation in a nonuniform plasma slab. *Comput. Phys. Commun.*, 117:118, 2007.

[116] G. J. M. Hagelaar and L. C. Pitchford. Solving the boltzmann equation to obtain electron transport coefficients and rate coefficients for fluid models. *Plasma Sources Sci. Technol.*, 14, 2005.

[117] V. E. Semenov, E. I. Rakova, V. P. Tarakanov, M. Yu. Glyavin, and G. S. Nusinovich. *Phys. Plasmas*, 22:092308, 2015.

[118] V. E. Semenov, E. I. Rakova, M. Yu. Glyavin, and G. S. Nusinovich. Study of a stationary breakdown wave under the conditions of noticeable reflection of the incident electromagnetic wave from a gas-discharge plasma. *Radiophys. Quantum Electr.*, 58(5):327, 2015.

[119] C. O. Laux, T. G. Spence, C. H. Kruger, and R. N. Zare. Optical diagnostics of atmospheric pressure air plasmas. *Plasma Sources Sci. Technol.*, 12(2):125, 2003.

[120] H. R. Griem. *Plasma Spectroscopy.* McGraw-Hill, New York, 1964.

[121] N. Konjevic, M. Ivkovic, and N. Sakan. Hydrogen balmer lines for low electron number density plasma diagnostics. *Spectrochimica Acta B*, 76(16), 2012.

[122] M. A. Gigosos and V. Cardeñoso. New plasma diagnosis tables of hydrogen stark broadening including ion dynamics. *J. Phys B*, 29.

[123] W. L. Wiese and J. R. Fuhr. Accurate atomic transition probabilities for hydrogen, helium, and lithium. *J. Phys. Chem. Ref. Data*, 38(565), 2009.

[124] A. E. Kramida. A critical compilation of experimental data on spectral lines and energy levels of hydrogen, deuterium, and tritium. *At. Data Nucl. Data Tables*, 96(586), 2010.

[125] Y. V. Bykov, M. S. Gitlin, M. A. Novikov, I. N. Polushkin, Y. I. Khanin, and A. I. Shcherbakov. Measurement of gas temperature by intracavity laser spectroscopy. *Sov. Phys. Tech. Phys.*, 29(7):755, 1984.

[126] N. A. Bogatov, M. S. Gitlin, S. N. Golubev, I. N. Polushkin, and S. V. Razin. Experimental study of the instability of an externally maintained microwave discharge. *Sov. J. Plasma Phys.*, 13(5):364, 1987.

[127] A. L. Vikharev, M. S. Gitlin, O. A. Ivanov, I. N. Polushkin, A. N. Stepanov, and A. I. Shcherbakov. Heating of nitrogen in a pulsed microwave discharge under strong excitation of electron levels. *Sov. Tech. Phys. Lett.*, 13(2):91, 1987.

[128] R. H. Huddlestone and S. L. Leonard. *Plasma Diagnostic Techniques.* Academic, New York, 1965.

[129] B. V. Weber and S. F. Fulghum. *Laser-Aided Diagnostics of Plasmas and Gases.* IOP Publishing, Philadelphia, 2001.

[130] M. A. Gdeisat, D. R. Burton, and M. J. Lalor. Spatial carrier fringe pattern demodulation by use of a two-dimensional continuous wavelet transform. *Appl. Opt.*, 45(34):8722, 2006.

[131] J. Ma, Z. Wang, B. Pan, T. Hoang, M. Vo, and L. Luu. Two-dimensional continuous wavelet transform for phase determination of complex interferograms. *Appl. Opt.*, 50(16):2425, 2011.

[132] M. Hipp, J. Woisetschläger, P. Reiterer, and T. Neger. Digital evaluation of interferograms. *Measurement*, 36(1), 2004.

[133] R. M. Goldstein, H. A. Zebker, and C. L. Werner. Satellite radar interferometry: Two-dimensional phase unwrapping. *Radio Sci.*, 23(4):713, 1987.

[134] W. C. Gardiner Jr., Y. Hidaka, and T. Tanzawa. Refractivity of combustion gases. *Combust. Flame*, 40:213, 1981.

[135] P. A. Vicharelli and W. P. Lapatovich. Iterative method for computing the inverse abel transform. *Appl. Phys. Lett.*, 50:557, 1987.

[136] E. A. Nanni, V. A. Dolgashev, J. Neilson, S. G. Tantawi, S. Jawla, R. J. Temkin, S. C. Schaub, and B. Spataro. Toward high-power high-gradient testing of mm-wave standing-wave accelerating structures. In *Proc. 9th Int. Particle Accelerator Conf.*, 2018.